University of Massachusetts Amherst
ScholarWorks@UMass Amherst

Doctoral Dissertations | Dissertations and Theses

June 2021

ELECTRO-THERMAL TRANSPORT IN TWO-DIMENSIONAL MATERIALS AND THEIR HETEROSTRUCTURES

Arnab K. Majee
University of Massachusetts Amherst

Follow this and additional works at: https://scholarworks.umass.edu/dissertations_2

 Part of the Electrical and Electronics Commons, Electronic Devices and Semiconductor Manufacturing Commons, Heat Transfer, Combustion Commons, and the Semiconductor and Optical Materials Commons

Recommended Citation

Majee, Arnab K., "ELECTRO-THERMAL TRANSPORT IN TWO-DIMENSIONAL MATERIALS AND THEIR HETEROSTRUCTURES" (2021). *Doctoral Dissertations*. 2198.
https://doi.org/10.7275/22139731.0 https://scholarworks.umass.edu/dissertations_2/2198

This Open Access Dissertation is brought to you for free and open access by the Dissertations and Theses at ScholarWorks@UMass Amherst. It has been accepted for inclusion in Doctoral Dissertations by an authorized administrator of ScholarWorks@UMass Amherst. For more information, please contact scholarworks@library.umass.edu.

University of Massachusetts Amherst
ScholarWorks@UMass Amherst

Doctoral Dissertations | Dissertations and Theses

ELECTRO-THERMAL TRANSPORT IN TWO-DIMENSIONAL MATERIALS AND THEIR HETEROSTRUCTURES

Arnab K. Majee

Follow this and additional works at: https://scholarworks.umass.edu/dissertations_2

 Part of the Electrical and Electronics Commons, Electronic Devices and Semiconductor Manufacturing Commons, Heat Transfer, Combustion Commons, and the Semiconductor and Optical Materials Commons

ELECTRO-THERMAL TRANSPORT IN TWO-DIMENSIONAL MATERIALS AND THEIR HETEROSTRUCTURES

A Dissertation Presented

by

ARNAB K. MAJEE

Submitted to the Graduate School of the
University of Massachusetts Amherst in partial fulfillment
of the requirements for the degree of

DOCTOR OF PHILOSOPHY

May 2021

Electrical and Computer Engineering

© Copyright by Arnab K. Majee 2021

All Rights Reserved

ELECTRO-THERMAL TRANSPORT IN TWO-DIMENSIONAL MATERIALS AND THEIR HETEROSTRUCTURES

A Dissertation Presented

by

ARNAB K. MAJEE

Approved as to style and content by:

Prof. Zlatan Aksamija, Chair

Prof. Neal Anderson, Member

Prof. Eric Polizzi, Member

Prof. Ashwin Ramasubramaniam, Member

Prof. Christopher V. Hollot, Department Head
Electrical and Computer Engineering

DEDICATION

To my lovely mother.

ACKNOWLEDGMENTS

To quote William Arthur Ward, *The good teacher explains. The superior teacher demonstrates. The great teacher inspires.*

I express my deepest gratitude and profound respect to my Ph.D. advisor Dr. Zlatan Aksamija who has guided and encouraged me at all the stages of my Ph.D.. Professor Aksamija has served as a role model; his unique style of thinking, interesting ways to approach new problems and incessant enthusiasm to solve them have always motivated me to grow into a better researcher. His timely suggestions, scholarly advice and critical review of my work have helped me to accomplish my research goals smoothly. I would like to also thank him for always believing in me and supporting me, especially when I, myself, would be questioning my abilities to be a successful researcher. I would like to acknowledge and be grateful to him for providing all the necessary training to succeed in my future research endeavors.

I owe a deep sense of gratitude to Prof. Neal Anderson and Prof. Eric Polizzi, who introduced me to solid state electronics in my first semester at UMass Amherst and for also serving in my master's thesis and Ph.D. committees. I would like to also thank Prof. Ashwin Ramasubramaniam for being supportive and for serving as an external committee member for my Ph.D. dissertation.

I want to thank my family—my mother, father and brother, without whom none of this would ever have been possible. I have had their love and support in everything I have done. A special thanks to Pooja Saha for always being there for me, and for cheering me up when I was feeling down; without her support, this would have been impossible.

I am also grateful to my labmates for always providing useful suggestions related to my research. I cannot thank enough Cameron J. Foss and Adithya Kommini for all the

late-night zoom calls whenever I had questions related to Density Functional Theory calculations. A special thank you to all those whose support and friendship helped me to stay focused, especially, during festive seasons when I would be missing home. I will also like to extend my heartiest graditude to Rajarshi Roychowdhury, Samrat Sur, Moumita Dasgupta, Aruni Roy Chowdhury, Moumita Ray, Adithya Kommini, Pritha Dutta, Ishita Dasgupta, Kaushal Sumaria, Rishabh Chaudhary, Chirantan Kanani, Priyanka Chowdhury and Anamika Sen for being my family at Amherst.

ABSTRACT

ELECTRO-THERMAL TRANSPORT IN TWO-DIMENSIONAL MATERIALS AND THEIR HETEROSTRUCTURES

MAY 2021

ARNAB K. MAJEE

B.Tech., W.B.U.T. INDIA

M.S.E.C.E., UNIVERSITY OF MASSACHUSETTS AMHERST

Ph.D., UNIVERSITY OF MASSACHUSETTS AMHERST

Directed by: Professor Prof. Zlatan Aksamija

"Smaller is better" is the mantra that has driven semiconductor industry for the past 50 years. The on-going quest for faster electronic switching, higher transistor density, and better device performance, has been driven by a self-fulfilling prophecy popularly known as *Moore's law*, according to which the number of transistors per unit area of a chip doubles itself approximately every two years. A modern smartphone has about 8 billion transistors, which is as large as current earth's population. Although each transistor dissipates negligible power, but the collective power dissipation from all the transistors in an electronic gadget and inefficient heat removing capability of ultrathin silicon have led to the formation of *hotspots*—which degrade device performance and, ultimately, lead to their failure. Since the breakthrough of graphene, two-dimensional (2D) materials have drawn tremendous research attention due to their ultra-thin nature and yet high carrier mobility and are, thus, envisioned as potential materials to replace silicon in future electronic devices.

Among 2D materials, transition metal dichalcogenides (TMDs) and black phosphorene (a 2D analogue of black phosphorus) exhibit high carrier mobility and on-off ratio—necessary requirements for high-speed switching applications. 2D materials, in suspended form, exhibit extremely high carrier mobility, but when they are placed on a substrate, as would be the case in a transistor, their mobility drops by one to two orders of magnitude due to strong Coulomb scattering from the charged impurities in the substrate. In few-layered (FL) devices, where the top layers are shielded from the charged impurities by bottom layers, the mobility has been found to improve significantly. Due to high surface-to-volume ratio, heat removal in FL devices occurs mainly in the cross-plane direction. Weak vdW forces cause weak thermal coupling between layers, and therefore limits the heat-removing capability—characterized by thermal boundary conductance (TBC)—of these materials in the cross-plane direction to the substrate. Most of the studies, so far, have been geared towards improving the room-temperature (RT) mobility and TBC of FL 2D devices. However, modern transistors operate at temperatures much higher than the RT due to self-heating; as a result, their mobility deteriorates significantly from their RT values due to the increased electron-phonon scattering. Therefore, to examine the potential of a FL 2D material, it is imperative to perform coupled electro-thermal studies where one can probe power dissipation and temperature rise simultaneously to assess the mobility of the device under actual operating conditions.

I chose tungsten diselenide (WSe_2) as the representative material because it exhibits the highest carrier mobility among all TMDs. It also has high on-off ratio—a desirable characteristic for transistor applications. WSe_2 has large charge-screening length (λ_{TF}) which means the induced carriers in the FL WSe_2 stack due to the applied gate voltage would spread over more number of layers. Because of large λ_{TF} in FL WSe_2 devices the top layers carry majority current whose contribution to the TBC is fairly poor. The mobility in WSe_2 is strongly temperature-dependent; as a result, there is significant temperature rise in the top layers causing its mobility to deteriorate. The mobility degradation in the top layers

causes the current to route itself to the bottom layers, where the TBC is higher, resulting in better heat removal and less temperature rise which limits the severity of self-heating and its impact on carrier mobility in FL WSe_2 devices. Our electro-thermal simulations also revealed that a FL 2D material with smaller λ_{TF} and high TBC will be a suitable candidate for next-generation electronic material.

The second part of my dissertation aims at improving thermal management in 2D materials from fundamental perspective. The microscopic interactions between phonons and electrons play a major role in influencing electrical properties of solids and are therefore well studied. However, their impact on phonon transport has received far less attention because they are generally weak except at cryogenic temperatures. Recent studies suggest that phonon-electron scattering can significantly reduce the in-plane thermal conductivity in materials like silicon and its 2D counterpart, silicene. However, the heat removal in devices made up of 2D materials takes place in the cross-plane direction. For cross-plane thermal conduction, the internal resistance due to phonon-phonon interactions is found to be the bottleneck. A significant phonon-electron scattering can reduce the internal resistance and boost its TBC. To examine it, I calculate phonon-electron scattering from the phonon dispersion calculated from first principles and then studied its impact on TBC between a 2D material and a substrate. Our results show that among TMDs, the TBC of MoS_2 exhibits the maximum enhancement of about 36% when the carrier density is increased from 10^{14} to 10^{18} m^{-2}. This provides a novel tool to dynamically tune TBC between a 2D material and a 3D substrate via electrostatic gating.

Thermal conduction in solids is mainly considered to be diffusive in nature where the quasiparticles carrying heat, called *phonons*, lose their momenta due to collisions with the underlying lattice. These momentum-relaxing scattering processes are called umklapp scattering. A strong fraction of momentum-relaxing collisions is a signature of diffusive transport. However, under special conditions such as cryogenic temperatures, a large fraction of phonons might undergo momentum-conserving collisions, therefore carrying heat

over a longer characteristic length called mean-free-path, and hence it may lead to a higher thermal conductivity. Such fluid-like thermal transport in solid is referred to as hydrodynamic transport. Recently, researchers have found graphene to exhibit hydrodynamic transport at around 100 K, which is much higher than cryogenic temperatures. Phonon hydrodynamics at higher temperatures has received significant attention because it may now be used for practical applications. Since hydrodynamic transport is a wave-like phenomenon, it is more rational to study thermal conductivity in the frequency domain. In my dissertation, I derived an expression for thermal conductivity in 2D materials by solving Boltzmann Transport equation, which governs heat conduction in solids, in frequency domain. We quantified the range of frequencies of temperature gradient, where normal scattering is more dominant than umklapp scattering, which supports hydrodynamic transport in graphene ribbons. The method also provides an unique opportunity to perform phonon lifetime spectroscopy.

The principle "*Smaller is better* is not only applicable for transistors, but for interconnects as well. Along with shrinking the dimensions of transistors, the dimension of interconnects and wires, typically made of copper, has also shrunk. Current state-of-the-art technology uses copper interconnects as thin as 10 nm. However, the resistivity of copper increases exponentially below 100 nm. On the other hand, graphene ribbons exhibit lower resistance at similar linewidths, which makes them promising candidates for interconnects in the next-generation integrated circuits. Mass production of graphene is achieved via chemical vapor deposition technique (CVD). Unfortunately, CVD-grown graphene are, inherently, polycrystalline in nature. The large film consists of several grains, each having different crystal orientation and size, which are separated from each other by grain boundaries (GBs). The relative mismatch in the crystal orientations of the adjacent grains, typically referred to as misorientation angle Θ_M, is expected to play a significant role in determining the electrical properties of a polycrystalline material.

In this dissertation, I first studied the impact of misorientation angles on the GB resistivities (ρ_{GB}) of 2D materials where the GBs were assumed to be straight lines. We found that Θ_M alone does not determine the GB resistivity rather it is the pair of angles that the physical GB makes with the crystal orientations of each grain which governs ρ_{GB}. Symmetric GBs are found to be highly conductive approximately equal to the ballistic conductance. Asymmetric GBs are resistive—the resistivity increases exponentially with the degree of asymmetry. In graphene, they exhibit stronger angle dependence than those in MoS_2. In practice, GBs are straight lines only in microscopic regions, however, over an extended region, GBs are never straight lines. Consequently, the prediction of ρ_{GB} differ significantly from experimental measurements, especially for asymmetric GBs. Here I used two different approaches to simulate extended GBs in graphene and then integrated them with the electrical transport model developed by me to compute GB resistivity. Our results revealed that the resistivity is inversely proportional to the effective slope of the GB, which is given by the ratio of the rms roughness and correlation length. The segments which symmetrically divide the grains destroy the correlation between the resistivity and misorientation angles which we found in our previous study on straight-line GBs. We calculated the resistivity for extended GB to lie between 10^2 to 10^4 Ω μm, which aligns well with the measured resistivity values found in the literature.

TABLE OF CONTENTS

LIST OF FIGURES

Figure **Page**

CHAPTER 1

INTRODUCTION

1.1 Moore's law: Roadmap for semiconductor industries

Gordon E. Moore's famous 1965 essay states that the number of transistors on a microprocessor chip will double itself every year. In 1975 after co-founding Intel Corporation, he revised his prediction of doubling chips to approximately two years. Doubling the number of transistor count on a given area means each transistor's area needs to be scaled to half. In 1974, Robert H. Dennard proposed a scaling law where each transistor dimension is reduced by 30% (0.7x) and thus the area by 50% (Figure 1.1(a)), and observed a 40% reduction in circuit delays making devices 40% faster. To keep the electric field constant, the operating voltage is reduced to 0.7x, which implies the power consumption is reduced by 50%. Thus, for double transistor count, the device becomes 1.4x faster and power consumption remains the same. Moore's prediction combined with Dennard's scaling law transformed the crude computing devices of 1950's and 1960's, mainframe and minicomputers, to sophisticated personal computers and laptops in early 1980's (Figure 1.1(b)). The dynamic power consumption of CMOS circuits is proportional to the clock frequency. Simultaneously shrinking device dimensions and operating voltage allowed the chip manufacturers to aggressively ramp up the clock frequencies without impacting power consumption. It was around 2005 Dennard's scaling law started to breakdown when the increase in performance achieved by increasing clock frequency caused the chips to heat up and posed a threat of thermal runaway. Since then, although the manufacturers stopped increasing clock frequency to boost performance but the transistor size kept on shrinking as per Moore's law until 2016. Recently, the smallest feature size in a transistor has reached

few nanometers (TSMC, a chip manufacturing company based on Taiwan, are etching 7 nm transistors and 5 nm ones are there in their list). We are already down to few tens of atoms where quantum uncertainties alter electron behavior; if shrinkage continues then eventually (in next few generations) we will run out of atoms. Several efforts have been made to preserve Moore's law including multicore processors and 3D architectures with processor and memory on the same chip. A different approach comes from materials perspective which strives for finding a "millivolt switch"—a material that could be used for transistors which are at least as fast as their contemporary silicon counterparts, but that would generate much less heat.

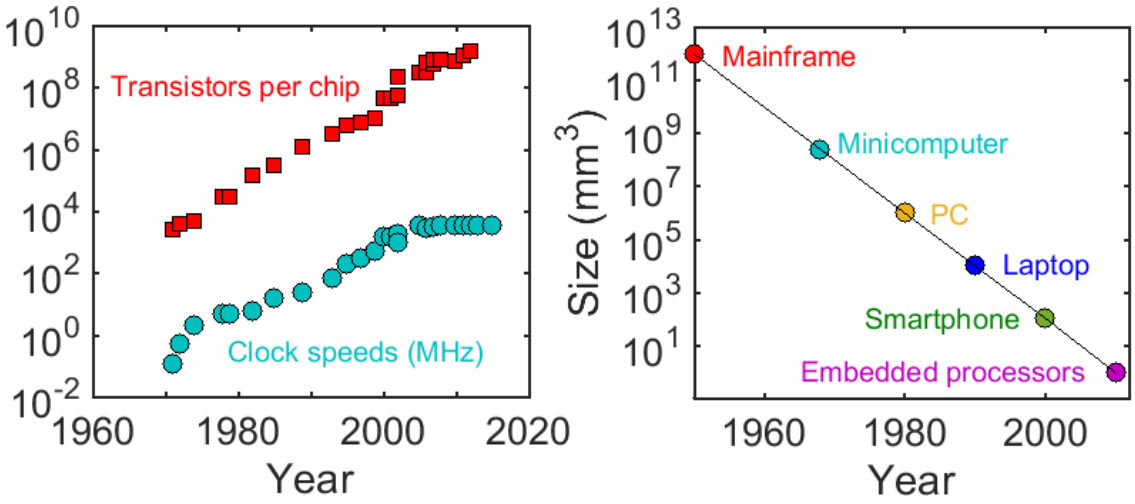

Figure 1.1: **(a)** Evolution of processing power (number of transistors per unit chip area and clock frequencies) for last last five decades followed Moore's law. **(b)** New generation of machines emerged every ten years while the transistors were shrinking every two years. (adapted from Mitchell et al. [1])

1.2 Emergence of two-dimensional materials

Although the idea of graphene (a single layer of graphite) existed theoretically for several decades, it was believed that crystalline two-dimensional (2D) materials, including graphene, could not exist in nature because of thermodynamical instability [15]. It was in

2004, when a group of scientists from University of Manchester in United Kingdom and Institute for Microelectronics Technology in Russia successfully separated a single layer from bulk graphite for the first time [16]. Their groundbreaking work resulted in the 2010 Nobel Prize in Physics being awarded to Novoselov and Geim. They followed it up by preparing single-layer exfoliated forms of other van der Waals 2D atomic crystals, including transition metal dichalcogenides (TMDs) such as MoS_2 and $NbSe_2$, and boron nitride [17]. This cohort of 2D materials includes graphene, hexagonal boron nitride (hBN), and transition metal dichalcogenides (TMDs), which have covalent in-plane bonds and weak van der Waals (vdW) bonds across atomic planes. The weak interlayer coupling allows these vdW monolayers to be separated, manipulated, and assembled into vertical and lateral heterostructures. These materials have a host of unique and superlative electronic, optical, thermal, and thermoelectric properties, thus forming a basis for future low-power logic devices, high-efficiency energy materials, and high-performance optoelectronics.

The unique electronic structure of graphene, where the low energy charged carriers mimic relativistic particles with zero rest mass having an 'effective speed of light' of 10^6 ms^{-1} [18], along with experimental demonstrations of integer quantum Hall states [19] and Klein tunneling [20], not only opened up avenues for rich, fundamental science but also led to a possibility of realizing new electronic and magneto-electronic device applications. Earlier reports suggested that carrier mobilities, which were found to be about 15,000 $cm^2V^{-1}s^{-1}$ for both electron and holes, were independent of temperature over the range between 10 and 1000 K [18], suggesting a very strong influence from the interaction with the underlying substrate. This has led to a series of studies trying to establish the upper bound of the intrinsic phonon-limited mobility by fabricating and measuring highly crystalline, suspended graphene [21, 22, 23].

1.3 Charge impurity scattering in monolayer TMDs

An electron mobility of 230,000 cm^2 V^{-1} s^{-1} at a carrier concentration of 2×10^{11} cm^{-2} is among the highest ever measured mobility in suspended graphene [21]. This value is considered as the phonon-limited upper bound [24]. Despite such high mobilities, the weak electrostatic gating and absence of band gap makes it an undesirable candidate for 2D field-effect transistor (FET). However, it did not deter scientific community from continuing research on graphene because of its rich and unique fundamental physical properties. On the other hand, the inherent band gap of TMDs made them promising candidates for making FETs. So, researchers turned to this new family of 2D materials based on TMDs. Early studies of MoS_2 found significantly lower mobility but with a much better electrostatic control. The subsequent introduction of a substrate [25, 26, 27, 28] for better electrostatic gating provided an opportunity to measure large-area graphene sheets, although substrate impurity [29], interface, and remote phonon scattering [30] significantly reduce carrier mobility.

An avalanche of experiments have been conducted to fabricate defect- and impurity-free samples, which demonstrated a significant increase in mobility. [31, 32, 33] For low impurity concentrations, and especially at high temperatures, the mobility is found to approach phonon-limited value of about 400 $cm^2V^{-1}s^{-1}$ in monolayer MoS_2. In this regime, the mobility is dominated by remote-optical phonon scattering. It has been shown that encapsulating MoS_2 with HfO_2 [34] or Al_2O_3 [35] improves mobility because the encapsulation shields the monolayer from charged impurities in the substrate. An alternative route to circumvent the effect of charged impurity scattering is to use few-layered (FL) TMDs where the bottom layers shield the top layers from the charges in the substrate. Consequently, FL TMDs exhibit improved mobility as compared to its single layer counterparts.

1.4 Heat Dissipation in FL 2D Materials

Despite their superior electrical mobilities, thermal management in devices based on FL TMDs remains a critical issue in their development and implementation in next-generation electronic devices [36, 37]. Owing to the weak van der Waals forces between layers, heat dissipation in FL TMDs is more complex because each layer carries a different current [38], resulting in highly non-uniform Joule heating in the stack. Heat removal in 2D FETs is mainly cross-plane through the substrate due to the small thermal healing length (a measure of heat spreading, around 100 nm) [39] and large lateral/vertical aspect ratio [40, 41]. Heat dissipated by electrons is carried to the substrate via quantized lattice vibrations, or *phonons*, whose transmission is further limited by: (i) large difference between the phase spaces of the 2D material and the 3D substrate [42], (ii) small overlap between their vibrational densities of states [43], and (iii) mechanical mismatch between the stiff substrate and soft out-of-plane flexural phonon modes [44], which transfer most of the heat across the interface. Consequently, thermal boundary conductance (TBC) between the 2D material and the substrate, typically between 12 and 27 $\mathrm{MWm^{-2}K^{-1}}$, is the main bottleneck for heat removal [44, 41, 45, 46]. For FL TMDs to potentially replace silicon in the next-generation electronic devices, it is imperative that we find a TMD which exhibits not only high carrier mobility but also high TBC. Therefore, it is necessary to solve for the charge and heat current simultaneously in FL TMDs and examine the materials which could be a potential candidate for future electronic devices.

1.5 Improving Thermal Management Using Fundamental Physics

1.5.1 Phonon-Electron Coupling

Electron-phonon scattering plays an major role in determining electrical resistance of a material. Their interactions have received less attention for phonon transport because it is believed that such processes can impact thermal conductivity only at sub-zero temperatures. But recent reports on reduction of in-plane thermal conductivity at room temperature in

silicon [47] and 2D materials like silicene [48] have revived interests in the interactions of phonons and electrons, especially in 2D materials. While a strong coupling between them is detrimental to in-plane transport, phonon-electron interactions can reduce the internal resistance (due to the interaction of quasiparticles in the 2D material itself), which is found to be the bottleneck to TBC of most 2D materials on SiO_2, and enhance their TBC. This motivated me to conduct a study to examine the effect of phonon-electron coupling on TBC in 2D materials which, until now, is completely unexplored.

1.5.2 Phonon Hydrodynamics

In solids, including 2D materials, heat is known to flow diffusively through lattice vibrations (phonons). In diffusive regime, phonons lose their momentum on interacting with the underlying lattice, that is, other phonons. Mean-free-path (MFP)—an average characteristic length over which phonons can travel in a solid without scattering—determines the thermal conductivity (κ) of a solid; larger MFP translates to a larger κ. More than fifty years ago, phonons in insulators and electrons in metals were found to exhibit wave-like behavior under special conditions such as cryogenic temperatures where momentum-conserving collisions (normal scattering) among phonons become more prominent than momentum-relaxing (umpklapp) scattering. As a result, phonons exhibit larger MFP and hence larger thermal conductivity which is critical for variety of thermal and electronic applications. Such wave-like transport in solids is often referred to as *phonon hydrodynamics*. In recent years, phonon hydrodynamic transport has become a subject of renewed interest because of evidence of it in graphene at temperatures much higher than cryogenic temperatures. Since hydrodynamic transport is a wave-like phenomenon, it is more rational to study thermal conductivity in the frequency domain. In my dissertation, I derived an expression for thermal conductivity in 2D materials by solving Boltzmann Transport equation, which governs heat conduction in solids, in frequency domain. We quantified the range of frequencies,

where normal scattering is more dominant than umklapp scattering, which supports hydrodynamic transport in graphene ribbons.

1.6 Scope of Polycrystalline Graphene as an Electronic Material

On-chip interconnects and vias between layers in 3D stacking architecture are becoming increasingly challenging due to the downscaling of interconnects in modern ultra-large scale integration. A few years ago, the performance of an integrated circuit was mainly determined by the gate delays until recently when the interconnect delays are becoming more prominent due to increasing parasitic effects. The primary requirement for a material to be used as interconnect is excellent electrical conductivity, and thus metals like copper and tungsten were the obvious choices. In recent years, the resistivity of interconnects, typically made of copper, has increased significantly due to surface roughness and grain boundary (GB) scattering, especially below 100 nm [49]. Because of the superior electrical properties of graphene, graphene nanoribbons (GNRs) are proposed to be the most promising candidates for future interconnect materials. For commercial applications, waferscale-sized graphene is required and chemical vapor deposition (CVD) is the most inexpensive and popular method to grow such large-area graphene. Because of the inherent nature of this method, CVD-grown graphene is polycrystalline in nature, which makes it essential to understand the effect of GBs on electron transport. In this dissertation, I developed a numerical transport model to decipher the impact of GB misorientation angles on electron flow in 2D polycrystalline structures. Large variations in GB resistance for different misorientation angles could raise serious reliability issues in future integrated circuits where the interconnect delays significantly impact their performance.

CHAPTER 2

ELECTRO-THERMAL MODELING IN FEW LAYER TWO-DIMENSIONAL MATERIALS

The on-going quest for faster switching, higher density, and better performance has led to persistent downscaling of nanoelectronic devices. Shrinking the device dimensions increases their surface-to-volume ratio [50] and introduces atomic-scale disorder at boundaries and interfaces [51, 52], reducing performance and threatening to limit scaling. To avoid these issues, the nanoelectronics community has turned to intrinsically 2D materials platforms. The ultrathin nature of 2D materials facilitates device downscaling [53] and vertical stacking [27, 54], which could extend Moore's law and enable high-density device integration for modern integrated circuits. Atomic flatness and the absence of dangling bonds [55] prevent scattering of carriers by surface roughness (SR), which limit mobility in ultra-thin body 3D silicon-on-insulator (SOI) field-effect transistors (FETs)[56]. Graphene exhibits superlative thermal [57] and electrical conductivity [21], flexibility [58], and optical transparency [59] but lacks a bandgap, which is a basic requirement for switching and logic applications. In contrast, TMDs have an intrinsic energy bandgap which makes them preferable candidates for applications in digital logic[60, 61], NEMS [62], optoelectronics [63], photovoltaics [64], spin- and valleytronics [65, 66]. Despite their immunity to SR scattering, single-layer (SL) TMDs typically exhibit degraded carrier mobility [17] relative to bulk due to strong Coulomb scattering from charged interfacial impurities [67, 68]. Measured room temperature (RT) mobilities of SL MoS_2 on SiO_2 substrates [69, 70] range from 0.1 to 55 $cm^2V^{-1}s^{-1}$. Significant research efforts have been invested towards growing high-quality, impurity- and defect-free samples [71, 72]. Another route is encapsulating

the SL with a 2D insulator, such as graphene sandwiched between two sheets of hexagonal boron nitride (hBN) [27], but these methods are time-intensive and expensive.

A viable alternative is to use FL TMDs, in which the bottom layers act akin to encapsulation, screening the layers above from impurities. Due to this self-encapsulating nature, carrier mobility improves significantly in FL TMDs [73, 74], with the highest RT field-effect mobility on SiO_2 attained in FL tungsten diselenide (WSe_2) FETs reaching 350 $cm^2V^{-1}s^{-1}$ [75]. Above RT, mobility in FL TMDs is limited by phonon scattering and decreases nearly quadratically with temperature [76]. Despite their superior electrical mobilities, thermal management in devices based on FL TMDs remains a critical issue in their development and implementation. High lateral voltages increase Joule heating and cause transistors to self-heat, a process which, if unchecked by heat removal, can be highly detrimental to mobility and device performance [36, 37]. Heat dissipation in FL TMDs is more complex because each layer carries a different current [38], resulting in highly non-uniform Joule heating and temperature rise among layers. Current in FL graphene [77] and MoS_2 [78] is vertically localized in a few layers, causing a hotspot, where the location and spread of this hotspot depends on gate voltage via carrier concentration in each layer.

Heat removal in 2D FETs is mainly cross-plane through the substrate, owing to the small thermal healing length of around 100 nm [39] and large lateral/vertical aspect ratio [40, 41]. Interactions between the atoms on the two sides of the interface are governed by van der Waals (vdW) forces, which are weaker than covalent bonds and thus known for reducing interface thermal transport [17, 68]. Heat dissipated by electrons is carried to the substrate via quantized lattice vibrations (phonons), whose transmission is further limited by the large difference between the phase spaces of the 2D material and the 3D substrate [42], small overlap between their vibrational densities of states [43], and the mechanical mismatch between the stiff substrate and soft out-of-plane flexural phonon modes [44], which transfer most of the heat across the interface [67]. This causes the TBC between the 2D material and the substrate, typically between 12 and 27 MW $m^{-2}K^{-1}$, to be the

main bottleneck for heat removal [44, 41, 45, 46]. In FL TMDs, layers farther from the substrate are partially insulated by layers below them and thus contribute less to TBC [79], but measurements to date only provide us with the average temperature rise of the entire stack through Raman thermometry [80].

To fully understand heat removal in FL 2D FETs, it is imperative that we quantify the temperature rise in each layer of the stack. Moreover, the effect of self-heating on electrical performance of each layer in FL 2D devices remains unexplored. In this work, we study Joule heating and thermal management in FL FETs built from WSe_2 and extract their layer-dependent temperature rise to elucidate its impact on performance. We employ a resistance-network model to understand the current distribution in a FL TMD FET and extract parameters for our model by fitting experimentally measured I_D-V_{DS} characteristics of the device operating under low-field conditions; the experimental measurements were done at my collaborators at University of Illinois Chicago (Prof. Amin Salehi-Khojin's lab). Then we employ the resistance-network model to study the effects of self-heating under high-field conditions. We use a layer-resolved TBC model developed in our previous work [80, 81] to calculate the temperature rise in each layer of the device due to self-heating. The calculated temperatures were validated against experimentally-measured average temperature rise. At large bias voltages, the temperature rise in layers near the top of the stack, which are carrying the majority of the current, increases significantly, which deteriorates the mobility of these layers. We uncover an interesting dual behavior of the hotspot caused by Joule heating: at small drain biases, the hotspot shifts towards the top layers with increasing gate voltage, whereas at high drain biases, the temperature rise and mobility degradation cause the hotspot to re-route towards the bottom layers to minimize self-heating. We also found that, unlike SL TMDs, there is a considerable amount of heat removal through the contacts in FL TMD FETs, even in those with long channels, due to longer thermal healing length of top layers.

2.1 Results

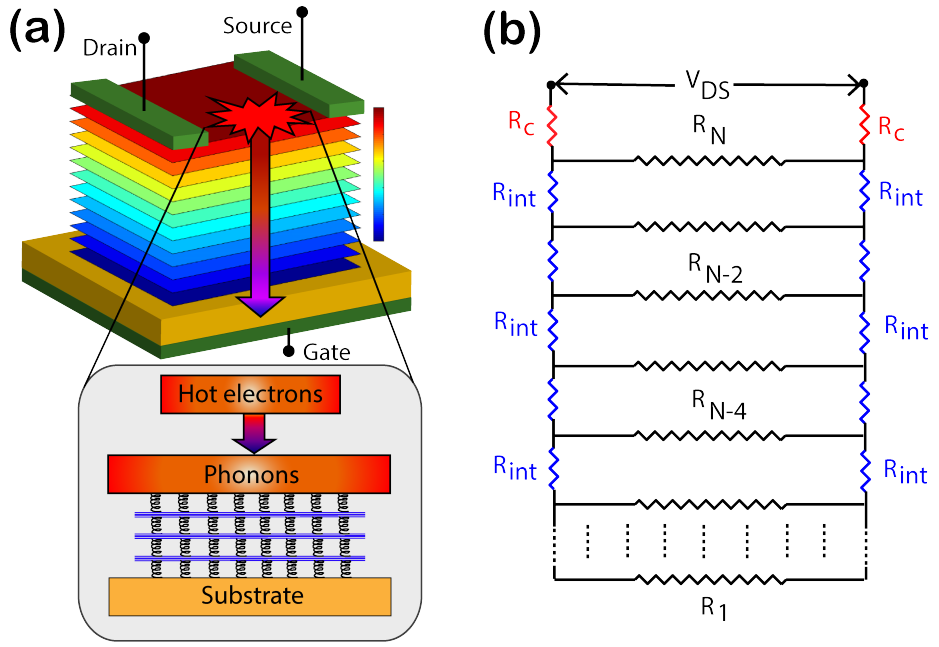

Figure 2.1: **(a)** Schematic depiction of a FL 2D FET device configuration showing non-uniform current distribution across various layers. **(b)** shows the resistance-network model used to represent the FL 2D FET.

2.1.1 Layer-dependent Electrical Properties of FL WSe_2

In this work, we consider a typical back-gated device configuration, shown schematically in Figure 2.1**(a)**. The metal source and drain contacts are deposited on the topmost layer and the current is injected from the top through contact resistances $\mathrm{R_c}$ between the metal and the TMD, assuming an ohmic contact. Each layer in the stack has a different resistance $\mathrm{R_i}$, where 'i' refers to the i'th layer in an N-layered stack, depending on its local carrier concentration, mobility, and temperature. Current encounters an additional resistance $\mathrm{R_{int}}$ to access the next layer. A resistor-network model represents the current flow through the FL stack, as shown in Figure 2.1**(b)**. The extent of current penetration through the stack would depend on the strength of $\mathrm{R_{int}}$ with respect to the layer resistances $\mathrm{R_i}$. $\mathrm{R_i}$ is the product of carrier concentration n_i and mobility μ_i of that layer, $\mathrm{R_i} = [qn_\mathrm{i}\mu_\mathrm{i}(T)]^{-1}(L/W)$. The total charge on the gate is $\mathrm{Q_{tot}} = \mathrm{C_{ox}}(\mathrm{V_{GS}} - \mathrm{V_T})$, where

C_{ox} is the capacitance per unit area of the oxide and V_T is the threshold voltage. However, charge screening causes the distribution of carriers across layers to be highly non-uniform. Carrier concentration is highest in the bottommost layer and decreases exponentially with each additional layer, given by the ratio [38] $n_{i+1}/n_i = \exp(d_{FL}/\lambda_{TF})$, such that the total charge induced in the channel is equal to the charge on the gate, $Q_{tot} = q\sum_i n_i$. d_{FL} is the layer thickness of WSe_2, 0.645 nm, and λ_{TF} is the Thomas-Fermi (TF) screening length. Analogously, mobility in the bottommost layer [$\mu_1(n_i)$] is primarily limited by charged-impurity (CI) scattering [82]; mobility increases in the layers away from the substrate as the charged impurities are screened by layer charges, approaching the phonon-limited bulk mobility $\mu_\infty(T_i)$, which depends on the temperature of each layer. Its dependence was experimentally determined to follow a power-law $\mu_\infty(T_i) = \mu_\infty(300) \times (T_i/300)^{-\gamma}$ with γ=1.9 [83].

2.1.2 Coupled Electro-thermal Model

The mobility of individual layers is expressed as [38]

$$\mu_i(n_i, T_i) = \mu_1(n_1, n_{imp}) + [\mu_\infty(T_i) - \mu_1(n_1, n_{imp})]\left[1 - \exp\left(-\frac{(i-1)d_{FL}}{\lambda_{TF}}\right)\right], \quad (2.1)$$

where μ_∞ and μ_1 are the bulk and SL mobilities of WSe_2, while T_i and n_i are the temperature and carrier concentration in the i'th layer, respectively. The SL mobility is calculated based on our previous work [84], which includes acoustic, optical, and remote surface optical phonon, as well as CI scattering. Using this resistive network model, we fit our calculated I_D-V_{DS} curves at low lateral fields for different gate voltages to experimentally measured values to obtain R_{int}, λ_{TF} and μ_∞, which are inputs to the model. The experimental measurements were performed by my collaborator, Zahra Hemmat at Prof. Amin Salehi-Khojin's lab, in University of Illinois Chicago. To capture both lateral and cross-plane heat conduction, and their impact on the mobility of each layer, we calculate the temperature rise in each layer of the FL stack from

$$\Delta T_i = \left(\frac{Q_i}{WL}\right) \times \frac{1}{G_i}\left[1 - \frac{2L_{H_i}}{L} tanh\left(\frac{L}{2L_{H_i}}\right)\right] \tag{2.2}$$

where WL is the surface area of the WSe_2 layers and $\mathrm{L_H}$ is the thermal healing length. The derivation of the thermal healing length is detailed in the appendix. Healing length is calculated as $\mathrm{L_{H_i}} = \kappa_{\mathrm{in}} \times \mathrm{d_{SL}}/\mathrm{G_i}$, where κ_{in} is the in-plane thermal conductivity of WSe_2, which is 53 $\mathrm{Wm^{-1}K^{-1}}$ [85]. Depending on the average temperature rise of each layer $\Delta\mathrm{T_i}$, we update the layer mobilities μ_i in Eq. 2.1, and then re-calculate the layer resistances $\mathrm{R_i}$. Based on the updated $\mathrm{R_i}$, we re-compute $\mathrm{Q_i}$ and $\Delta\mathrm{T_i}$. Using this electro-thermal coupling, we set up an iterative loop where we update $\Delta\mathrm{T_i}$ based on the $\mu_\mathrm{i}(\mathrm{n_i}, \mathrm{T_i})$ of the previous iteration. We continue until total Joule heating $\sum_\mathrm{i} \mathrm{Q_i}$ reaches convergence, typically taking between 5 to 15 iterations.

Here, WSe_2 was selected as a representative TMD because of its high carrier mobility [86] and good stability to oxidation in ambient conditions [87]. The parameters for our resistance-network model $\mathrm{R_{int}}$, λ_{TF}, and μ_∞ are extracted from fitting the current-voltage curves of exfoliated FL WSe_2 flakes which were transferred onto a Si-SiO_2 substrate. The details on fabrication of these devices can be found in [88]. On fitting our calculated $\mathrm{I_D}$-$\mathrm{V_{DS}}$ curves to the experimentally measured data, we obtain $\mathrm{R_{int}}$ of 5958 $\Omega\ \mu\mathrm{m}$, μ_∞ = 114 $\mathrm{cm^2V^{-1}s^{-1}}$, and a TF screening length λ_{TF} = 13 nm.

2.1.3 Joule Heating and Layer-resolved Temperatures

Once we extract the values of both intra- as well as inter-layer resistances, we calculate the current distributions across all the layers and obtain their layer-specific Joule heating $\mathrm{Q_i} = \mathrm{I_i^2 R_i}$. Self-heating is significant in two operating conditions: when the overdrive voltage $(\mathrm{V_g} - \mathrm{V_T})$ is smaller than $\mathrm{V_{DS}}$ and the carriers are pinched-off near the drain contact, and when $\mathrm{V_g} - \mathrm{V_T} \geq \mathrm{V_{DS}}$ but the lateral field $(\mathrm{V_{DS}/L})$ is large enough for the carrier drift velocity to reach the saturation region, $\mathrm{v_d} \rightarrow \mathrm{v_{sat}}$. The average lateral field beyond which the device is driven into velocity saturation is given by [89] $(\mathrm{V_g} - \mathrm{V_T})/\mathrm{L} \approx 2\mathrm{v_{sat}}/\mu_{\mathrm{eff}}$.

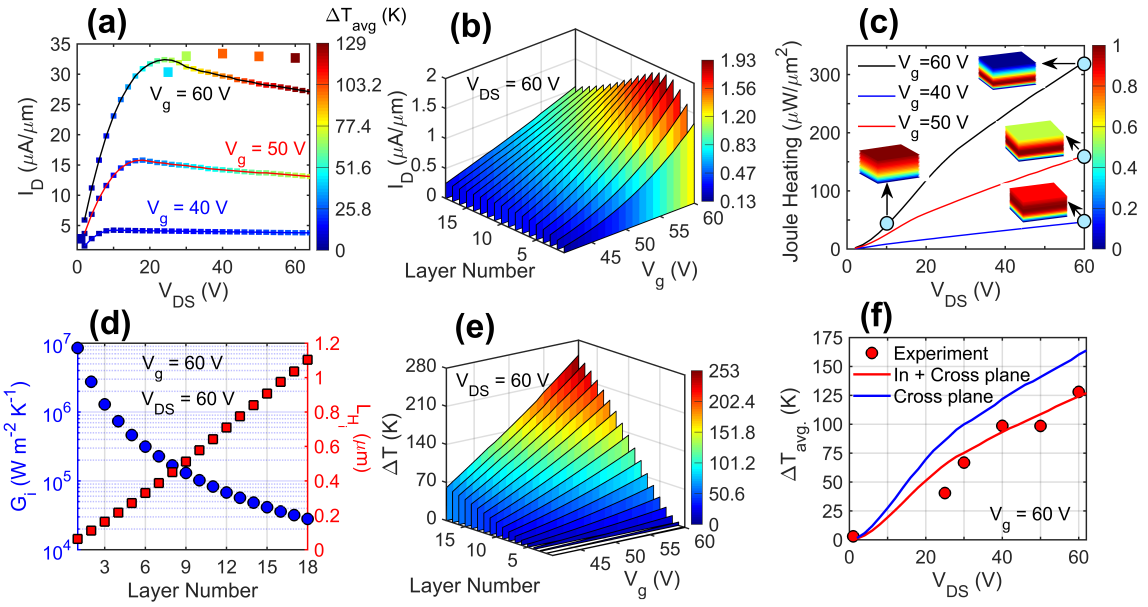

Figure 2.2: **(a)** shows I_D-V_{DS} output characteristics in 18-layer WSe_2 with different V_g calculated at room temperature (300 K). The color of square markers represent the rise in average device temperature ΔT_{avg} at each V_{DS} and V_g. Large square colored markers denote experimentally measured I_D and ΔT_{avg} with V_{DS} at V_g equals 60 V. **(b)** shows the drain current per layer for different gate voltages V_g at V_{DS} equal 60 V. **(c)** shows Joule heating vs. V_{DS} at different V_g. The insets show Joule heating among layers at different V_{DS} and V_g. **(d)** shows thermal boundary conductance G_i (left y-axis) and thermal healing length L_H (right y-axis) of each layer in an 18-layer WSe_2 stack. **(e)** shows temperature rise in each layer for different V_g at V_{DS} equal to 60 V. **(f)** shows calculated (red curve) and measured (red circles) average temperature rise of the stack vs. V_{DS} at V_g equals 60 V. The blue curve represents the average temperature rise if the heat removal was entirely cross-plane.

Thus, the critical device length (L_{crit}) for velocity saturation in FL WSe_2 is 3.5 μm, where v_{sat} in FL TMDs is about 3×10^6 cm^2 V^{-1} s^{-1} [90, 91]. In this work, we chose a long-channel device (L=4.9 $\mu m > L_{crit}$) such that the carriers are not driven into velocity saturation. Figure 2.2**(a)** shows the drain-source characteristics for different gate voltages at RT (300 K). With the increase in V_{DS}, there is increased Joule heating and the average device temperature ΔT_{avg}, denoted by the color of square markers on top of the $I_D - V_{DS}$ lines in Figure 2.2**(a)**, rises. The large square markers represent the experimentally measured drain-source characteristics at V_g=60 V, and the marker color denotes the measured aver-

age temperature rise of WSe_2 with respect to the substrate, which was obtained from Raman thermometry. We found that at large $\mathrm{V_g}$ (=60 V) there is an increase in Joule heating due to higher carrier concentration and the $\Delta \mathrm{T_{avg}}$ reaches as high as 130 K. In Figure 2.2**(b)**, we show that the current distribution among layers is non-monotonic for large $\mathrm{V_{DS}}$=60 V, especially at large gate bias. Due to strong TF screening and $\mathrm{R_{int}}$, the top layers carry higher currents at large $\mathrm{V_g}$, resulting in an increased Joule heating and temperature in these layers. This deteriorates their mobilities, and the current penetrates lower into the stack as $\mathrm{V_g}$ is increased. In Figure 2.2**(c)**, we plot Joule heating against $\mathrm{V_{DS}}$ for the same gate voltages as Figure 2.2**(a)**. We find that the distribution of Joule heating among layers shows a distinct variation with $\mathrm{V_g}$ and $\mathrm{V_{DS}}$, as shown by the insets in Figure 2.2**(c)**, where Joule heating, normalized by its maximum value, is schematically depicted for different gate and source-drain voltages. While for small $\mathrm{V_g}$ heat is mostly concentrated in the top layers, increasing $\mathrm{V_g}$ causes dissipation to become concentrated in the bottom layers.

To understand these trends, we next delve into the temperatures ΔT_i in each layer. We used layer-dependent TBC values ($\mathrm{G_i}$), calculated from our first-principles FL thermal transport model [81, 80]. In Figure 2.2**(d)**, we plot $\mathrm{G_i}$ and observe that most conductance is contributed by the bottom layers, with $\mathrm{G_i}$ decaying approximately quadratically with distance from the substrate. The total $\mathrm{G_{tot}} = \sum_\mathrm{i} \mathrm{G_i}$=15 MW m^{-2} K^{-1}, in good agreement with Raman measurements, and the TBCs exhibit only a weak increase with T_i above RT [44, 92]. The TBC of the top layer is about two orders of magnitude lower than the layers close to the substrate because heat has to traverse all the weak vdW bonds of the layers in series below it. The average temperature rise of each layer, calculated from Joule heating via Eq. (2.2) in Methods, is plotted for varying gate-bias conditions at $\mathrm{V_{DS}}$=60 V in Figure 2.2**(e)**. ΔT_i shows a strong layer-dependence for large gate voltages ($\mathrm{V_g} = 60\mathrm{V}$), indicating significant self-heating near the top of the FL stack, far exceeding the average. Although there is significant Joule heating in the bottom layers [Figure 2.2**(c)**], the temperatures of these layers do not increase significantly because of their higher TBC.

The thermal healing length L_H, which represents the lateral length along the channel over which the temperature increases away from the contact, also shows a prominent layer dependence, plotted on the right axis of Figure 2.2(**d**). L_H of the bottom layer is about 80 nm, comparable to SL TMDs [41], indicating that there is negligible lateral heat conduction in the bottom layers while L_H for the top layer reaches about 1.1 μm, indicating that there is considerable heat removal through the contacts from the top layers. The ratio of power dissipation through cross-plane and in-plane against channel length is also examined; we find Q_{cross}/Q_{in}=5 for L=4.9 μm. Although heat removal through contacts is non-negligible in the upper layers due to their large L_H, cross plane thermal conduction still plays a dominant role and the temperatures of those layers increase tremendously because of their poor TBC. In Figure 2.2(**f**), the average device temperature rise ΔT_{avg}, shown by the solid red line, is plotted as a function of V_{DS} for V_g=60 V. ΔT_{avg} shows a sharp rise for small V_{DS}, but for large drain-source voltage Joule heating shifts towards the bottom layers, which efficiently conduct heat into the substrate, resulting in a smaller rise in ΔT_{avg} with V_{DS}. Our calculated average device temperatures show a good agreement with those obtained from Raman thermometry, represented by red circular markers. The solid blue line represents the average device temperature with V_{DS} if the heat removal was entirely cross-plane into the substrate. The difference stems from lateral heat removal through the contacts, mainly from the top layers due to their large L_H.

2.1.4 Mobility Degradation and Current Re-routing

Earlier, we showed that I_D does not increase quadratically with V_g for a large V_{DS} [Figure 2.2(**a**)], indicating that carrier mobility in the device is not independent of gate bias, especially for large V_{DS}. To elaborate, we plot intrinsic mobility of each layer for different gate biases at V_{DS} equal to 60 V in Figure 2.3(**a**). For small V_g, the mobility is low for the bottom layers because of dominant CI scattering from the substrate. It increases monotonically towards bulk value with layer number due to charge screening from the bot-

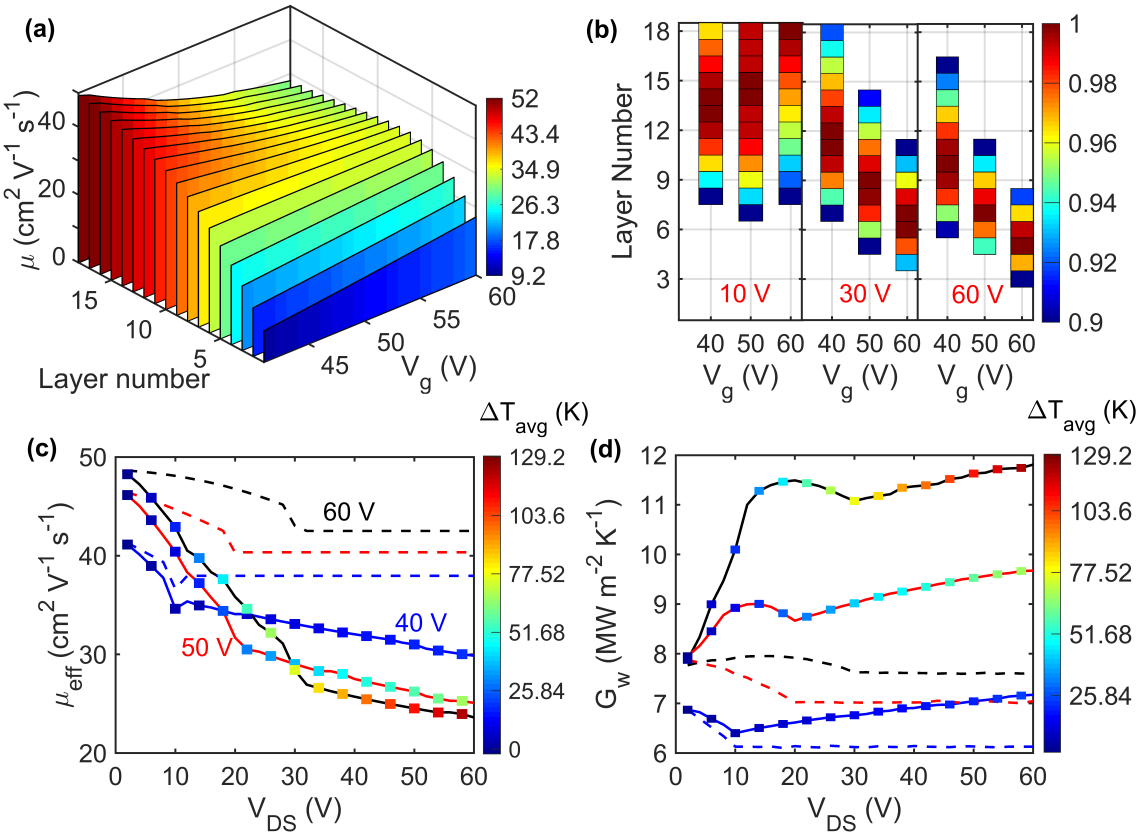

Figure 2.3: **(a)** shows the effect of self-heating on mobility of each layer for different V_g. **(b)** shows the shift in the hotspot in 18-layer WSe_2 with V_g for different V_{DS} (10, 30, and 60 V). Color corresponding to each layer denotes the amount of Joule heating in that layer with respect to the maximum Joule heating. The color bar is scaled from 0.9 to 1 to show the migration of the hotspot in the stack. The effective mobility and weighted TBC of the stack are plotted against V_{DS} for different gate voltages under normal operating conditions with self-heating (solid lines) and isothermal case (dashed lines) in **(c)** and **(d)**, respectively. The blue, red, and black lines represent V_g equal to 40, 50, and 60 V, respectively. The average device temperatures due to self-heating are represented by the marker colors in **(c)** and **(d)**.

tom layers. For large gate bias conditions, the temperature rises significantly for top layers due to self-heating [shown earlier in Figure 2.2**(c)**]. Since layer mobility in Eq. (2.1) is temperature-dependent, it decreases with V_g, showing a peak in the sixth layer when V_g= 60 V. To demonstrate the effect of self-heating, we compare mobility during device operation with the isothermal case (no self-heating). We find that self-heating has negligible impact on mobilities of the bottom layers because of their excellent TBC. However, mo-

bilities of top layers exhibit severe degradation due to self-heating with a 57% reduction in the topmost layer at V_g=60 V.

Interestingly, we found that the migration of the hotspot with V_g exhibits different trends for low and high V_{DS}. Figure 2.3**(b)** shows that at V_{DS} equal to 10 V, the hotspot shifts towards the top layers with increasing gate bias because of the increase in charge concentration in these layers, which was also found earlier in FL MoS_2 [38]. However, at large V_{DS}, the location of the hotspot shows an opposite trend—it migrates towards the bottom layers with increasing V_g, even though charge concentration increases in the top layers. This is a consequence of the mobility reduction in top layers due to self-heating, which forces the current, and hence the hotspot, to move towards the bottom layers. Figure 2.3**(b)** also shows that at small V_{DS}, the layers contributing at least 90% of the peak Joule heating are spread over a wide number of layers with a weak dependence on V_g, while at large V_{DS} the spread decreases from 11 to 6 layers with increasing gate bias and gets localized in a few bottom layers.

To observe the effect of hotspot migration on device performance, we calculate an effective device mobility [89] $\mu_{\text{eff}} = L/(WC_{ox}V_{DS/Dsat})(\partial I_D/\partial V_g\,|_{V_g})$ and plot it in Figure 2.3**(c)**. Relative to the isothermal cases (dashed curves), μ_{eff} of the device decreases significantly due to the average temperature rise with V_{DS} (shown by the colored markers). With increasing V_{DS}, the hotspot migrates toward the bottom layers, whose mobilities are primarily limited by CI scattering, resulting in a decrease of the effective mobility of the device. While μ_{eff} reduces from the hotspot shifting to the bottom layers with V_{DS}, the effective capacity of the FL device to remove heat, which we capture by a dissipation-weighted TBC $G_w = \sum_{i=1}^{N} Q_i G_i / \max_i(Q_i)$, increases, as shown in Figure 2.3**(d)**. We conclude that Joule heating increases temperature and degrades mobility, but the trend is weaker than quadratic because current re-routes into layers closer to the substrate, improving heat removal. There is a trade-off between effective mobility and TBC; we explore computationally how this trade-off varies with the thickness of the FL stack and find that

drive current improves with increasing thickness but effective mobility saturates around 6-9 layers. For comparison, we repeat our calculations for a hypothetical material with a shorter TF screening length of 1 nm and observe improvements in current and mobility, with a peak around 6 layers.

2.2 Conclusions

In summary, we have developed a tightly-integrated experimental and numerical study of Joule heating in FL WSe_2 FETs, allowing us to extract the heat dissipation, thermal conduction, and temperature rise in each layer of the FL stack. The combination of non-uniform heating, caused by top layers having less CI scattering and higher mobility, and layer-dependent TBC results in significant temperature rise toward the top of the FL stack, far exceeding the average. This dramatic layer dependence is driven by the approximately quadratic drop in thermal conductance with distance from the substrate, caused by heat traversing the series of relatively weak interlayer vdW bonds, and offset only partially by the increased role of lateral heat spreading from the top layers into the contacts. Ultimately, this temperature rise reduces mobilities in layers near the top of the stack, where mobility is phonon-limited and exhibits a strong temperature dependence, and causes the current to re-route into layers nearer the substrate as their TBC is higher. In contrast to isothermal and low-field operation, when layer-wise Joule heating and TBC are fully accounted for, the dissipation hotspot moves down as gate voltage, and with it carrier concentration, increases. This means mobility gains from additional layers in the stack are partially offset by self-heating. However, current re-routing improves the effective heat removal as the layers closer to the substrate have higher TBCs. Short-channel FL TMD devices could benefit somewhat from heat removal through the contacts, but a more complete solution may require a carefully-designed heterostructure stack possessing both stronger screening and substrate/interlayer vdW coupling.

CHAPTER 3

IMPACT OF PHONON-ELECTRON COUPLING ON THERMAL BOUNDARY CONDUCTANCE OF 2D MATERIALS

The prospect of vertically stacking [93]—both homogeneous and heterogeneous—vdW materials has opened numerous avenues to engineer them for superior device performance. However, practical realization of electronic devices made of 2D vdW materials is limited by the inefficient thermal dissipation from the 2D material to the substrate. The high interface thermal resistance can cause unreliable performance and even lead to device failure. Significant research interests have been invested towards improving the electronic properties such as mobility, subthreshold slope etc. [21, 69], but heat dissipation has received less attention.

As discussed in chapter 2, heat removal in 2D field-effect transistors is mainly cross-plane through the substrate, especially in long devices, [88, 42] owing to the small thermal healing length [39] and large lateral/vertical aspect ratio [94]. Thermal energy carried by electrons is dissipated to the substrate via flexural out-of-plane lattice vibrations (ZA phonons) and the efficiency of heat transfer is quantified by the inverse of the Kapitza resistance between the 2D material and the substrate, which we call in our work *external TBC*. Electrons interact with the underlying lattice vibrations of the 2D material via phonon-electron scattering and transfer their thermal energy to phonons. The rate of this energy transfer depends on the strength at which the electrons scatter with various phonon modes which we refer to as *internal phonon-electron resistance*. [95] Similarly, the finite scattering strength between different phonon modes (anharmonic phonon scattering) also adds to the internal resistance. The different components of internal resistance are summarized by arrows in the schematic shown in Figure 3.1.

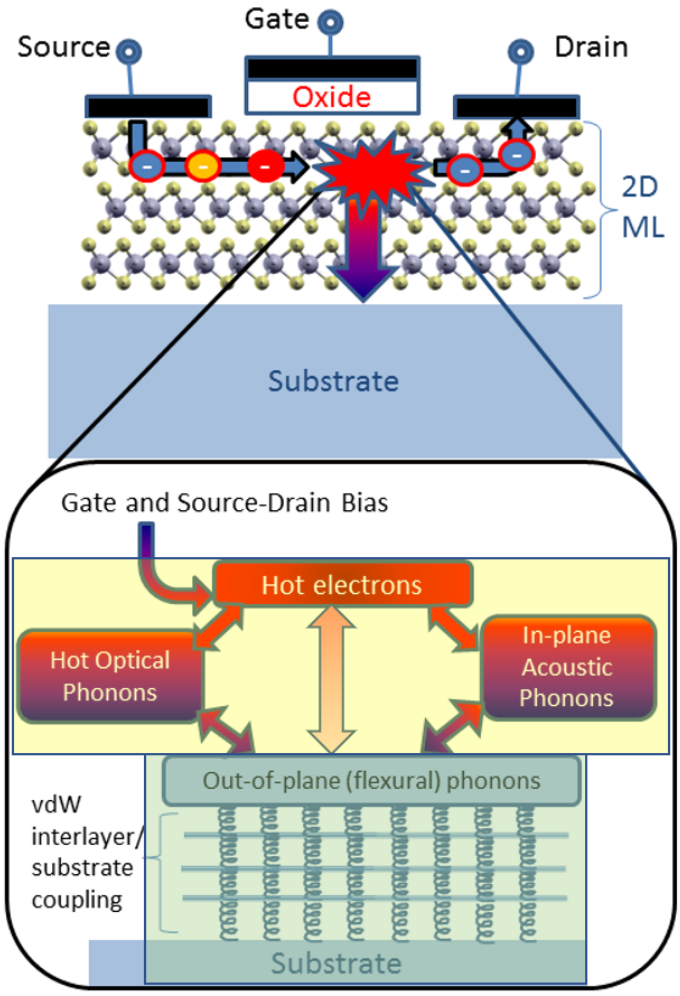

Figure 3.1: **(a)** Schematic depiction of the interplay of electrons and phonons in a few-layered 2D field-effect transistors

Typically, the interaction between electrons and phonons is weak in semiconductors and insulators, except at cryogenic temperatures. It causes the average lattice temperature, which does not exceed beyond a few hundred Kelvin, to be vastly different than that of electrons which is typically one order magnitude higher than phonons. [95] Thus, the poor thermal coupling between them acts as a bottleneck to the cross-plane heat transfer. Moreover, recent measurements revealed that Raman peaks in 2D materials exhibit different temperature-dependent broadening and there exists a strong thermal non-equilibrium between different phonon branches, especially the high-frequency optical phonons and low-frequency ZA phonons. [96] The thermal non-equilibrium between phonon branches indi-

cates that the coupling between them is also weak, which can cause an addition resistance to the heat flow between the 2D material and substrate. Most theoretical studies, so far, have been geared towards improving the external TBC, however, to get a complete picture of the heat transfer between a 2D material and a substrate, it is essential that we quantify the various components of internal resistance and investigate their effect on the total TBC.

In this work, we compute various components of internal resistances and examine their effect on the total TBC. We first calculate the phonon dispersions and electronic bandstructures of various 2D materials from first principles Density Functional Theory using an open-source software package called Quantum ESPRESSO. Then we use the dispersion and bandstructure information to compute the phonon-electron rates for graphene and various TMDs. Then the phonon-electron rates are used to calculate the corresponding internal resistances to the heat transfer from electrons to various phonon modes. A recent study demonstrated lowering of in-plane thermal conductivity of 2D materials via phonon-electron interactions, opening a new avenue to modulate heat transfer by electrostatic gating. [48] Here we also examine the impact of doping on the phonon-electron scattering rates and investigate whether the phonon-electron internal resistance can be reduced by doping. The ability to do so will provide a novel tool to dynamically tune TBC by gating the 2D material.

3.1 Methodology

We calculate the electronic bandstructures and phonon dispersions of 2D materials from first principles Density Functional Theory using the QUANTUM ESPRESSO package [97]. Due to the coupling between the 2D material and the substrate, ZA phonons in the 2D material experience an offset ω_0 in their energies; the effect is dominant only for the long-wavelength ZA phonons. The modified dispersion is calculated as $\tilde{\omega}_{ZA}(\vec{q}) = \sqrt{\omega_{ZA}^2(\vec{q}) + \omega_0^2}$, where the ω_0 is precisely the oscillating frequency of a harmonic oscillator, $\omega_0 = \sqrt{K_a/m_{2D}}$, where K_a is the van der Waals spring coupling constant between

the 2D material and the substrate and m_{2D} is the atomic mass of the 2D material in contact with the substrate. The dispersion of the ZA phonon branch for various TMDs is shown by the red lines in the Figure 3.2. Then we compute phonon-electron rates (Γ_{ph-el}) from Fermi's Golden rule, the derivation is detailed later in this section. Γ_{ph-el} is added to the anharmonic phonon rates in our thermal model [98] to obtain the internal scattering rates Γ_{int}. The details of our thermal model can be found in the appendix section (chapter 7), *Multilayer Thermal Boundary Conductance Model*. Since the bottom-most layer in a multilayer stack has the highest TBC, it is desirable that all the carriers are concentrated in the bottom layer to observe the maximum effect of phonon-electron scattering on TBC. The TBC of a single layer is obtained from the multilayer model in the limit when the number of layers equal to 1. The TBC is then calculated as

$$G = \int \hbar\omega D_{2D}(\omega) \frac{dN_0(T)}{dT} \frac{\Gamma_{sub}(\omega)\Gamma_{int(\omega)}}{\Gamma_{sub}(\omega) + \Gamma_{int(\omega)}} d\omega \tag{3.1}$$

where N_0 is the equilibrium Bose-Einstein distribution, D(ω) is the phonon density of states, and Γ_{sub} and Γ_{sub} are the substrate and internal scattering rates, respectively. Mathematically, the internal rate is calculated as $\Gamma_{int} = \Gamma_{ph-el} + \Gamma_{ph-ph}$.

On rearranging the scattering terms in eq. 3.1, we get

$$G = \int \hbar\omega D_{2D}(\omega) \frac{dN_0(T)}{dT} \left[\frac{1}{\Gamma_{sub}(\omega)} + \frac{1}{\Gamma_{int}(\omega)} \right]^{-1} d\omega. \tag{3.2}$$

The external TBC G_{ext} is calculated in the limit when $\Gamma_{int} \gg \Gamma_{sub}$. Mathematically, G_{ext} is obtained by replacing $\Gamma_{int} \to \infty$ in eq.3.2.

$$G_{ext} = \int \hbar\omega D_{2D}(\omega) \frac{dN_0(T)}{dT} \Gamma_{sub} d\omega. \tag{3.3}$$

In the opposite limit, when $\Gamma_{sub} \gg \Gamma_{int}$, the TBC is limited by the internal scattering rate; in this limit, we get the internal TBC by replacing $\Gamma_{sub} \to \infty$.

$$G_{ext} = \int \hbar\omega D_{2D}(\omega)\frac{dN_0(T)}{dT}\Gamma_{int}d\omega. \tag{3.4}$$

The internal TBC due to phonon-electron scattering only can be calculated as

$$G_{ph-el} = \int \hbar\omega D_{2D}(\omega)\frac{dN_0(T)}{dT}\Gamma_{ph-el}d\omega, \tag{3.5}$$

where the Γ_{ph-el} is replaced by eqn. 3.13, 3.14 or 3.15 depending whether we want to calculate the internal resistance for in-plane acoustic phonon-, ZA phonon-, or optical phonon-electron scatterings.

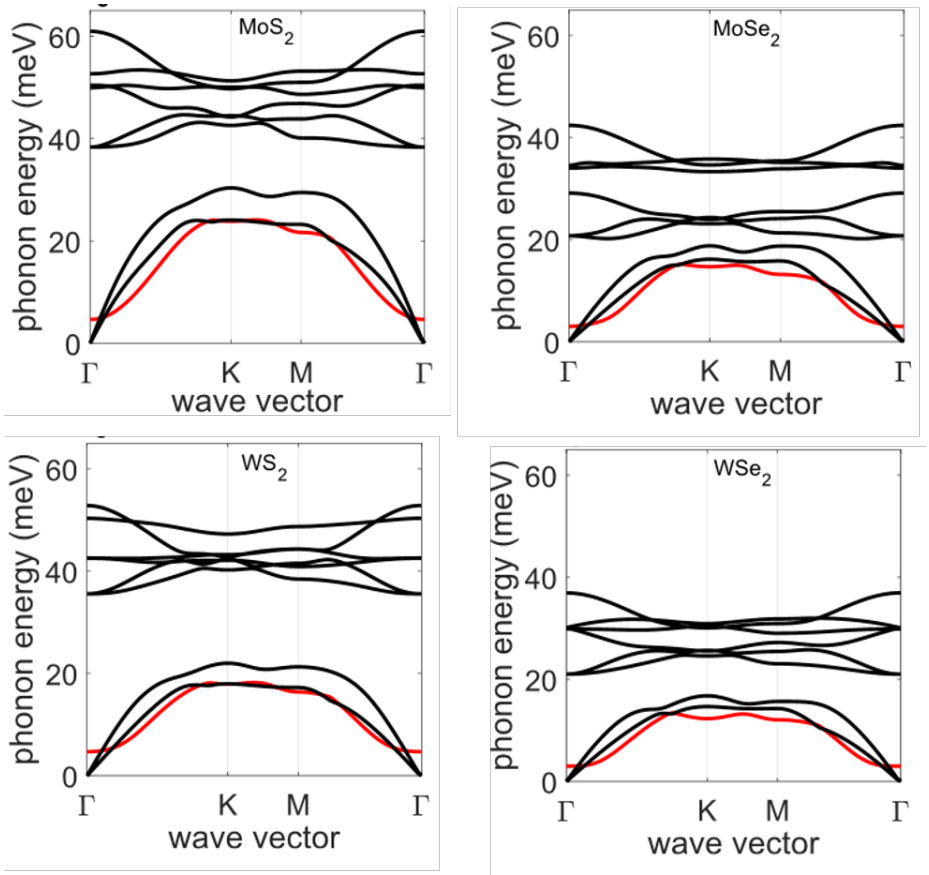

Figure 3.2: Phonon dispersions for various TMDs calculated from first principles Density Functional Theory.

3.1.1 Derivation of Phonon-electron rates

The derivation and expressions for phonon-electron scattering, for both acoustic and optical phonons, in 2D material is detailed here within deformation potential approximation. From Fermi's Golden rule, we can write the standard expression for the rate of transition of phonons as

$$\begin{aligned}\gamma_{q\nu} =&\frac{2\pi}{\hbar}\sum_{mn,k} \mid g^{\nu}_{mn}(k,q) \mid^2 [f_{nk}(1-f_{mk+q})\delta(E_{mk+q}-E_{nk}-\hbar\omega_{q\nu})- \\ & f_{nk}(1-f_{mk+q})(n_{q\nu}+1)\delta(E_{mk-q}-E_{nk}+\hbar\omega_{q\nu})].\end{aligned} \tag{3.6}$$

Under the relaxation time approximation (RTA) formalism, if the distribution function of only one phonon mode is perturbed from equilibrium by a small amount $n_{q\nu} = n^0_{q\nu} + \delta n_{q\nu}$, while assuming all the other electrons and phonons to be in equilibrium, the lifetime of this phonon mode $\tau^{ep}_{q\nu}$ is defined via $\gamma_{q\nu} = \frac{\delta n_{q\nu}}{\tau^{ep}_{q\nu}}$. This simplifies the transition rate of phonons

$$\frac{1}{\tau^{ep}_{q\nu}} = -\frac{2\pi}{\hbar}\sum_{mn,k} \mid g^{\nu}_{mn}(k,q) \mid^2 [(f_{nk}-f_{mk+q})\delta\left(E_{mk+q}-E_{nk}-\hbar\omega_{q\nu}\right), \tag{3.7}$$

where the matrix element can be written as (From Ziman's book on Electrons and Phonons) [99]

$$g^{\nu}_{mn}(k,q) = \sqrt{\frac{\hbar}{2m_0\omega_{q\nu}}}\left\langle mk+q|\partial_{q\nu}V|nK\right\rangle. \tag{3.8}$$

The matrix element $\left\langle mk+q|\partial_{q\nu}V|nK\right\rangle$ can either be calculated from first principles Density Functional Theory (DFT) calculations or can be approximated using appropriate deformation potential. Within Deformation Potential Approximation (DPA), the matrix element can be replaced by $D_a q$ for acoustic phonon mode and D_o for optical phonon mode (From Lundstrom's book on Fundamentals of carrier transport, 2009) [100]. The mass m_0 can be substituted by the product of mass density and area ρA. We use an effective mass approximation for expressing energies of the electron modes and the Einstein's model for phonon

vibrational frequencies—

$E_{nk} = \frac{\hbar^2 k_n^2}{2m^\star}$, $E_{mk+q} = \frac{\hbar^2}{2m^\star}(k_m + q) \cdot (k_m + q)$, $\omega_{q\nu} = v_s q$ (for acoustic branches), $\omega_{q\nu} = \omega_0$ (for optical branches), and also $\sum_{k',k} = \frac{A}{(2\pi)^2} \int_{k',k} d^2k$.

3.1.2 Phonon-electron rate for acoustic phonons

The transition rate for acoustic phonon can be written as

$$\frac{1}{\tau_{q\nu}^{ep}} = -\frac{D_a^2 q^2}{4\pi\rho\omega_{q\nu}} \sum_n \int_{k',k} d^2k (f_{nk} - f_{nk+q}) \delta \left(\frac{\hbar^2 k_n^2}{2m^\star} - \frac{\hbar^2}{2m^\star}(k_n + q) \cdot (k_n + q) - \hbar v_s q \right) \tag{3.9}$$

The Dirac-delta function in Eqn. 3.9 can be simplified further to obtain

$$\delta \left[-\frac{\hbar^2 q}{m^\star}(k_n cos\theta + \frac{q}{2} + \frac{m^\star v_s}{\hbar}) \right],$$

where $cos\theta$ is the angle between k_n and q. We use the properties of Dirac-delta function, $\delta(-x) = \delta(x)$ and $\delta(\alpha x) = \frac{\delta(x)}{|\alpha|}$ to write Eqn. 3.9 as

$$\frac{1}{\tau_{q\nu}^{ep}} = -\frac{m^\star D_a^2 q}{4\pi\hbar^2\rho\omega_{q\nu}} \sum_n \int_{k',k} d^2k (f_{nk} - f_{nk+q}) \delta \left[k_n cos\theta + \frac{q}{2} + \frac{m^\star v_s}{\hbar} \right]. \tag{3.10}$$

The integration is done along two cartesian axes k_{n1} and k_{n2}, which are chosen such that k_{n1} is pointing towards q, that is $k_n cos\theta = k_{n1}$. Substituting the Fermi-Dirac distribution in non-degenerate limit, we can write Eqn. 3.10 as

$$\frac{1}{\tau_{q\nu}^{ep}} = -\frac{m^\star D_a^2 q}{4\pi\hbar^2\rho\omega_{q\nu}} \sum_n \int_{k_{n1}} \int_{k_{n2}} \left[exp\left(-\frac{E_{nk} - E_F}{k_B T} \right) - exp\left(-\frac{E_{nk+q} - E_F}{k_B T} \right) \right] \delta[k_{n1} - k'_n],$$

where $k'_n = (-\frac{q}{2} - \frac{m^\star v_s}{\hbar})$. The detailed steps for the integration is given in the appendix, chapter 7.3.

$$\frac{1}{\tau_{q\nu}^{ep}} = \frac{m^{\star 3/2} D_a^2 (k_B T)^{1/2}}{(2\pi)^{1/2} 2\hbar^3 \rho v_s} \sum_n exp\left(\frac{E_F}{k_B T}\right) exp\left(-\frac{\hbar^2 q^2}{8m^\star k_B T} - \frac{m^\star v_s^2}{2k_B T} - \frac{\hbar v_s q}{2k_B T}\right)\left[exp\left(\frac{\hbar v_s q}{k_B T}\right) - 1\right]. \tag{3.11}$$

In the limit of small q, that is $q \to 0$, the transition rate for the acoustic phonons can be written as

$$\begin{aligned}\frac{1}{\tau_{q\nu}^{ep}} &= \frac{m^{\star 3/2} D_a^2 (k_B T)^{1/2}}{(2\pi)^{1/2} 2\hbar^3 \rho v_s} \sum_n exp\left(\frac{E_F}{k_B T}\right) exp\left(-\frac{m^\star v_s^2}{2k_B T}\right)\left(1 + \frac{\hbar v_s q}{k_B T} - 1\right) \\ &= \frac{m^{\star 3/2} D_a^2 q}{(2\pi)^{1/2} 2\hbar^2 \rho (k_B T)^{1/2}} \sum_n exp\left(\frac{E_F}{k_B T}\right) exp\left(-\frac{m^\star v_s^2}{2k_B T}\right).\end{aligned} \tag{3.12}$$

We can collect some of these terms and can express the acoustic phonon-electron scattering rate in terms of 2D carrier density. The electronic density of states for 2D material is given by

$$D_{2d}(E) = \frac{1}{4\pi^2} \frac{2\pi k}{\mid \nabla E \mid} = \frac{m^\star}{2\pi\hbar^2}.$$

And the 2D carrier density is given as

$$n_{2D}(E) = \int D_{2D}(E) f(E) dE = \frac{m^\star k_B T}{2\pi\hbar^2} exp\left(\frac{E_F - E_c}{k_B T}\right).$$

The transition rate for acoustic phonons in Eqn. 3.12 can thus be written as

$$\boxed{\frac{1}{\tau_{q\nu}^{ep}} = \frac{(2\pi m^\star)^{1/2} D_a^2 q}{2\rho (k_B T)^{3/2}} n(E) \sum_n exp\left(-\frac{m^\star v_s^2}{2k_B T}\right)}. \tag{3.13}$$

The derivation for the phonon-electron rates of ZA phonons is also similar, but the difference in the final expression comes from the quadratic dispersion of ZA phonons as opposed to the linear dispersion for in-plane acoustic phonons. The expression is

$$\boxed{\frac{1}{\tau_{q\nu}^{ep}} = \frac{(2\pi m^\star)^{1/2} D_{ZA}^2}{\rho q (k_B T)^{3/2}} n(E) \sum_n exp\left(-\frac{\hbar^2 \left(\frac{1}{2} + \frac{m^\star \omega_q}{\hbar q^2}\right)^2}{2m^\star q^2 k_B T}\right)}. \tag{3.14}$$

The efficiency of the heat transfer from electrons to the optical phonon modes depends on the strength of coupling between them. The derivation for the optical phonon-electron rate is detailed in the appendix, chapter 7.3.2. The final expression for the optical phonon-electron rate is

$$\boxed{\frac{1}{\tau_{q\nu}^{ep}} = \left(\frac{2\pi m^\star}{k_B T}\right)^{1/2} \frac{D_o^2}{\rho\omega_o} exp\left(-\frac{m^\star\omega_o^2}{2k_B T q^2}\right)\left(\frac{1}{\hbar q}\right) n(E) sinh\left(\frac{\hbar\omega_o}{2k_B T}\right)}. \tag{3.15}$$

It can be used to estimate how efficiently the electrons transfer their energy to the optical phonons. The TBC due to the optical phonon-electron rate can be calculated by replacing eqn. 3.15 in eqn. 3.5.

3.2 Results and Discussion

Figure 3.3 shows the TBC for various TMDs at different temperatures. The TBC in this figure is calculated for a carrier density equal to 10^{14} m^{-2}. The TBC values are much smaller than their corresponding external TBCs at all temperatures; at room temperature, TBC is smaller by a factor of about 3 to 4 for all the TMDs. This clearly indicates that the internal resistance due to anharmonic phonon-phonon scattering, also shown by the dotted lines in the figure, is the bottleneck to the cross-plane heat transfer from the 2D material to the substrate. In other words, the rate at which the ZA phonons carry thermal energy into the substrate, is much larger than the rate at which ZA phonons are replenished in the 2D material due to internal anharmonic phonon rates. At higher temperatures, due to the increase in the anharmonic phonon rates—as indicated in the figure by the increase in TBC due to phonon-phonon rates—the effective TBC (shown by the solid lines) improves, but still is much smaller than the external TBC. The overall TBC can be improved if we can tune the internal scattering rate such that there is either faster replenishment ZA phonons or by exploring additional channels to boost internal scattering rate.

Next, we examine the impact of phonon-electron scattering on the TBC of 2D materials. Figures 3.4(a)-(d) show the TBC of MoS_2, $MoSe_2$, WS_2, and WSe_2 vs. temperature

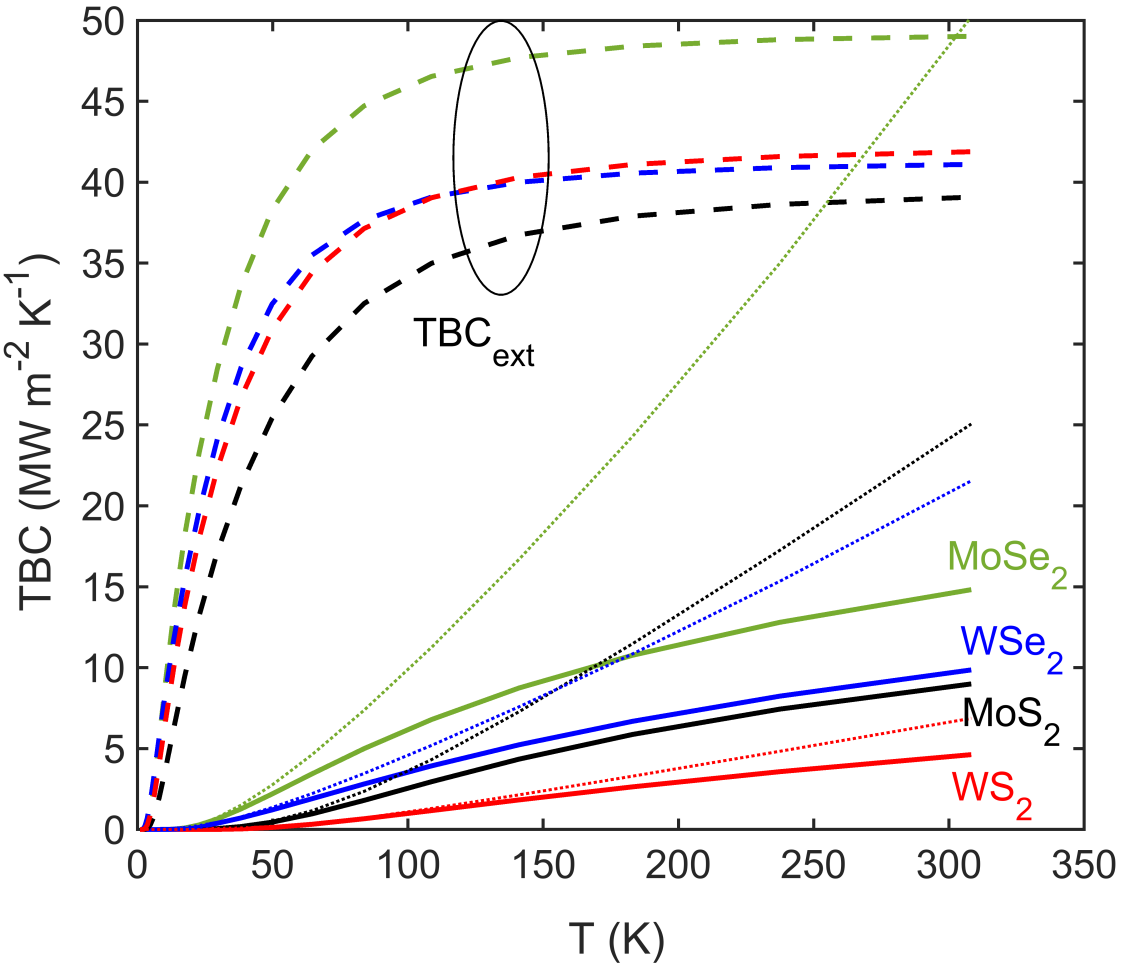

Figure 3.3: shows the external TBC (dashed lines) and the effective TBC (solid lines) vs. temperature (T) at negligible carrier densities (10^{14} m^{-2}) for various TMDs—MoS_2 (black), $MoSe_2$ (green), WS_2 (red) and WSe_2 (blue).

at different carrier densities. We can see that when the carrier density is increased from 10^{14} to 10^{18} m^{-2}, the TBC curves also shift upwards. We found that the TBCs of MoS_2 improves significantly by 36%, when the carrier density is varied from 10^{14} cm^{-2} to 10^{18} m^{-2} at 300 K. The enhancement is relatively smaller in $MoSe_2$ where the TBC increased by 15% for the same range of carrier densities. On the other hand, WS_2 and WSe_2 show a weaker dependence on phonon-electron coupling with an improvement of 13% and 5%, respectively, which is due to dominant phonon-phonon scattering in these materials. The maximum enhancement in TBC due to phonon-electron coupling is obtained for TMDs

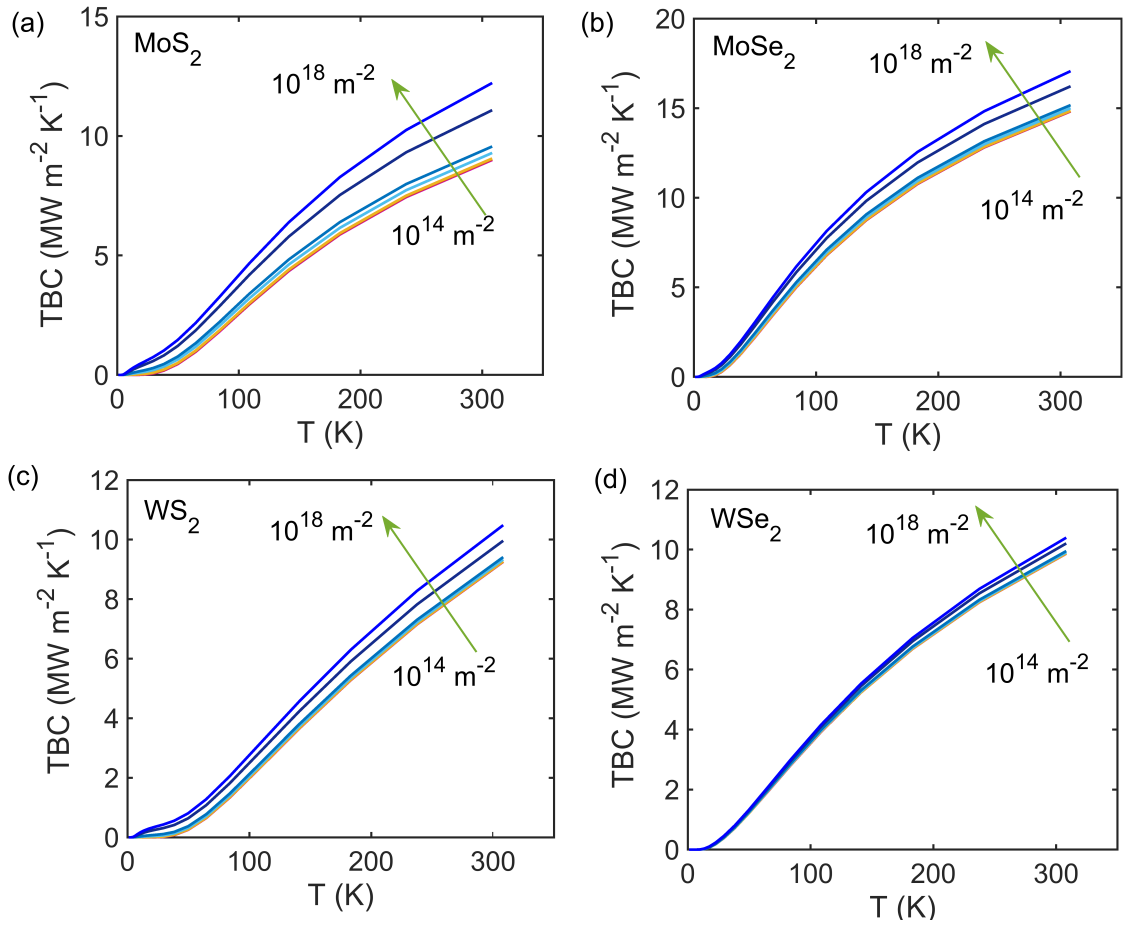

Figure 3.4: shows the TBC vs. temperature for various TMDs—MoS_2 (black), $MoSe_2$ (green), WS_2 (red) and WSe_2 (blue)—when the carrier density is tuned from 10^{14} to 10^{18} m^{-2}.

composed of lighter chalcogen atoms. Since ZA phonon-electron scattering acts as a parallel channel to repopulate ZA phonons in the 2D material, we compute the conductance due to phonon-electron scattering as $TBC_{ZAph-el} = \int \hbar\omega D_{2D}(\omega)\frac{dN_0}{dT}\Gamma_{ZAph-el}d\omega$. In Figure 3.5, we can see that the ZA phonon-electron scattering channel in MoS_2 exhibits the maximum conductance, which explains the largest enhancement in its TBC due to phonon-electron scattering. The contributions of TBC due to phonon-electron scattering to the overall TBC in WS_2 and WSe_2 is less than a 1 MW m^{-2} K^{-1}, whcih translates directly to weak enhancement of TBC due to doping in these materials.

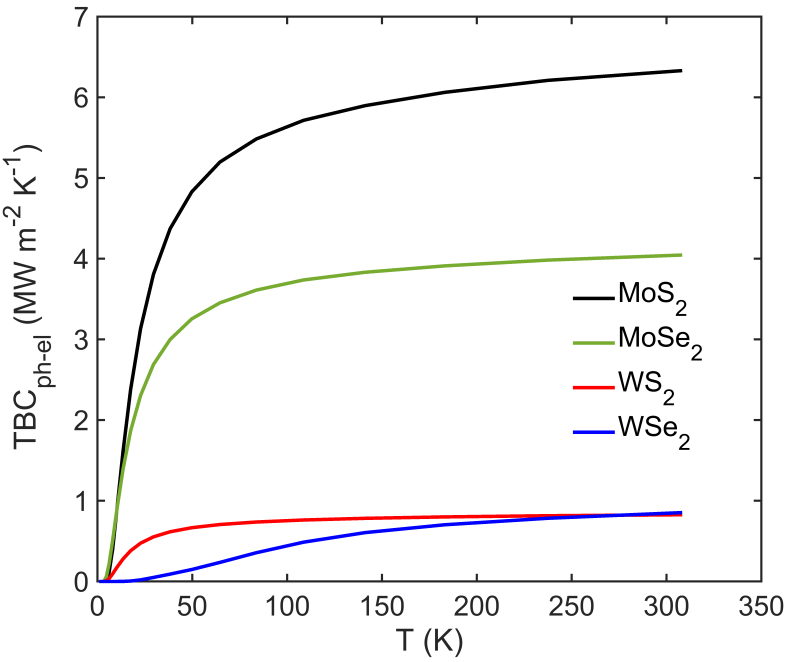

Figure 3.5: shows the TBC vs. temperature due to phonon-electron scattering for various TMDs—MoS_2 (black), $MoSe_2$ (green), WS_2 (red) and WSe_2 (blue)—at a carrier density equal to 10^{18} m^{-2}

3.3 Conclusions

To summarize, our results show that the TBC across a 2D-3D interface is limited by the internal scattering rate and ranges between 5 to 15 MW m^{-2} K^{-1}. However, if internal resistance is not the bottleneck, then the TBC between a 2D material and substrate can be much higher and will be given by the external TBC, which ranges from 40 to 50 MW m^{-2} K^{-1} for various TMDs. Our calculations reveal that the bottleneck due to internal resistance can be lowered by doping or gating the 2D material. MoS_2 exhibits the maximum enhancement in TBC of about 36% when the carrier density is increased from 10^{14} to 10^{18} m^{-2}. The enhancement of TBC in $MoSe_2$, WS_2, and WSe_2 due to doping are 15%, 13%, and 5%, respectively. Tuning TBC by varying carrier densities via doping/gating opens up a new avenue to manipulate heat flow in 2D materials.

CHAPTER 4

DYNAMICAL THERMAL CONDUCTIVITY AND PHONON HYDRODYNAMICS IN GRAPHENE RIBBONS

4.1 Introduction

In the context of developing of on-chip heat management, thermoelectric, and other energy conversion applications, the ability to tailor the thermal conductivity of a material is of fundamental importance. The steady-state behavior of the thermal transport in bulk semiconductors [101, 102], metals [103] and, more recently, in two-dimensional (2D) materials [104, 105, 106, 107, 108] has been widely studied, expanding the upper [109] and lower [110] bounds on thermal conductivity. Significant efforts have also been devoted to understand the reduction of thermal conductivity due to atomically rough interfaces [111, 112, 113] and boundaries [114, 115, 116] in nanostructured materials ranging from nanowires [117, 118, 119] to thin films [120, 121], superlattices [122, 123, 124, 125], and nanocomposites [126]. Heat conduction at short length scales, comparable to the phonon mean-free-path (MFP), and from small heat sources is a related type of size effect that has also drawn significant research attention in recent years [127, 128, 129]. When the temperature gradient varies over a length scale comparable to the phonon MFP, Fourier's concept of local thermal equilibrium breaks down [130, 131] and transport becomes nonlocal [132] and partially ballistic [133, 134].

To treat this situation, Mahan [135] proposed a nonlocal theory of heat conduction, while Chen [136] derived ballistic-diffusive heat equations to capture this nondiffusive nature of phonons. There have been numerous observations of the reduced thermal transport at length scales comparable to the phonon MFP [137, 138, 139, 140] and the interplay between phonon MFP spectra and size effects is now quite well understood [141, 142]. On the

other hand, the effect of fast transients and the frequency response of thermal conduction, sometimes called the *dynamical* thermal conductivity, has been given less attention. The response of thermal conductivity to rapidly varying heat sources may become more crucial in the future, especially with the constant growth in the clock frequencies in microprocessors and increase in giga- and terahertz applications of semiconductor devices. Analogous to transport at short scales in nanostructures, transport of heat at short time scale smaller than the phonon lifetime also becomes non-diffusive in nature, where local non-equilibrium prevails. It has been theoretically predicted in 3D materials that the heat flux in response to a time-varying temperature gradient starts decaying when the frequency of the applied heat source (Ω) exceeds a certain cut-off frequency Ω_c, which was related to the inverse of the average phonon relaxation time τ_C [143, 144, 145]. This dynamical and transient behavior has also been quantified in metals [146, 147, 148] and argon crystals [149].

Using molecular dynamics simulation, Volz[143] found that the phonon relaxation time in bulk semiconductors such as silicon is short, on the order of 30-140 ps, and concluded that a frequency-dependent behavior of thermal conductivity can only be observed when the applied temperature gradient is varying at frequencies exceeding 10 gigahertz (GHz). Sellitto et al. [150] used a phonon-hydrodynamical model with suitable boundary conditions to study the frequency dependent thermal conductivity in silicon nanowires, while Yang and Dames [151] extended the gray BTE model for periodic heating on the surface of bulk materials. Ezzahri and Joulain [145] solved the Boltzmann-Peierls transport equation in the frequency domain within single-mode relaxation time approximation and used the Debye-Callaway model [152] to obtain expressions for dynamical thermal conductivity of natural silicon and germanium crystals, and semiconductor alloys $Si_{0.7}Ge_{0.3}$, $In_{0.53}Ga_{0.47}As$, and $In_{0.49}Ga_{0.51}P$. Among these materials, $Si_{0.7}Ge_{0.3}$ alloys exhibited the most pronounced dynamical thermal conductivity trend with cut-off frequencies ranging from 0.1 megahertz (MHz) at 3 K to 2 GHz at the room temperature. Chaput [153] solved frequency-dependent phonon Boltzmann transport equation (pBTE) by linearizing it and transforming it into an

integral equation over the irreducible Brillouin zone to compute dynamical thermal conductivity in diamond, silicon, and magnesium silicide. The frequency-dependent behavior was observed only beyond 10 GHz, corroborating Volz [143].

In contrast to the aforementioned bulk semiconductors, 2D materials, especially graphene, have longer phonon relaxation times [154]. The presence of strong momentum-conserving normal phonon-phonon processes in graphene, overshadowing momentum-destroying umklapp processes, results in hydrodynamic transport [155, 156]. Therefore, in suspended graphene and wide graphene ribbons the cut-off frequency Ω_c is much lower than that of silicon, even at room temperature. This could impact thermal dynamics and transients [157] in graphene at comparatively lower frequency ranges. Therefore, the dynamical thermal conductivity is expected to play a significant role in removing heat from electronic devices based on graphene and other related two-dimensional materials switching at high frequencies. Some of the other interesting phenomena that can be studied using dynamical thermal conductivity are Poiseuille flow [158] and *second sound*, where heat does not diffuse but rather propagates in a wave-like fashion [159, 160, 161, 162]. This phenomenon, which has been observed at low temperatures in liquid helium [163], NaF [164, 165], Bi [166, 167], and $SrTiO_3$ [168], was predicted from first-principles calculations to persist even at room temperature in graphene [155].

4.2 Methodology

In this paper, we focus on the dynamical thermal conductivity of suspended graphene ribbons. We calculate a frequency-dependent thermal conductivity by solving the time-dependent phonon Boltzmann transport equation (pBTE). In response to a rapidly time-varying temperature field, the heat conduction in solids becomes non-local in time and space $\kappa(\vec{r}, t; \vec{r'}, t')$ [169]. Phonons that are driven by a temperature gradient at position $\vec{r'}$ and time t', move from $\vec{r'}$ to $\vec{r}$ in time between t' and t to cause a heat current at position $\vec{r}$ and time t. The heat current $J(\vec{r}, t)$ is given by the convolution of thermal conductivity

with the temperature gradient $\nabla_{\vec{r}}T$ at position $\vec{r'}$ and time t' as[141]

$$J(\vec{r},t) = -\int d\vec{r'}dt'\kappa(\vec{r},t;\vec{r'},t')\nabla_{\vec{r}}T(\vec{r'},t').$$

It is mathematically convenient to express the heat current in Fourier domain, where the convolution becomes a simple product of a frequency- and wavenumber-dependent thermal conductivity and temperature gradient. On taking the Fourier transform of the time-domain heat current, we get

$$\widetilde{J}(\vec{Q},\Omega) = -\widetilde{\kappa}(\vec{Q},\Omega) \times \widetilde{\nabla}T(\vec{Q},\Omega), \tag{4.1}$$

where $\widetilde{J}(\vec{Q},\Omega)$, $\widetilde{\kappa}(\vec{Q},\Omega)$ and $\widetilde{\nabla}T(\vec{Q},\Omega)$ are the Fourier-transformed heat current, thermal conductivity, and temperature gradient, respectively, while Q and Ω are the wavenumber and frequency of the temperature gradient. The time-dependent pBTE is given by

$$\frac{\partial N_{q,b}(\vec{r},t)}{\partial t} + \vec{v}_{q,b} \cdot \nabla_{\vec{r}} N_{q,b}(\vec{r},t) = \left[\frac{\partial N_{q,b}(\vec{r},t)}{\partial t}\right]_{coll}, \tag{4.2}$$

where $N_{q,b}(\vec{r},t)$ is the phonon distribution function, which is a function of position $\vec{r}$ as well as time t. From here on, we suppress $(\vec{r},t)$ in $T(\vec{r},t)$ and $N_{q,b}(\vec{r},t)$, and $(\vec{Q},\Omega)$ in $\widetilde{N}_{q,b}(\vec{Q},\Omega)$ for clarity, where $\widetilde{N}_{q,b}(\vec{Q},\Omega)$ is the Fourier-transformed distribution function. $\vec{v}_{q,b} = \partial\omega_{q,b}/\partial q$ is the group velocity of the phonon wavevector q in branch b, $\omega_{q,b}$ being its vibrational frequency. Using Callaway's idea [152], we write the collision term as the sum of two terms

$$\left[\frac{\partial N_{q,b}}{\partial t}\right]_{coll} = -\left(\frac{N_{q,b} - N^0_{q,b}}{\tau^R_{q,b}}\right) - \left(\frac{N_{q,b} - N^*_{q,b}}{\tau^N_{q,b}}\right), \tag{4.3}$$

where the first term on the right hand side of the equation represents the rate at which the non-equilibrium distribution returns to the equilibrium Bose-Einstein distribution $N^0_{q,b} = [\exp(\hbar\omega_{q,b}/k_BT)-1]^{-1}$ due to momentum-destroying resistive scattering mechanisms. The second term represents how the perturbed distribution function in the presence of collective momentum-conserving normal phonon-phonon processes relaxes to a drifted distribution

$N^*_{q,b}$, often referred to as *flowing equilibrium*. The flowing equilibrium distribution is written as $N^*_{q,b} = [\exp\Big(\hbar\omega_{q,b}/k_BT + \vec{\lambda}\cdot q\Big) - 1]^{-1}$, where $\vec{\lambda}$ is the displacement vector of the drifted distribution and is related to the drift velocity by $\vec{\lambda} = \hbar\vec{\nu}_d\,/k_BT$. The $\tau^R_{q,b}$ and $\tau^N_{q,b}$ are the average resistive and normal scattering times respectively.

Resistive processes include umklapp phonon-phonon processes, isotope, and line-edge roughness scattering so the resistive scattering rate is calculated by combining them as $1\,/\tau^R_{q,b} = 1\,/\tau^U_{q,b} + 1\,\Big/\tau^{Iso}_{\omega_q} + 1\,/\tau^{LER}_{q,b}$. While Callaway's approach of separating the collision integral into resistive and normal components is not as exact as the iterative [170, 171, 172] and direct pBTE solvers [173], it has been widely used and shown to be reasonably accurate in graphene [174] and graphite ribbons [175] when combined with *ab initio* dispersion. Here we compute the phonon dispersion of suspended graphene from first-principles Density Functional Theory (DFT) as implemented in the open-source package *Quantum Espresso* [97]. The expressions for all the relevant scattering rates, including anharmonic umklapp and normal phonon-phonon [176], isotope [177], and line-edge roughness [178], are taken from our recent work [108].

The deviation of the phonon distribution function from equilibrium is $\Phi_{q,b}(\vec{r},t) = N_{q,b} - N^0_{q,b}$. The derivation of this deviated distribution in frequency domain $\widetilde{\Phi}_{q,b}(Q,\Omega)$ is discussed in details later in the section. Once $\Phi_{q,b}(\vec{r},t)$ is obtained, the non-local heat current is related to $\widetilde{\Phi}_{q,b}(Q,\Omega)$ through

$$\widetilde{J}(Q,\Omega) = -\widetilde{\kappa}(Q,\Omega)\times\widetilde{\nabla}T(Q,\Omega) = \sum_{q,b}\hbar\omega_{q,b}v_{q,b}\widetilde{\Phi}_{q,b}(Q,\Omega) \tag{4.4}$$

from which we obtain an expression for the frequency-dependent thermal conductivity composed of two parts $\kappa_{eff}(Q,\Omega) = \kappa_{RTA}(Q,\Omega) + \kappa_{corr}(Q,\Omega)$. The $\kappa_{RTA}(Q,\Omega)$ is the resistive component thermal conductivity given by

$$\kappa_{RTA}(Q,\Omega) = \frac{1}{A\delta}\sum_{q,b}\hbar\omega_{q,b}v^2_{q,b}\frac{\tau^C_{q,b}}{1+j\Omega\tau^C_{q,b}+jQ\Lambda_{q,b}}\frac{\partial N^0_{q,b}}{\partial T} \tag{4.5}$$

where A and δ are the area of the unit cell and thickness of the graphene monolayer. This κ_{RTA} is the component of thermal conductivity originating from the relaxation time approximation (RTA), where all the scattering mechanisms including normal scattering are treated as resistive. Hence, we refer to κ_{RTA} as the resistive or RTA thermal conductivity. The frequency dependence and non-locality enter the κ_{RTA} through the term $1 + j\Omega\tau^C_{q,b} + jQ\Lambda_{q,b}$ in the denominator, which acts as a suppression function: when frequency exceeds the scattering rate $\Omega > 1/\tau^C_{q,b}$ of a phonon mode or the wavelength is smaller than its MFP $Q^{-1} < \Lambda_{q,b}$, the contribution of that mode to the conductivity is correspondingly reduced.

In graphene, momentum-conserving normal scattering mechanisms are strong and the RTA solution κ_{RTA} underestimates the total thermal conductivity [171]. Following Allen's improved Callaway (AIC) model [179], the hydrodynamic effect of normal processes is encapsulated as a correction term $\kappa_{corr} = \frac{\lambda_1\lambda_2}{\lambda_3}$, where

$$\lambda_1(Q,\Omega) = \frac{1}{A\delta}\sum_{q,b} v_{q,b}q_{\parallel}\frac{\tau^C_{q,b}}{1 + j\Omega\tau^C_{q,b} + jQ\Lambda_{q,b}}\frac{\partial\widetilde{N}^0_{q,b}}{\partial T} \tag{4.6}$$

$$\lambda_2(Q,\Omega) = \frac{1}{A\delta}\sum_{q,b} v_{q,b}q_{\parallel}\left[\frac{\tau^C_{q,b}/\tau^N_{q,b}}{1 + j\Omega\tau^C_{q,b} + jQ\Lambda_{q,b}}\right]\frac{\partial\widetilde{N}^0_{q,b}}{\partial T} \tag{4.7}$$

$$\lambda_3(Q,\Omega) = \frac{1}{A\delta}\sum_{q,b} \frac{q^2_{\parallel}}{\hbar\omega_{q,b}}\left[1 - \frac{\tau^C_{q,b}/\tau^N_{q,b}}{1 + j\Omega\tau^C_{q,b} + jQ\Lambda_{q,b}}\right]\frac{\partial\widetilde{N}^0_{q,b}}{\partial T} \tag{4.8}$$

The effective thermal conductivity κ_{eff} is a sum of the RTA, which treats all scattering mechanisms as resistive, and a correction that accounts for an additional collective contribution from momentum-conserving normal processes, both of which are complex-valued and depend on the frequency and spatial wavenumber of the temperature gradient. Similar to κ_{RTA}, each of the correction terms has an Ω- and Q-dependent suppression function. However, the dependence of κ_{corr} due to the combined three terms $\lambda_1\lambda_2/\lambda_3$ is more complex than κ_{RTA}.

4.2.1 Derivation of the deviated phonon distribution

To obtain an expression for $\widetilde{\Phi}_{q,b}(Q,\Omega)$, we first Fourier-transform the time-dependent pBTE (Eq. 4.2), akin to the work by Ezzahri and Joulain [145], and write the pBTE in Fourier domain as

$$\begin{aligned} &j\Omega\widetilde{\Phi}_{q,b} + j\Omega\widetilde{N}^0_{q,b} + j\vec{Q}\cdot\vec{v}_{q,b}\widetilde{\Phi}_{q,b} + \vec{v}_{q,b}\cdot\widetilde{\nabla}T(Q,\Omega)\frac{\partial\widetilde{N}^0_{q,b}}{\partial T} \\ &= -\frac{\widetilde{N}_{q,b}-\widetilde{N}^0_{q,b}}{\tau^R_{q,b}} - \frac{\widetilde{N}_{q,b}-\widetilde{N}^*_{q,b}}{\tau^N_{q,b}}, \end{aligned} \tag{4.9}$$

where the right-hand side is the collision term from Eq. (4.3). The flowing equilibrium $\widetilde{N}^*_{q,b}$ is expanded around $\vec{\lambda}=0$ in a Taylor series [145, 179], keeping terms up to first order in $\vec{\lambda}$

$$\widetilde{N}^*_{q,b} \approx \widetilde{N}^*_{q,b}(\vec{\lambda}=0) + \vec{\lambda}\cdot\left(\frac{\partial\widetilde{N}^*_{q,b}}{\partial\vec{\lambda}}\right)_{\vec{\lambda}=0} = \widetilde{N}^0_{q,b} - \frac{k_B T^2}{\hbar\omega_{q,b}}\frac{\partial\widetilde{N}^0_{q,b}}{\partial T}(\vec{\lambda}\cdot\vec{q}). \tag{4.10}$$

On replacing $\widetilde{N}^*_{q,b}$ on the right side of Eq. (4.9) with the expression in Eq. (4.10), and $\widetilde{N}_{q,b}-\widetilde{N}^0_{q,b}$ with $\widetilde{\Phi}_{q,b}$, we write Eq. (4.9) as

$$\begin{aligned} &j\Omega\widetilde{\Phi}_{q,b} + j\Omega\widetilde{N}^0_{q,b} + j\vec{Q}\cdot\vec{v}_{q,b}\widetilde{\Phi}_{q,b} + \vec{v}_{q,b}\cdot\widetilde{\nabla}T(Q,\Omega)\frac{\partial\widetilde{N}^0_{q,b}}{\partial T} \\ &= -\frac{\widetilde{\Phi}_{q,b}}{\tau^C_{q,b}} - \frac{1}{\tau^N_{q,b}}\left[\frac{k_B T^2}{\hbar\omega_{q,b}}\frac{\partial\widetilde{N}^0_{q,b}}{\partial T}\vec{\lambda}\cdot\vec{q}\right], \end{aligned} \tag{4.11}$$

where $1/\tau^R_{q,b} + 1/\tau^N_{q,b}$ is the combined quasi-particle relaxation rate $1/\tau^C_{q,b}$ [179]. By rearranging the terms, $\widetilde{\Phi}_{q,b}$ can be written as

$$\begin{aligned} \widetilde{\Phi}_{q,b}(Q,\Omega) = &-\frac{\tau^C_{q,b}}{1+j\Omega\tau^C_{q,b}+jQ\Lambda_{q,b}}\vec{v}_{q,b}\cdot\widetilde{\nabla}T(Q,\Omega)\frac{\partial\widetilde{N}^0_{q,b}}{\partial T} \\ &-\frac{\tau^C_{q,b}/\tau^N_{q,b}}{1+j\Omega\tau^C_{q,b}+jQ\Lambda_{q,b}}\frac{k_B T^2}{\hbar\omega_{q,b}}\frac{\partial\widetilde{N}^0_{q,b}}{\partial T}(\vec{\lambda}\cdot\vec{q}) - j\Omega\widetilde{N}^0_{q,b}\tau^C_{q,b}, \end{aligned} \tag{4.12}$$

where $\Lambda_{q,b} = v_{q,b}\tau^C_{q,b}$ is the modal phonon MFP and Q is the component of the wavevector of the temperature gradient $\vec{Q}$, both along the direction of transport.

To obtain an expression for the displacement of the drifted distribution $\vec{\lambda}$ we follow Allen's improved Callaway (AIC) model [179], according to which the total crystal momentum should be the same for both the actual distribution $\widetilde{N}_{q,b}$ and the flowing equilibrium $\widetilde{N}^*_{q,b}$. This means

$$\sum_{q,b} \vec{q}(\widetilde{N}_{q,b} - \widetilde{N}^*_{q,b}) = 0 = \sum_{q,b} \vec{q}(\widetilde{\Phi}_{q,b} + \widetilde{N}^0_{q,b} - \widetilde{N}^*_{q,b}). \tag{4.13}$$

Using the Taylor series expansion for $\widetilde{N}^*_{q,b}$ obtained in Eq. (4.10), we write $\widetilde{N}^0_{q,b} - \widetilde{N}^*_{q,b}$ on the right hand side of Eq. (4.13) as

$$\widetilde{N}^0_{q,b} - \widetilde{N}^*_{q,b} = \frac{k_B T^2}{\hbar \omega_{q,b}} \frac{\partial \widetilde{N}^0_{q,b}}{\partial T} \vec{\lambda} \cdot \vec{q}. \tag{4.14}$$

Taking $\vec{\lambda}$ to be in the direction of the applied temperature gradient, $\vec{\lambda} \cdot \vec{q}$ can be simplified to $\lambda q_{\parallel}$, where $q_{\parallel}$ is the phonon wavevector in the transport direction. Then, combining Eqs. (4.12) and (4.14), $\widetilde{\Phi}_{q,b}$ and $\widetilde{N}^0_{q,b} - \widetilde{N}^*_{q,b}$ can be replaced in Eq. (4.13) to solve for the displacement

$$\widetilde{\lambda}(Q,\Omega) = \frac{\displaystyle\sum_{q,b} q_{\parallel} \left(\frac{\tau^C_{q,b}}{1 + j\Omega\tau^C_{q,b} + jQ\Lambda_{q,b}} v_{q,b} \frac{\partial \widetilde{N}^0_{q,b}}{\partial T} \right) \widetilde{\nabla} T(Q,\Omega) + j\Omega \sum_{q,b} \vec{q} \widetilde{N}^0_{q,b} \tau^C_{q,b}}{\displaystyle\sum_{q,b} q^2_{\parallel} \frac{\partial \widetilde{N}^0_{q,b}}{\partial T} \frac{k_B T^2}{\hbar \omega_{q,b}} \left(1 - \frac{\tau^C_{q,b}/\tau^N_{q,b}}{1 + j\Omega\tau^C_{q,b} + jQ\Lambda_{q,b}} \right)}. \tag{4.15}$$

The term $\displaystyle\sum_{q,b} q \widetilde{N}^0_{q,b} \tau^C_{q,b}$ in the numerator of Eq. (4.15) is equal to zero because both the equilibrium distribution and the scattering rates are even functions while the wavevector $\vec{q}$ is odd; consequently, the displacement $\widetilde{\lambda}(Q,\Omega) \propto \widetilde{\nabla} T(Q,\Omega)$. We also find $\widetilde{\lambda}$ to be dependent on both wavenumber Q and frequency Ω, unlike earlier derivations that assumed it to be constant [145]. The deviation $\widetilde{\Phi}_{q,b}$ can now be expressed by substituting $\widetilde{\lambda}(Q,\Omega)$ in Eqn. 4.12. Now $\widetilde{\Phi}_{q,b}(Q,\Omega)$ is replaced in Eq. 4.4 to obtain thermal conductivity as a function of wavenumber and frequency.

4.3 Results and Discussions

4.3.1 Frequency Dependence

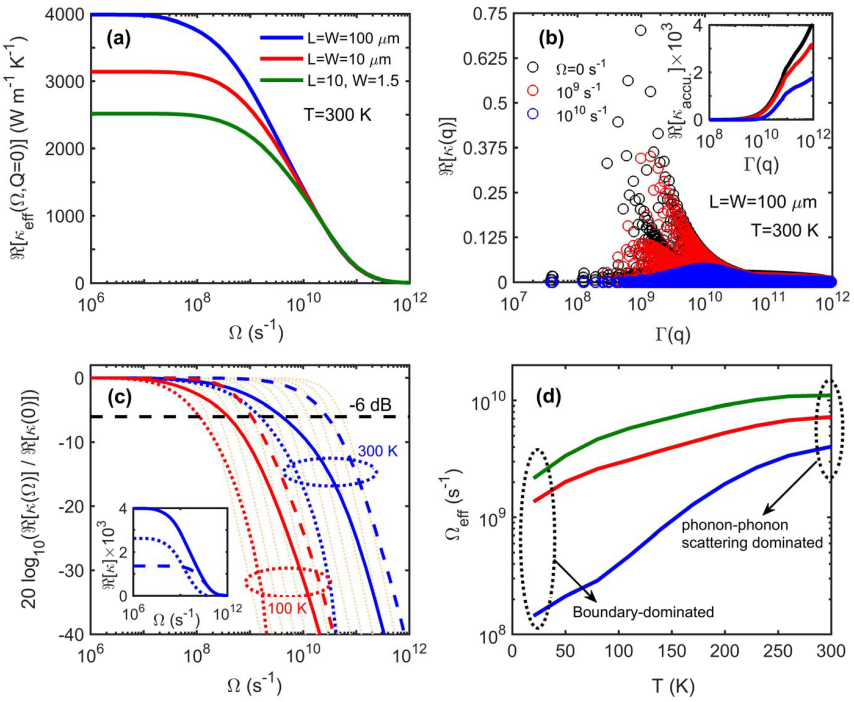

Figure 4.1: **(a)** shows the frequency dependence of the real part of thermal conductivity $\mathrm{Re}(\kappa_{eff})$ for several ribbon sizes at 300 K. In **(b)**, the mode-dependent thermal conductivity is plotted against the scattering rate of the corresponding phonon modes at different frequencies of temperature gradient, $\Omega = 0$, 10^9, and 10^{10} s^{-1} shown by black, red and blue markers respectively. The inset in **(b)** shows the accumulative thermal conductivity with modal scattering rates for the same set of frequencies as described by the markers previously. The normalized thermal conductivity $\kappa_{eff}(\Omega)/\kappa_{eff}(\Omega = 0)$ in dB vs. frequency of temperature gradient (Ω) is plotted in **(c)** for 100 and 300 K. The solid, dashed, and dotted lines represent normalized κ_{eff}, κ_{RTA}, and κ_{corr}, respectively. The inset shows the components of thermal conductivity at 300 K. In **(c)**, the size of the ribbon considered is 100 $\mu m \times 100$ μm. The cut-off frequency corresponding to κ_{eff} is plotted against temperature for various ribbon sizes in **(d)**. The rms value of edge roughness is taken to be 2 nm for all the cases.

First we focus on the effect of the dynamical temperature gradient on thermal conductivity. We separate the temporal dependence from the spatial dependence by setting $Q = 0$ in Eqns. 4.5-4.8. Figure 4.1a shows the real part of thermal conductivity vs. frequency of

the temperature gradient (Ω) for various ribbon sizes at room (300 K) temperature. For any given ribbon size, thermal conductivity shows two distinct behaviors: the first is a constant thermal conductivity regime at low frequencies of the temperature gradient, where the thermal conductivity is equal to its steady-state value $\kappa_{eff}(\Omega = 0)$ and the second is a high frequency regime, where thermal conductivity exhibits a decaying frequency-dependent behavior with Ω. The high-frequency regime resembles the response of a typical low-pass filter. The zero-frequency (steady-state) thermal conductivity is highest for the flake of dimensions $100\ \mu m \times 100\ \mu m$ (largest size considered here) and lowest for the narrowest ribbon, whose width equals $1.5\ \mu m$, due to the strong edge-roughness scattering in the narrow ribbon.

The low-pass frequency-dependent behavior can be explained as follows: thermal conductivity is a sum of a broad distribution of modal thermal conductivities. At low frequencies, all the thermally-excited phonon modes have sufficient time to undergo multiple scattering events during one cycle of the temperature gradient. As a result, a local thermal equilibrium is restored to yield a steady-state thermal conductivity. In contrast, when the frequency is increased beyond the cut-off, phonons with relaxation times larger than one period of the temperature gradient do not have sufficient time to scatter and equilibrate. Such phonon modes do not fully contribute to conductivity; instead, their contribution is suppressed by an amount determined by the term $(1 + j\Omega\tau^C_{q,b})^{-1}$, leading to an apparent reduction in thermal conductivity at high frequencies. Thus, the frequency of temperature oscillations Ω can be used to control which phonon modes contribute towards thermal conductivity, and to what extent, based on their lifetimes. Frequency-dependent measurements can potentially be used to probe the distribution of phonon lifetimes, analogously to recent advances in MFP spectroscopy [180, 181, 182].

The frequency-dependent dynamical suppression is depicted in Figure 4.1b, where the mode-dependent thermal conductivity is plotted against their scattering rates for frequencies Ω equal to 0, 10^9, and $10^{10}\ s^{-1}$, shown by black, red, and blue markers respectively.

For Ω equal to $10^9\ s^{-1}$, it can be seen that the phonon modes with scattering rates smaller than Ω do not thermalize and thus contribute less towards thermal conductivity than in steady-state. The contribution of phonon modes with small scattering rates to thermal conductivity is further suppressed when Ω equals $10^{10}\ s^{-1}$, while modal thermal conductivities for phonon modes with scattering rates much larger than the frequency of the temperature gradient remain unaffected. The reduced contribution from the phonon modes with scattering rates smaller than Ω is also demonstrated in the cumulative thermal conductivity vs. scattering rate plot shown in the inset of Figure 4.1b.

The frequency-dependent thermal conductivity exhibits a low-pass thermal filter behavior, analogous to the frequency response of electrical conductivity for time-varying electric fields, as described by Drude's model. We normalize the frequency-dependent thermal conductivity for a given ribbon size and temperature by dividing with its corresponding steady-state value and then express it in decibels (dB), as one would describe the gain of an electronic filter, $20\log_{10}\left[\kappa_{eff}(\Omega)/\kappa_{eff}(0)\right]$. The solid lines in Figure 4.1c show the frequency response of the normalized thermal conductivity in dB at 100 and 300 K temperatures. If all the phonon modes scattered at the same rate, then the two thermal conductivity regimes, constant and frequency-dependent, would be separated by a single corner frequency $\Omega_{corner} = \tau^{-1}$ such that $\kappa(\Omega) = \kappa(0)/(1+j\Omega\tau)$. Multiplying both sides of this expression by ∇T and taking the inverse Fourier transform produces the Cattaneo-Vernotte (C-V) equation for the heat current $\tau\frac{dJ(x,t)}{dt} + J(x,t) = \kappa(0)\nabla T(x,t)$, which describes wave-like heat transfer with a finite velocity of propagation [183], x is considered as the direction of transport here. For comparison, the single-τ frequency response is plotted by yellow-dotted lines for different corner frequencies ranging from about 10^8 to 10^{12} Hz.

In contrast, in most solids including graphene, each phonon mode scatters at a vastly different rate. Owing to this broad spectrum of scattering rates, the transition of κ_{eff} from constant at low frequencies to decaying at high frequencies is broad and smooth. In Fig-

ure 4.1c, the thermal conductivity at both temperatures shows a much gradual decay than the yellow-dotted lines. As there is no single corner frequency to demarcate the transition between the constant thermal conductivity regime at low frequencies and decaying thermal conductivity at high frequencies, we define a cut-off frequency Ω_{eff} where the real part of the thermal conductivity decays to -6 dB or half of its steady-state value, shown by the black-dashed horizontal line in Figure 4.1c. The inset in Figure 4.1c shows the frequency response of the RTA (κ_{RTA}), correction (κ_{corr}), and effective (κ_{eff}) thermal conductivity at room temperature (RT, 300 K) by the dashed, dotted, and solid lines respectively for a graphene ribbon of size $100\ \mu m \times 100\ \mu m$. κ_{eff} is much greater than κ_{RTA} indicating hydrodynamic transport, where it is no longer sufficient to describe thermal conductivity with the RTA term alone. We normalize the resistive, normal, and effective thermal conductivities by their steady-state values in Figure 4.1c and observe different cut-off frequencies for each of the κ_{RTA}, κ_{corr}, and κ_{eff}. In suspended graphene ribbons, where a major fraction of the scattering events are momentum-conserving normal scattering, the heat flux is dissipated at a much slower rate than the purely resistive case and the relaxation time is larger than the one obtained under the RTA, leading to $\Omega_{RTA} > \Omega_{eff} > \Omega_{corr}$.

As Ω_{eff} is closely associated with the scattering rates, it can be tuned by both temperature and size of the ribbon. In Figure 4.1d, the cut-off frequencies for various ribbon sizes have been plotted against temperature. For a given ribbon size, owing to the increase in phonon-phonon scattering with temperature Ω_{eff} shows an increasing trend. At a given temperature, Ω_{eff} decreases with increasing ribbon size, which we attribute to the decrease in the boundary scattering with increasing ribbon size. At temperatures around 300 K, the size dependence of Ω_{eff} becomes weak because phonon-phonon scattering dominates over the boundary scattering. The cut-off frequencies in graphene ribbons are found to range from 100 MHz to 2 GHz at 20 K, and 3-10 GHz at room temperature, depending on ribbon width. We contrast these frequencies to the analogous behavior of high-frequency electrical conductivity of graphene, which was found to follow a Drude model [29] with a decay

at frequencies exceeding 4-6 THz, depending on substrate and carrier concentration [184]. Hence, there is a wide swath of frequencies between $\sim$3 GHz and $\sim$4 THz where thermal conductivity is strongly suppressed while electrical conductivity is at its DC value, offering a potential avenue for dynamic enhancement of the thermoelectric figure-of-merit $ZT(\Omega) \propto \sigma(\Omega)/\kappa(\Omega)$ [185].

The dynamical thermal conductivity can be split into real and imaginary parts, where $\mathrm{Re}(\kappa_{eff})$ is related to heat flux dissipation via scattering while the imaginary part of the thermal conductivity is related to the storage of thermal energy in the ballistic phonon modes. The imaginary component turns the heat diffusion equation (HDE) $\rho C_V dT/dt = \kappa d^2T/dx^2$ into a dampened wave equation; in fact, a purely imaginary conductivity turns the HDE into a wave equation, analogous to the Schrödinger equation, admitting solutions of the form $T(x,t) \propto \exp[j(Qx - \Omega t)]$ that satisfy $j\Omega\rho C_V T = -\kappa(\Omega, Q)Q^2T$ (ρ and C are density and specific heat capacity). Furthermore, the relative sizes of the real and imaginary components dictate the phase of the heat flux relative to the temperature gradient that drives it, with the imaginary component representing phase lag. This lagging behavior can be traced back to the C-V equation, which is to first order equivalent to $J(x, t+\tau) = -\kappa(0)\nabla T(x,t)$ [186], with τ being the flux-gradient phase lag. The frequency response of the imaginary part of thermal conductivity $\mathrm{Im}(\kappa_{eff})$, shown by the solid curves in Figure 4.2a for $100\ \mu m \times 100\ \mu m$ at different temperatures. $\mathrm{Im}(\kappa_{eff})$ shows an increasing trend beyond the frequency where the real part of thermal conductivity starts to fall off. Then $\mathrm{Im}(\kappa_{eff})$ peaks before decaying to zero at high frequencies. The height of the peak depends on temperature in the same way as the steady-state thermal conductivity.

The dashed and solid lines in Figure 4.2a represent the imaginary parts of the RTA component $\mathrm{Im}(\kappa_{RTA})$ and total thermal conductivity $\mathrm{Im}(\kappa_{eff})$; the imaginary part of correction κ_{corr} is omitted for clarity. At both 100 and 300 K, $\mathrm{Im}(\kappa_{RTA})$ peaks at a higher frequency than the corresponding $\mathrm{Im}(\kappa_{eff})$ due to the presence of strong normal scattering, associated with hydrodynamic thermal transport, indicating that the RTA component

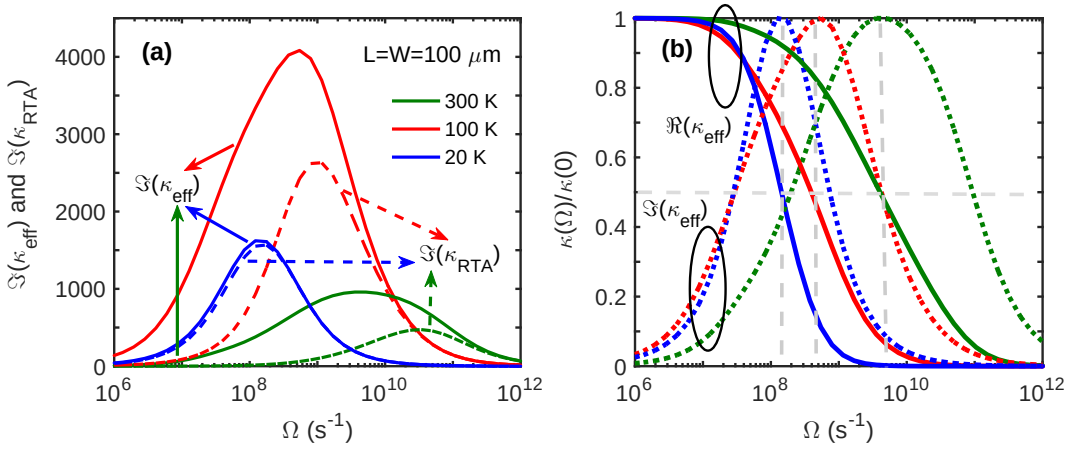

Figure 4.2: **(a)** Imaginary part of thermal conductivity vs. frequency of the temperature gradient for $L = W = 100\ \mu m$ at 20, 100, and 300 K. The frequency response of the $\mathrm{Im}(\kappa_{RTA})$ is shown by the dashed lines for different temperatures. **(b)** shows the normalized real as well as the imaginary part of thermal conductivity for the same set of temperatures and ribbon size. The solid lines represent the normalized $\mathrm{Re}(\kappa_{eff})$ and the dotted-lines their imaginary counterparts $\mathrm{Im}(\kappa_{eff})$.

has a smaller phase delay. There is a window of frequencies between the two peaks where κ_{corr} is complex, thus lagging in phase, while κ_{RTA} is real and in-phase with the gradient. In Figure 4.2b, we observe that the imaginary part of thermal conductivity peaks at the same frequency Ω_{eff} where the real part of thermal conductivity decays to half of its steady-state value. Thus, the peak of the imaginary part can also be used to determine the cut-off frequency, at which the phase angle between flux and gradient is 45° for a first-order and 90° for a second-order frequency slope. In the frequency range between Ω_{eff} and Ω_{RTA}, the κ_{corr} will be complex while κ_{RTA} is still real-valued, indicating a phase difference between these two components of the heat flux.

4.3.2 Spatial Dependence

Now we turn to the spatial dependence of thermal conductivity. To isolate it from the temporal response of thermal conductivity, we set Ω=0 in Eqs. (4.5-4.8). The real part of thermal conductivity is plotted in Figure 4.3 against the wavelength (Q^{-1}) of the tempera-

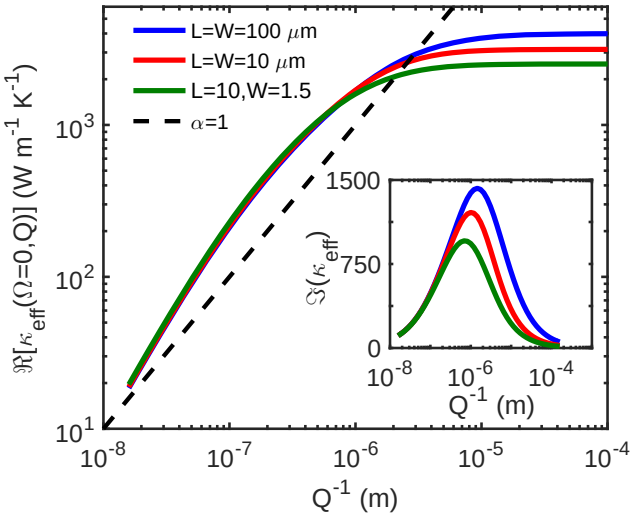

Figure 4.3: Real part of the thermal conductivity vs. wavelength of temperature gradient (Q^{-1}) for several ribbon sizes at 300 K, showing super-linear scaling in the narrow ($Kn < 1$) regime. Dashed line indicates a linear ($\propto Q^{-\alpha}$ with $\alpha = 1$) trend for comparison. The inset shows the corresponding wavelength dependence of the imaginary part of thermal conductivity.

ture gradient for ribbon dimensions ranging from 1.5 to 100 μm at 300 K. The wavelength of temperature gradient Q^{-1} is the relevant lengths scale; when it is larger than the phonon MFP (Λ), all the phonons undergo multiple scattering events within a single temperature node, leading to thermalization. On the other hand, when the wavelength is comparable to the phonon MFP, a fraction of the phonons having $\Lambda > Q^{-1}$ travel ballistically and do not scatter on the length scale over which the temperature is varying. The modal dependence is captured by the suppression $1/(1 + jQ\Lambda_{q,b})$ in Eqs. (4.5-4.8), where the dimensionless term $Kn = Q\Lambda_{q,b}$ plays the role of an effective modal Knudsen number. This also leads to an apparent reduction of thermal conductivity for $Kn > 1$, as observed previously in thermal grating experiments [140], and in narrow ribbons of width $W < \Lambda_{avg}$; Λ_{avg} being the phonon MFP averaged over all phonon modes and across all branches. When the ribbon edges are rough, heat flux decays at the edges due to diffuse scattering and components of the flux having whose wavelength exceeds the width, or $QW < 1$, are suppressed so the

wavelength dependence informs us about size scaling. Figure 4.3 shows that in narrow ribbons, thermal conductivity scales as $\kappa \propto Q^{-\alpha}$ with a slope $\alpha > 1$, indicating super-linear scaling. In contrast to the ballistic-to-diffusive transition [187] where size scaling is sub-linear, the hydrodynamic correction κ_{corr} has a stronger size dependence as all three terms Eqs. (4.6-4.8) explicitly depend on Q. The imaginary component of thermal conductivity is shown in the inset, displaying a peak around the same wavelength where the real part reduces to one-half of its $Q = 0$ value. At the peak, $Kn = 1$ and the wavelength equals the average phonon MFP $Q^{-1} = \Lambda_{avg} \approx 1$ μm [177].

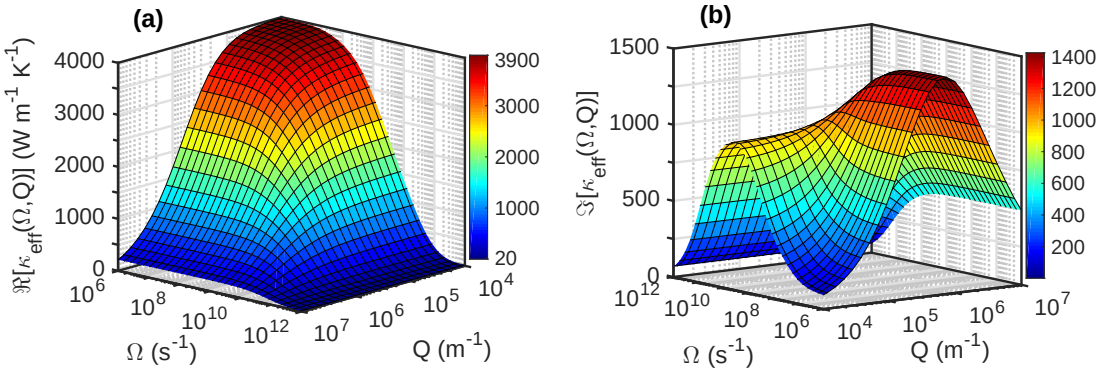

Figure 4.4: Surface plots of the frequency and spatial dependence of real part in **(a)** and imaginary part in **(b)** of thermal conductivity in a graphene ribbon of size L=W=100 μm and at 300 K.

The complete temporal and spatial dependence of the thermal conductivity at RT are shown in Figures 4.4a and 4.4b, respectively. At small wavenumbers (Q) and frequencies (Ω) of temperature gradient, the real part of thermal conductivity goes to its highest value $\mathrm{Re}[\kappa_{eff}(\Omega = 0, Q = 0)]$ for a given temperature and ribbon size. The $\mathrm{Re}[\kappa_{eff}(\Omega, Q)]$ decays to zero when either Ω exceeds the average scattering rate or the wavelength $Q^{-1} \ll \Lambda_{avg}$, the average phonon MFP. For any intermediate values, $\mathrm{Re}[\kappa_{eff}(\Omega, Q)]$ decays from $\mathrm{Re}[\kappa_{eff}(0, 0)]$ to zero with increasing Q and Ω. The imaginary part of thermal conductivity against frequency and wavenumber of the temperature gradient is plotted in Figure 4.3b.

For small wavenumbers, $Q^{-1} \ll \Lambda$, $\mathrm{Im}[\kappa_{eff}(\Omega, Q)]$ shows a resonant behavior: it is equal to zero at low as well as high frequencies with a peak at the cut-off frequency (also shown in Figure 4.2). $\mathrm{Im}[\kappa_{eff}(\Omega, Q)]$ vs. Q shows a similar trend for small frequencies below the scattering rate, also shown in the inset of Figure 4.5. However, for intermediate values of Ω and Q, the imaginary part of thermal conductivity exhibits a very interesting behavior: for $Q \gg 10^5 m^{-1}$, it is constant and decays to zero at high frequencies of temperature gradient. On the other hand, for Ω close to the cut-off, $\mathrm{Im}[\kappa_{eff}]$ starts constant, then reaches a broad peak where $Q^{-1} = \Lambda_{avg}$ (Kn =1) before decaying to zero at very high wavenumbers $Q \gg 10^7 m^{-1}$, implying larger phase shift for spatially localized or peaked heat pulses whose wavelength is around the phonon MFP $\approx$1 μm.

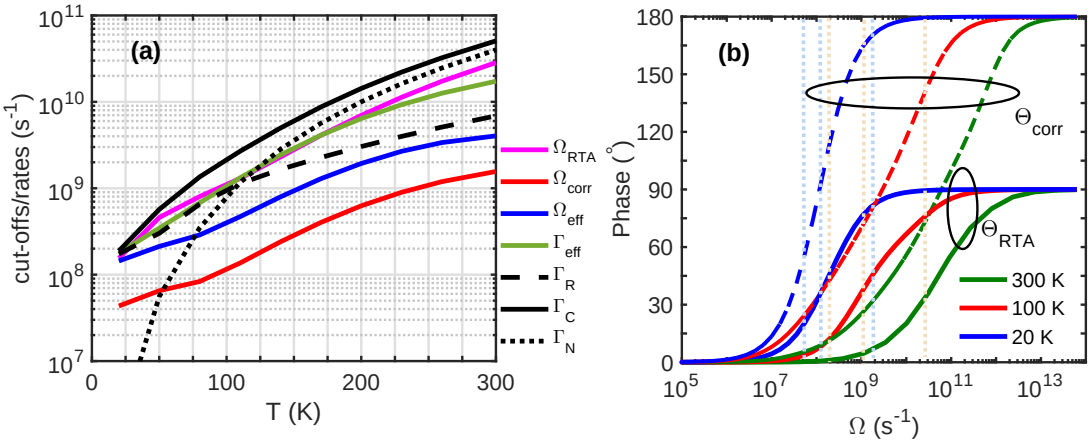

Figure 4.5: **(a)** shows the combined, normal, and resistive scattering rates along with the cut-off frequencies for a ribbon size of $L = W = 100\ \mu m$ as a function of temperature ranging from 20 to 300 K. **(b)** variation in phase of κ_{RTA} (solid) and κ_{corr} (dashed lines) vs. frequency at T=20 (blue), 200 (red), and 300 K (green), showing first and second-order behavior, respectively, along with a constant lag in the second sound frequency window $\Gamma_R < \Omega < \Gamma_N$, marked by vertical dashed lines in colors matching the corresponding temperatures.

4.3.3 Conductivity in the Second Sound Regime

The propagation of a heat pulse in the form of a temperature wave is referred to as second sound. For a material to host such a wave-like thermal transport, the primary condition

is that it should exhibit hydrodynamic transport,which occurs when there is significantly more momentum-conserving normal scattering than momentum-destroying resistive scattering mechanisms. Then there exists a "window" of frequencies $\Gamma_R < \Omega < \Gamma_N$ [160] where second sound can be observed. This makes suspended graphene a promising candidate to host second sound even at room temperature [155]. Second sound has also been characterized by a two-fluid flow where superfluid (in this case hydrodynamic, represented by κ_{corr}) and non-superfuid (here resistive, κ_{RTA}) components are out of phase [188]. This is in contrast to purely ballistic transport where all the components of the heat flux are in phase. We compare the cut-off frequencies to the scattering rates, which are all plotted in Figure 4.5a as a function of temperature for a large ($L = W$ =100 μm) graphene flake. Ω_{RTA} corresponds to the cut-off frequency of κ_{RTA} from to the combined scattering rate $\Gamma_C = \Gamma_R + \Gamma_N$, while Ω_{corr} and Ω_{eff} represent cut-off frequencies corresponding to κ_{corr} and κ_{eff}, respectively. The frequency window $\Gamma_R < \Omega < \Gamma_N$ coincides with the regime where the dissipative and hydrodynamic components of thermal conductivity, κ_{RTA} and κ_{corr}, are out of phase by a constant shift, shown in Figure 4.5b. Ultimately, we find that the hydrodynamic transport should be treated as two fluxes, each with its own lag arising out of the corresponding cut-off frequencies Ω_{RTA} and Ω_{corr}.

4.4 Conclusions

We have studied the dynamical response of thermal conductivity to time- and spatially-varying temperature gradients at several temperatures and ribbon sizes. We derived a compact and computationally efficient model for dynamical thermal conductivity by Fourier-transforming the pBTE, while including first-principles phonon dispersion and differentiating between resistive and normal scattering mechanisms. We found that the frequency-dependent thermal conductivity in suspended graphene resembles a low-pass thermal filter, whose cut-off frequency is related to the scattering rate and can be tuned over a wide range from a few MHz to several GHz by size and temperature. At low temperatures when the

phonon-phonon scattering is weak, the cut-off frequency rises inversely to ribbon width. The RTA contribution always has a higher cut-off, related to the total scattering rate, than the hydrodynamic correction. Both are complex-valued in the transition region, indicating a phase lag. The dynamical response of thermal conductivity can be used as a platform for phonon lifetime spectroscopy in frequency-dependent measurements. The dual cut-offs and phase lags of the two components of heat flux can be employed to study the hydrodynamic phenomenon of second sound.

CHAPTER 5

EFFECT OF MISORIENTATION ANGLE ON INTERFACES FORMED BY TWO-DIMENSIONAL MATERIALS

5.1 Introduction

Graphene, a monolayer of sp^2 hybridized carbon atoms arranged in a honeycomb lattice structure, has a unique Dirac cone electronic structure and exhibits numerous interesting properties including quasi-ballistic electron transport up to several microns of length even at room temperature. Besides graphene, transition metal dichalcogenides (TMDs) are another class of 2D materials which have attracted intense research interests in recent years. The potential applications of graphene and TMDs have motivated mass scale production of large-area films. Among the most popular methods, chemical-vapor deposition (CVD) on transition metal substrates is relatively cheap and extensively used to grow high quality large 2D sheets [189]. However, CVD-grown films are typically found to be polycrystalline in nature, consisting of many single crystalline grains each with random crystal orientation and separated by grain boundaries (GBs) [6]. Several studies have reported that grain boundaries in 2D materials impact both their electronic [189, 4, 5, 190, 191, 192] and thermal properties [193, 116, 194].

The earliest of these studies focused on the electrical resistance across graphene GBs. Experimentally, graphene GB resistance has been found to vary over a broad range from a few $\Omega\ \mu\mathrm{m}$ [7] to tens of $\mathrm{k}\Omega\ \mu\mathrm{m}$ [4, 5]. Huang et al. [8] showed a wide distribution of misorientation angles between adjacent grains in a polycrystalline monolayer graphene sheet with a preferential low angle growth of about 7°. The GB resistance across such GBs was found to be about 240 $\Omega\ \mu\mathrm{m}$. Contrasting this to the sheet resistance of 700 $\Omega/\square$

for the entire device, they concluded that the GB resistance is about one-third of the total resistance of a 250 nm grain. Koepke et al. [195] observed a reduction in mobility in CVD-grown graphene and attributed it to the strong carrier scattering at grain boundaries. Clark et al. [2] found resistance across graphene GBs to be varying between 40-140 $\Omega\ \mu\mathrm{m}$ for samples with misorientation angles ranging from 9° to 21°. The resistivity of GBs was more than 3 times the bulk resistivity of the grains consistently across all of their samples. There was a positive correlation between misorientation angles and GB resistance, but the width of the transition region surrounding the GB also played a role.

Besides experimental measurements, there are several theoretical studies [196, 197, 198, 199, 200] which have helped to gain more insight on transport across graphene GBs. Yazyev and Louie [196] found that GBs across grains represented by the same translational vectors are highly transparent to charge carriers with a transmission of about 80%, whereas GBs formed by grains with different translational vectors behave as perfect reflectors of carriers. Vancso et al. [197] performed wave packet dynamical transport calculations to show that transmission properties across graphene GBs depend on misorientation angles as well as localized structures at the boundaries. Zhang et al. [198] showed that intrinsic (defect-free) GBs are almost transparent to carrier transport in highly symmetric GB. They concluded that the degradation in transmission mainly comes from the extrinsic defects at the boundaries which results in the passivation of the π-orbital. Recently, Sun et al. [199] investigated electrical properties along different transport directions with respect to the GB direction using Density Functional Theory (DFT) calculations combined with Green's function technique. They showed that the zero band gap nature of graphene bandstructure remains intact even in the presence of GBs. They also found that there is an at least 50% current suppression in the transport across GBs as compared to the current in prinstine graphene. Despite the numerous studies on various types of graphene GBs, the dependence of GB resistance on misorientation angles is still inconclusive.

There has also been a growing interest in electrical transport of CVD-grown MoS_2 [201, 202, 203, 204, 205, 206]; however, little is known about the impact of misorientation angles on its GB resistance. Najmaei et al. [201] studied the individual and collective effect of GBs on electronic transport properties and found that the carrier mobility shows a weak dependence on channel length up to 75 μm. Kang [206] et al. also reported a similar dependence of field-effect mobility on channel length, again indicating that GBs don't significantly degrade the electronic transport properties in CVD-grown MoS_2. This observation was further corroborated by Schmidt et al. [202], where they demonstrate that the electronic properties of CVD-grown monolayer MoS_2 are comparable to those of their exfoliated counterparts. In contrast, Ly et al. [205] showed that MoS_2 sheets exhibit very poor electrical transport properties (mobilities below 70 $\mathrm{cm^2V^{-1}s^{-1}}$) for all their devices with different misorientation angles. They observed a positive but non-linear correlation between field-effect mobility and misorientation angles.

Electronic transport in lateral [84, 207, 208, 209] as well as vertical [210, 211, 212] 2D heterostructures has recently gained significant research attention with particular focus on graphene-contacted MoS_2 lateral (in-plane) heterostructures [213, 214, 215, 216]. Graphene has been reported to form an ohmic contact with MoS_2 [84, 217], resulting in an increase in mobility up to an order of magnitude as compared to that of in metal-MoS_2 field-effect transistors (FETs). This calls for investigating the role of misorientation angles in determining the graphene-MoS_2 interface resistance in such heterostructures. Throughout the numerous studies of the resistance of GBs and interfaces, a common thread is that the resistance spans a wide range of values depending on mismatch angle. A definitive trend explaining this variation, especially in MoS_2 GBs and graphene-MoS_2 interfaces, still requires further investigation.

In this paper, we focus on the fundamentals behind the impact of grain misorientation angles in 2D homojunctions and heterojunctions. Starting from electronic structure obtained through first principles Density Functional Theory (DFT), we calculate the transmis-

sion coefficients and boundary/interface resistances for graphene and MoS_2 grain boundaries, as well as graphene-MoS_2 heterojunctions. We use the transmission coefficients to compute the conductance of the boundaries/interfaces as a function of both mismatch angle and carrier concentration. In Sec. 5.2 we further detail our approach and delineate two different classes of GBs (twin and tilt homojunctions) and interfaces (Class-I and II heterojunctions). In Sec. 5.3, we discuss our results showing that transport across twin homojunctions and Class-I heterojunctions show a weak dependence on mismatch angles, whereas the resistance across tilt homojunctions and Class-II heterojunctions exhibits a strong dependence on mismatch angles. We conclude in Sec. 5.4 that GBs play a moderate role in MoS_2 due to its parabolic bands, but can be quite significant in graphene and large-mismatch graphene-MoS_2 heterostructures owing to graphene's steep linear Dirac cones.

5.2 Theoretical approach

To study the impact of misorientation angles on interface resistance, we have developed a numerical model based on first-principles DFT electronic bandstructure calculations and electron transmission coefficients from simultaneous energy and momentum conservation. The latter is an extension of the approach originally proposed by Yazyev and Louie [196] to calculate the transmission coefficient of electrons across a graphene grain boundary. The interface resistance is calculated in the following steps: bandstructure calculations for graphene and MoS_2 individually from the first principles, rotation of the Brillouin zones (BZ) to account for the misorientation angle between adjacent grains, calculation of electron transmission across the interface from the energy and momentum conservation, and finally computing the interface resistance in the Landauer formalism. For heterojunctions between dissimilar materials, an additional second step involves band alignment at the interface based on the Schottky-Mott rule.

First, we calculate the electronic bandstructure for single-layer graphene and MoS_2 individually from first principles using Density Functional Theory (DFT) as implemented

within the open-source distribution Quantum Espresso [97] (further details on the DFT calculations are given in the Methods). It is followed by the alignment of the bands at the interface. In homojunctions such as graphene-graphene GBs and MoS_2-MoS_2 GBs, the bands are always well-aligned at the interface, whereas in heterojunctions, such as the graphene-MoS_2 GBs, the bands need to be aligned. In contrast to the planar charge in a 3D interface, a 2D heterojunction forms a line dipole at the junction [218, 214]. It has been shown that in 2D heterojunctions, the effect of this interfacial dipole vanishes when the overall dimensions of the device are much larger than the characteristic junction-width, typically about 10 nm [218]. As a result, the band alignment in 2D heterojunctions is far less sensitive to the interfacial details and the band alignment closely follows the Schottky-Mott rule [218].

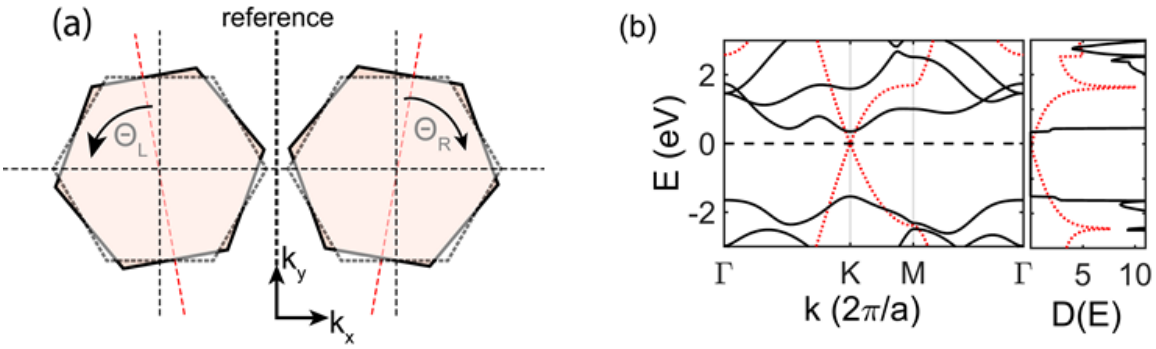

Figure 5.1: **(a)** shows orientation of the grains with respect to the interface. The dash-outlined hexagons represent the orientation of the Brillouin zones for perfectly matched condition ($\Theta_L = \Theta_R = 0°$). Θ_L is the angle of rotation, measured in anticlockwise direction, between the rotated left grain (solid-outlined hexagon) and the one for perfectly-matched condition (dash-outlined hexagon). Θ_R is the angle of rotation, measured in clockwise direction, between the rotated right grain and the grain for perfectly-matched condition. The total misorientation angle is then given as $\Theta_M = \Theta_L + \Theta_R$. **(b)** shows the bandstructure and density of states of graphene (in red) and MoS_2 (in black) computed from the first principles.

In our case, the graphene and MoS_2 are treated as semi-infinte, so we use the Schottky-Mott rule [219] and align the vacuum levels of the two materials at the interface. Next, the work function of graphene ($\phi_{graphene} = 4.55$ eV [220]) and the electron affinity of MoS_2

($\chi_{MoS_2} = 4.2$ eV [221]) are used to align the respective bands away from the interface relative to the vacuum level. Due to the difference in the work function of graphene and electron affinity of MoS_2, an energy barrier $\Phi_B(n_C) = \phi_{graphene}(n_C) - \chi_{MoS_2}$ is formed at the interface. As graphene is essentially metallic, the bands bend on the MoS_2 side near the interface to account for the energy barrier height in equilibrium. The amount of band-bending on MoS_2 side, which is also a function of carrier concentration n_C, is given by $\Phi_{interface}(n_C) = \phi_{MoS_2}(n_C) - \chi_{MoS_2} - \Phi_B(n_C)$ [84]. The carrier concentration typically depends on the level of impurities, doping, or gating [222, 223, 224].

The orientation of the grains with respect to the GB/interface is defined by two angles Θ_L and Θ_R, each being the angle of rotation between the grain on the left and the right side with respect to the interface, taken here as reference, as shown in Figure 5.1. According to our convention, Θ_L is taken to be positive for anticlockwise rotation of the left grain, whereas Θ_R is positive for clockwise rotation of the right grain. We define misorientation angle as $\Theta_M = \Theta_L + \Theta_R$. To include the effect of the misorientation angle in our calculation, the wavevectors in the first Brillouin zone are rotated by Θ_L for the left grain and Θ_R for the grain on the right hand side of the interface. The rotation of the Brillouin zone does not affect the aforementioned band structure alignment at the interface.

In 2D materials, GBs can be of different types depending on both the orientation of each grain with respect to the grain boundary and the orientation of the grains with respect to each other. One extreme is when both the grains are rotated symmetrically by equal angles away from the GB in opposite directions (i.e. $\Theta_L = \Theta_R = \Theta_M/2$) and the second is when only one of the grains is rotated away from the interface (i.e. $\Theta_L = 0^\circ, \Theta_R = \Theta_M$). In literature, the former type of symmetric grain boundaries are referred to as twin GBs and the latter as the most asymmetric tilt GBs.

So far, we have discussed the two extreme cases of GBs for a given misorientation angle Θ_M, but we can have many intermediate cases of tilt (asymmetric) GBs depending on the position of the boundary itself. For example, given that Θ_M is 4° we can have

$\Theta_L = \Theta_R = \Theta_M/2$ (twin GBs), or $\Theta_L = 0^\circ$ and $\Theta_R = \Theta_M$ (the most asymmetric tilt GB), or intermediate cases such as $\Theta_L = 1^\circ$ and $\Theta_R = 3^\circ$, and so on so forth. In order to denote these intermediate tilt cases, we introduce an angle Θ_B, which is defined as the angle, in the anticlockwise direction, that the boundary makes with the reference line. So, an intermediate case of $\Theta_L = 1^\circ$ and $\Theta_R = 3^\circ$ can be represented as $\Theta_M = 4^\circ$ and $\Theta_B = 1^\circ$.

The effect of GB/interface on transport is incorporated by using boundary conditions based on quantum-mechanical wave continuity [225]. From translational symmetry, transmission requires simultaneous conservation of energy and transverse momentum of the incident electron across the interface. Momentum conservation requires that the parallel component of the incident wave vector $k_{i_\parallel}$ be equal to the parallel component of the transmitted wave vector $k_{t_\parallel}$, in their respective domains that is $k_{t_\parallel} = k_{i_\parallel}$; simultaneously, energy is conserved by finding a perpendicular component of the transmitted wave vector $k_{t_\perp}$, within the first Brillouin zone of the right grain, such that $E_2(k_{t_\parallel} + k_{t_\perp}) = E_1(k_i) = E_1(k_{i_\parallel} + k_{i_\perp})$. Then we calculate the mode-dependent transmission coefficient $\tau_b(\vec{k})$ for each band b using the perpendicular components of the incident $k_{i_\perp}$ and transmitted $k_{t_\perp}$ wave vectors by the expression

$$\tau_b(k_i) = \frac{\mid 4k_{i_\perp} k_{t_\perp} \mid}{\mid k_{i_\perp} + k_{t_\perp} \mid^2} \tag{5.1}$$

Next, we obtain the energy-resolved transmission coefficient $\Gamma_b(E)$ by averaging the mode-dependent transmission coefficient $\tau_b(k)$ over the constant energy contour, described by $\delta(E - E_b(k))$, using the 2D version of the linear extrapolation approach described by Gilat and Raubenheimer [226] as

$$\Gamma_b(E) = \frac{1/4\pi^2 \int \tau_b(k_i)\delta(E - E_b(k_i))dk_i}{1/4\pi^2 \int \delta(E - E_b(k_i))dk_i} \tag{5.2}$$

The denominator of Eq. 5.2 is the density of states in band b $D_b(E)$, shown in Figure 5.1(b). The same transformation method is employed for converting the mode-dependent

velocity $v_{b_\parallel}(k)$ into energy-resolved velocity $v_{b_\parallel}(E)$ in the direction of transport. We then calculate the transport distribution function TDF $\Xi(E)$ as

$$\Xi(E) = \sum_b v_{b_\parallel}(E)\Gamma_b(E)D_b(E) \tag{5.3}$$

The TDF is then used to numerically calculate the grain boundary conductance in the Landauer formalism and inverted to obtain the grain boundary resistance $R_{GB/int.}(G^{-1}_{GB/int.})$. The grain boundary conductance is obtained from an integral of the product of TDF and Fermi window function $\partial f(E - E_F, T)/\partial E$ over energy

$$G_{GB/int.} = \frac{e^2}{2}\int_{E_C}^{E_{max}} \Xi(E)\left(-\frac{\partial f(E - E_F, T)}{\partial E}\right) dE \tag{5.4}$$

where E_C is the bottom of the conduction band and E_{max} is the highest electron energy in the first four conduction bands and $f(E)$ is the Fermi-Dirac distribution function $f(E) = [1 + exp((E - E_F)/k_BT)]^{-1}$.

5.3 Results and Discussion

Electron transport across graphene grain boundaries

We calculate the transmission and resistance of graphene GBs in order to explore the impact of the misorientation angle. The angle dependence of GB resistance largely depends on the type (tilt or twin) of the GB. Figure 5.2(a) and Figure 5.2(b) show transmission coefficient Γ(E) and GB resistance R_{GB} respectively for various misorientation angles in twin GBs. We see in Figure 5.2(a) that perfect transmission, that is transmission coefficient $\Gamma(E)$ equals 1, is obtained for 0° mismatch angle at any given energy level. However, as the misorientation angle increases, the modes that do not conserve energy and transverse momentum are reflected at the interface, resulting in a reduction of the transmission coefficient, which varies between 0.8 and 0.5 for various mismatch angles. Besides band gap,

the energy range for which there is no transmission (Γ(E)=0) is referred here as *transmission/transport gap*. In twin GBs, we note that even for large mismatch angles there is no transmission gap in the energy spectrum. For GBs with 0° mismatch angle, we obtain a

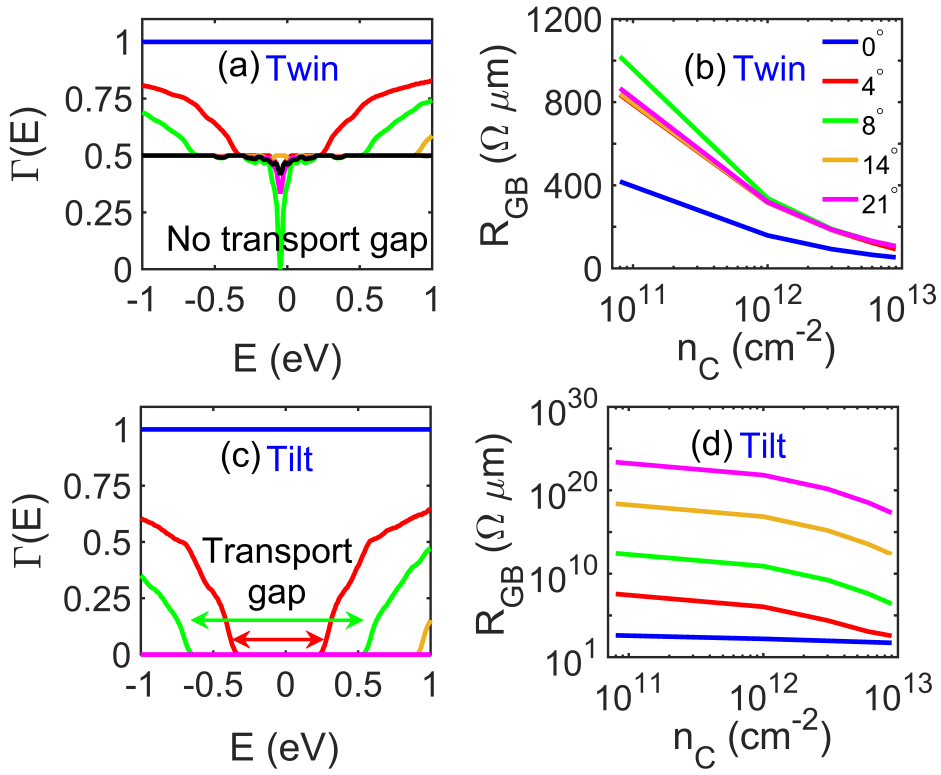

Figure 5.2: **(a)** shows transmission coefficient vs. energy for various misorientation angles across graphene twin grain boundaries. **(b)** shows the variation of grain boundary resistance with carrier concentration for the same mismatch angles as plotted in **(a)**. The curves for large mismatch angles (14° and 21°) are overlapping on each other in both **(a)** and **(b)**. Transmission coefficient vs. energy and the resultant GB resistance vs. carrier concentration for different misorientation angles in graphene tilt GBs are plotted in **(c)** and **(d)** respectively. A transmission gap opens up for tilt but not for twin GBs, resulting in much stronger angle dependence.

coefficient $\Gamma(E) = 1$; in contrast, Yazyev and Louie [196] reported a linear transmission probability $T(E)$ with energy. They used a non-equilibrium Green's function (NEGF) formalism to calculate conductance across graphene grain boundaries. In the coherent transport regime, the conductance from NEGF formalism reduces to the conductance in Landauer formalism [227], given by [228] $G = \frac{e^2}{h} \int T(E)(-\frac{\partial f(E-E_F,T)}{\partial E})dE$. Comparing this

with our conductance expression (Eqn. 5.4), we find that $T(E)$ in the NEGF formailsm is analogous to our transport distribution function $\Xi(E)$. For the graphene GBs with 0° mismatch, $\Xi(E)$ in Eqn. 5.3 is proportional to the DOS $D_b(E)$, which is linear with energy [as shown in Figure 5.1(b) and Eqn. 7.19]; thus our TDF is consistent with the $T(E)$ vs. energy plot from NEGF [196].

In Figure 5.2(b), the GB resistance is plotted for different misorientation angles and carrier concentrations. For a given carrier concentration, the GB resistance increases with misorientation angles. This is due to the reduction in transmission coefficient with increasing misorientation angle, as can be seen in Figure 5.2(a), which maps to an increase in GB resistance. Perfect transmission at 0° mismatch angle translates into ballistic resistance across graphene GBs as shown in Figure 7.2(b) in the Appendix [same as the blue curve in Figure 5.2(b) and (d)]. For a given mismatch angle, the GB resistance decreases with increasing carrier concentration as we can see in Figure 5.2(b). At intrinsic carrier concentration, the Fermi level E_F is near the Dirac point in graphene. But with the increase in electron concentration the Fermi level goes into the conduction band, and consequently, the Fermi window function $(-df/dE)$ which is centered at E_F also shifts towards higher energy levels. As the DOS in graphene is proportional to energy near the Dirac point (from Eqn. 7.19 and Figure 5.2(b)), the TDF $\Xi(E)$ also increases with energy away from the Dirac point. Thus the value of the integral in Eqn. 5.4, which is a product of TDF and Fermi window function, increases with carrier concentration. As a result, we see a decrease in GB resistance with increasing carrier concentration in Figure 5.2(b).

Figure 5.2(c) and Figure 5.2(d) show transmission coefficient Γ(E) and grain boundary resistance respectively for various mismatch angles in tilt grain boundaries. The transmission coefficient shows a similar reduction with increasing mismatch angles as seen in Figure 5.2(a); however the reduction is more pronounced than in the case of twin GBs. In tilt GBs we also observe a widening of the transmission gap, shown in the Figure 5.2(c), with increasing misorientation angle. This transmission gap around the Dirac point maps

into large GB resistance for large-angle tilt GBs and grain boundary resistance becomes less sensitive to the variation in carrier concentration.

Previously, it was found that the GB resistance across graphene GBs varies within a wide range from a few $\Omega\ \mu\mathrm{m}$ to several $\mathrm{k}\Omega\ \mu\mathrm{m}$ [6, 4]. The wide variation in GB resistance can be fully explained with the trends observed in Figure 5.2(b) and Figure 5.2(d): there is a large difference in resistance between twin and tilt GBs, with twin GBs being less sensitive to misorientation angles as compared to the tilt GBs. The GB resistance in tilt GBs range from about 350 $\Omega\ \mu\mathrm{m}$ at 4° mismatch to several thousands of $\mathrm{G}\Omega\ \mu\mathrm{m}$ at 14° mismatch, even at high carrier concentration of about $10^{13}\ \mathrm{cm}^{-2}$. The transmission coefficient eventually becomes zero for misorientation angles beyond 14° mismatch due to the large transmission gap in tilt GBs and we observe extremely high values of resistances. In contrast, the resistance of twin GBs in near-intrinsic graphene varies from 400 $\Omega\ \mu\mathrm{m}$ at low to about 1 $\mathrm{k}\Omega\ \mu\mathrm{m}$ at high mismatch angles, while at high carrier concentration it varies over a very narrow range of about 90 $\Omega\ \mu\mathrm{m}$ at 4° mismatch to 110 $\Omega\ \mu\mathrm{m}$ at 14° mismatch. Our calculated graphene GB resistances include a ballistic resistance of 53 $\Omega\ \mu\mathrm{m}$ at high carrier concentration of $10^{13}\ \mathrm{cm}^{-2}$ and 424 $\Omega\ \mu\mathrm{m}$ at intrinsic carrier concentration. After removing the ballistic resistance, the calculated GB resistance for a low-mismatch twin GBs of about 1° at high carrier concentration is 8 $\Omega\ \mu\mathrm{m}$. This is in good agreement with Grosse et al. [7].

Electron transport across MoS_2 grain boundaries

To study electronic resistance across MoS_2 GBs, we use the same procedure as used for graphene GBs in the previous section. The transmission coefficient as a function of energy is plotted in Figure 5.3(a) for different misorientation angles in twin GBs. The blue curve shows transmission across an imaginary, perfectly-matched grain boundary (which corresponds to 0° mismatch). A perfect transmission is obtained for energies greater than about 0.94 eV and less than about -0.94 eV. Zero transmission at energies between -0.94

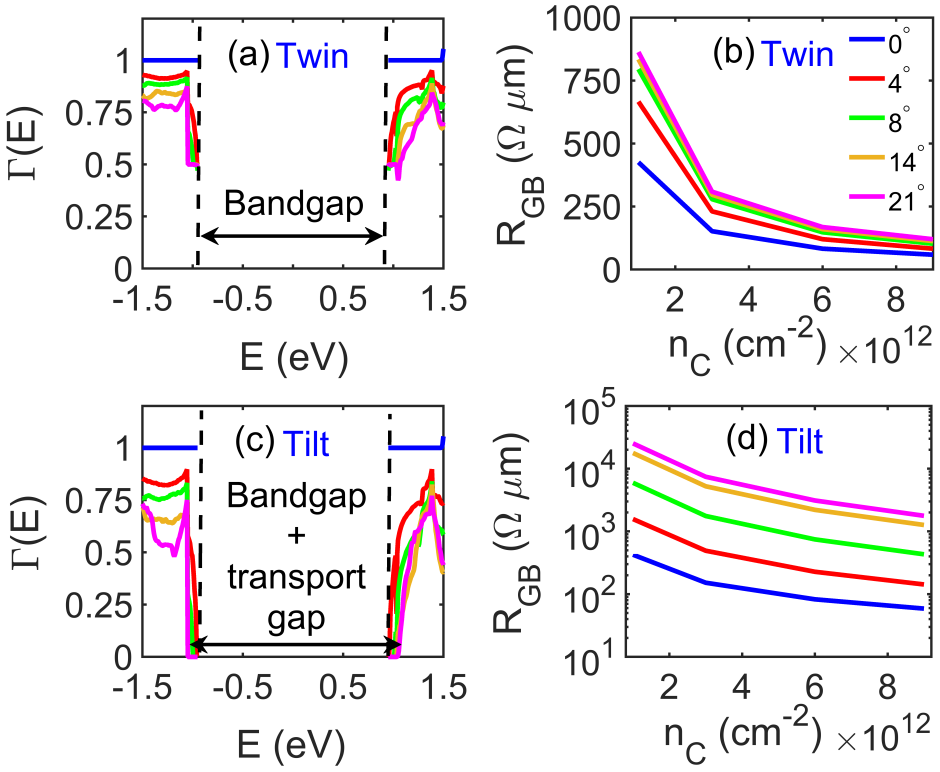

Figure 5.3: **(a)** shows transmission coefficient vs. energy for various misorientation angles across MoS_2 twin grain boundaries. **(b)** shows the variation of grain boundary resistance with carrier concentration for the same mismatch angles as plotted in **(a)**. Transmission coefficient vs. energy and the resultant GB resistance vs. carrier concentration for different misorientation angles in MoS_2 tilt GBs are plotted in **(c)** and **(d)** respectively. Besides intrinsic band gap, an additional transmission gap opens up for large tilt GBs.

eV and 0.94 eV corresponds to the energy band gap of 1.88 eV in intrinsic MoS_2. We also observe a gradual reduction in transmission coefficient with increasing misorientation angles as compared to that of graphene GBs. However, there is no transmission gap found for MoS_2 twin GBs, similar to what we observed in graphene twin GBs. Corresponding to the transmission coefficient for various misorientation angles, the boundary resistance across MoS_2 twin grain boundaries vs. carrier concentration is shown in Figure 5.3(b). We note that the values of R_{GB} in MoS_2 twin GBs are almost double than the values of GB resistance in graphene twin boundaries for a carrier concentration of 1×10^{12} cm^{-2},

whereas for large carrier concentrations between 6×10^{12} and 9×10^{12} cm^{-2}, MoS_2 twin GBs have GB resistance similar to that of graphene twin GBs.

Figure 5.3(c) and Figure 5.3(d) show transmission coefficient vs. energy and GB resistance vs. carrier concentration respectively for various misorientation angles in MoS_2 tilt GBs. It can be seen in Figure 5.3(c) that the transmission coefficient decreases with increasing misorientation angle and the rate of reduction of transmission coefficient is more rapid than what was observed in MoS_2 twin GBs. Like in tilt graphene GBs, a transmission gap is also observed in tilt MoS_2 GBs for large misorientation angles, however the transmission gap in MoS_2 is much smaller than that of graphene. We attribute this trend to the flatter parabolic conduction band bottom of MoS_2 as compared to the steep conical bandstructure of graphene around the Dirac point. The variation of GB resistance with misorientation angle is quite distinct in this case as compared to the variation of R_{GB} in graphene tilt GBs. It is important to note that the resistance across MoS_2 GBs is much smaller than what we found in graphene tilt GBs. Thus, misorientation of adjacent grains across grain boundaries can cause a significant reduction in electronic conductance in polycrystalline graphene, while GBs in polycrystalline MoS_2 might not play such a strong role in electron conduction, which is in good agreement with few recent reports on electronic transport in CVD-grown MoS_2 [206, 202].

Figure 5.4(a) and (b) depict the surface plots of GB resistance vs. Θ_M and Θ_B for graphene and MoS_2 GBs respectively. The calculated value of resistances across graphene GBs range from few tens of $\Omega\ \mu\mathrm{m}$ to about $10^{13}\ \Omega\ \mu\mathrm{m}$ depending on the Θ_M (the angle between the two grains) and Θ_B (the position of the boundary with respect to the left grain). However, the GB resistance across MoS_2 GBs vary over a relatively narrow range of about $130\ \Omega\ \mu\mathrm{m}$ to $5700\ \Omega\ \mu\mathrm{m}$ for various combinations of Θ_M and Θ_B. Thus, we can see that for a given misorientation angle, one can have different GB resistance depending on the position of the GB with respect to the grains, and any resistance value falling in this range can be explained by a combination Θ_M and Θ_B.

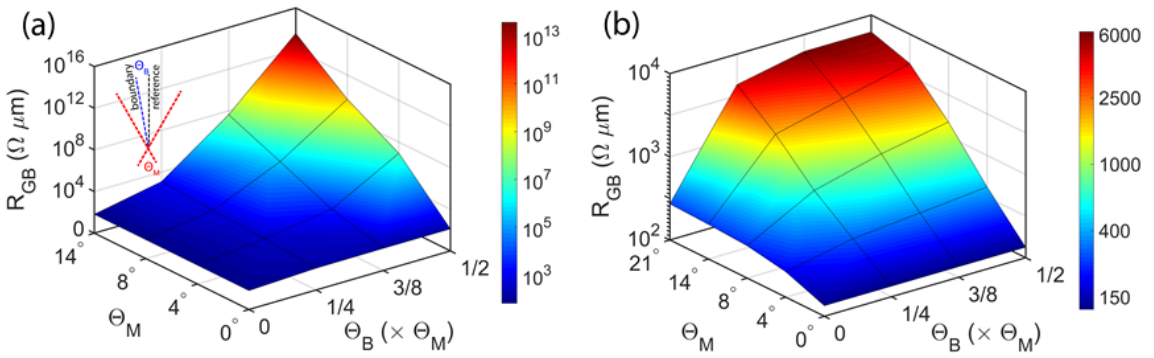

Figure 5.4: shows resistance **(a)** across graphene GBs and **(b)** across MoS_2 GBs vs. misorientation angles Θ_M and various combinations of Θ_L and Θ_R, represented as Θ_B for a given Θ_M. Here Θ_B is expressed as a fraction of Θ_M.

Electron transport across graphene-MoS_2 interfaces

The interfaces formed between two dissimilar materials (heterojunctions) are different from those of homojunctions because of the difference in the properties of the grains on either side of the interface—including electron affinity, work function, and bandstructure. So, before discussing about electron transport across such heterojunctions, we redefine the nomenclature of the interfaces formed between graphene and MoS_2 to differentiate with those of homojunctions. When graphene (taken here to be on left side of the boundary) and MoS_2 (right side of the boundary) grains are rotated by equal angles with respect to the interface i.e. $\Theta_L = \Theta_R$, we use the term Class-I interface, whereas when $\Theta_L \neq \Theta_R$ we call them Class-II interfaces in this work.

Figure 5.5(a) shows the thermionic transmission of the electrons across graphene-MoS_2 Class-I interface for various misorientation angles at a carrier concentration of 1×10^{12} cm^{-2}. Due to the difference in the work function and electron affinity in graphene and MoS_2, the bands bend and an energy barrier (the energy difference between fermi-level, approximately equal to 0 eV in Figure 5.5(a) and (c), to the bottom of the conduction band of MoS_2 at the interface where the transmission of electrons start) is formed at the interface. Like in homojunctions, the band alignment at the interface is independent of the misorientation angle, and thus, the barrier height is also independent of Θ_M. In Figure 5.5(b),

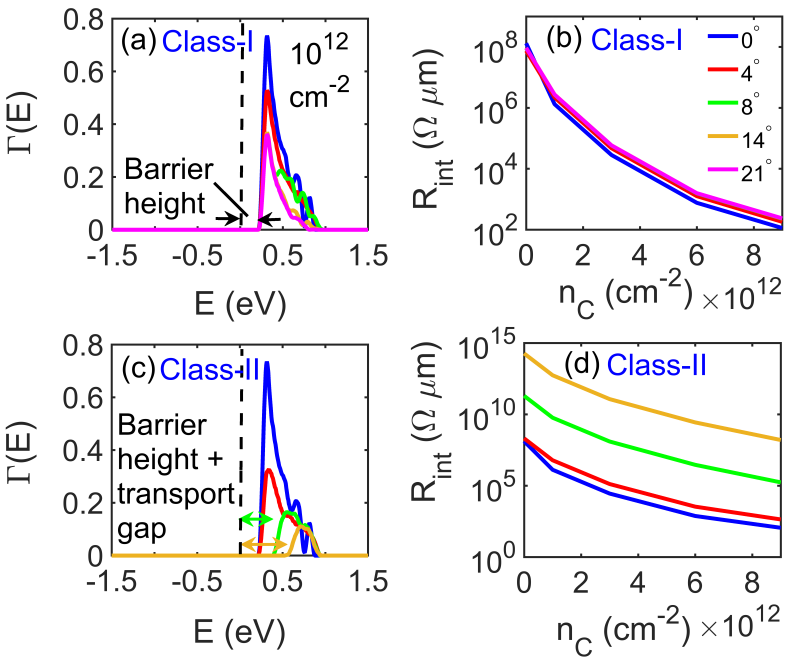

Figure 5.5: **(a)** shows transmission coefficient vs. energy for various misorientation angles across graphene-MoS_2 Class-I interfaces. **(b)** shows the variation of interface resistance with carrier concentration for the same mismatch angles as plotted in **(a)**. Class-I graphene-MoS_2 interfaces show neglibible sensitivity towards misorientation angles. **(c)** shows transmission coefficient vs. energy for different misorientation angles in graphene-MoS_2 Class-II interfaces. On top of intrinsic barrier height, an additional transmission gap opens up for such Class-II graphene-MoS_2 interfaces. The resulting interface resistance in Class-II interfaces vs. carrier concentration for different misorientation angles are plotted in **(d)**.

we see that at low carrier concentrations of about 1×10^{12} cm^{-2}, the interface resistance is in the order of 10^8 Ω μm because of the large energy barrier. However, at high carrier concentrations between 6×10^{12} cm^{-2} and 9×10^{12} cm^{-2}, the interface resistance reduces significantly because the energy barrier between graphene and MoS_2 almost disappears at such concentrations and they behave like Ohmic contacts.

Figure 5.5(c) shows transmission coefficient vs. energy for various misorientation angles in Class-II graphene-MoS_2 interfaces at a carrier concentration of 1×10^{12} cm^{-2}. The transmission coefficient decreases with increasing mismatch angle similar to the tilt GBs in graphene GBs. A transmission gap is formed in addition to the existing potential bar-

rier, marked in the figure, and this transmission gap widens with increasing misorientation angles. Transmission becomes zero for large mismatch angles beyond 14°. This strong dependence of mismatch angle on transmission coefficient leads to a strong dependence of the interface resistance on misorientation angles in Class-II graphene-MoS_2 heterojunctions, which can be seen in Figure 5.5(d). At a carrier concentration of 1×10^{12} cm^{-2}, the interface resistance varies from about 10^{8} for low mismatch angles to 10^{14} Ω μm for a mismatch of 14°, whereas at high concentrations the interface resistance ranges from about 10^{2} for low mismatch angles to 10^{8} Ω μm for a mismatch of 14°.

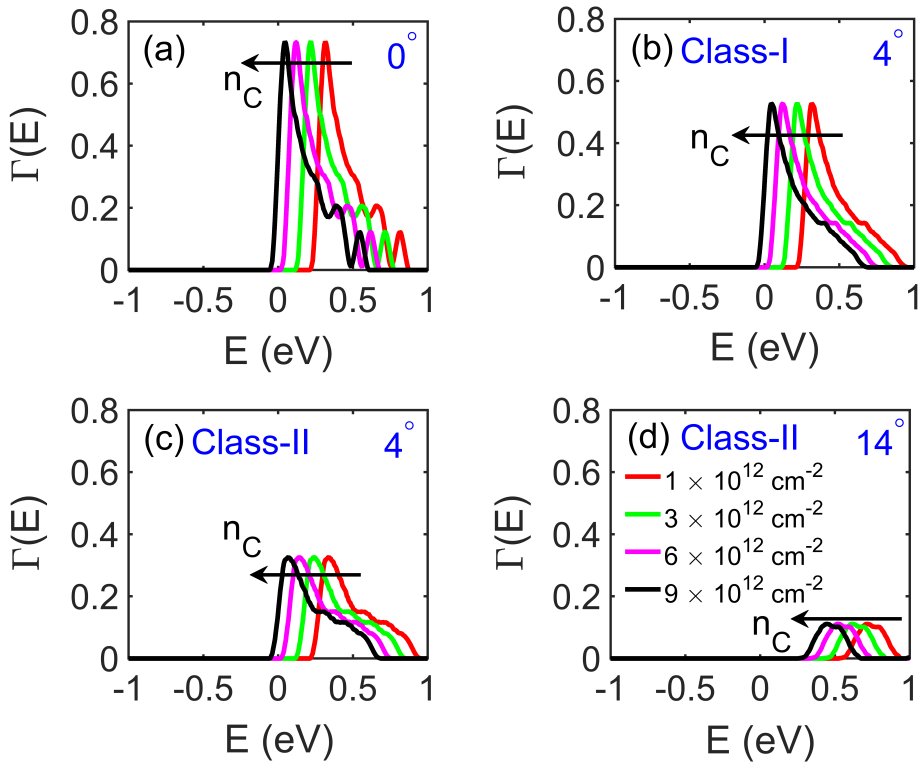

Figure 5.6: show transmission coefficient vs. energy for various carrier densities **(a)** for 0° mismatch, **(b)-(c)** for 4° in Class-I and Class-II graphene-MoS_2 interfaces respectively, and **(d)** for 14° mismatch in Class II interfaces.

In homojunctions like graphene-graphene and MoS_2-MoS_2 GBs, the band alignment is independent of the position of the Fermi level so the transmission coefficient is also independent of carrier concentration. In contrast, the barrier height in heterojunctions is a

function of carrier concentration via the position of the Fermi level, owing to the difference in DOS between graphene and MoS_2. The transmission coefficient in Class-I graphene-MoS_2 interface is plotted with carrier concentration in Figure 5.6. Figure 5.6(a) shows the transmission coefficient vs. energy for perfectly matched graphene-MoS_2 interface, that is 0° mismatch. The shape of the Γ(E) vs. energy does not change with carrier concentration rather the curves get shifted towards the left in energy due to the decrease in energy barrier height with carrier concentration. In Figure 5.6(b) and (c), the transmission coefficient vs. energy is plotted for 4° mismatch in Class I and II heterojunctions respectively. The decrease in the magnitude of transmission coefficient as compared to that of Figure 5.6(a) is more pronounced for Class II than Class-I interfaces. For large misorientation angles, that is beyond 14° the transmission coefficient in Class II interfaces becomes very small about 0.1 eV as can be seen in Figure 5.6(d), whereas for Class I heterojunctions the transmission coefficient peak is about 0.4 eV (shown by the green curve in Figure 5.5(a), noting that a change in carrier concentration only shifts the Γ vs E curve and does not change the shape).

Figure 5.7 shows a comparison of the interface resistance among Gr-Gr, MoS_2-MoS_2, and Gr-MoS_2 interfaces. It can be seen that, in general, symmetric twin GBs in homojunctions and Class-I interfaces in heterojunctions show a very weak dependence on the degree of mismatch between adjacent grains, whereas tilt GBs in homojunctions and Class-II interfaces in heterojunctions exhibit strong dependence on misorientation angles except in MoS_2, where both tilt and twin GBs are found to show a weak dependence on mismatch angles. The weak angle dependence in MoS_2-MoS_2 GBs can be attributed to the flat parabolic conduction band because of which the underlap in the bandstructures on the either side of the GB is quite small even at large mismatch angles. In order to explain the wide range of the graphene GB resistances in the literature via misorientation angle and type of GBs, the data from the literature has also been included in the figure. The yellow markers in the figure denote the combinations of Θ_M and Θ_B obtained by fitting the experimental measurements by Kochat et al. [3] ($\Theta_B = 2.83^\circ$ and 3° for $\Theta_M = 12^\circ$ and 22° respectively),

Clark et al. [2] ($\Theta_B = 0°$, $0.2°$ and $0.75°$ for $\Theta_M = 9°$, $14°$, and $21°$ respectively), and Yu et al. [4] ($\Theta_B = 3.1°$ for $\Theta_M = 28°$).

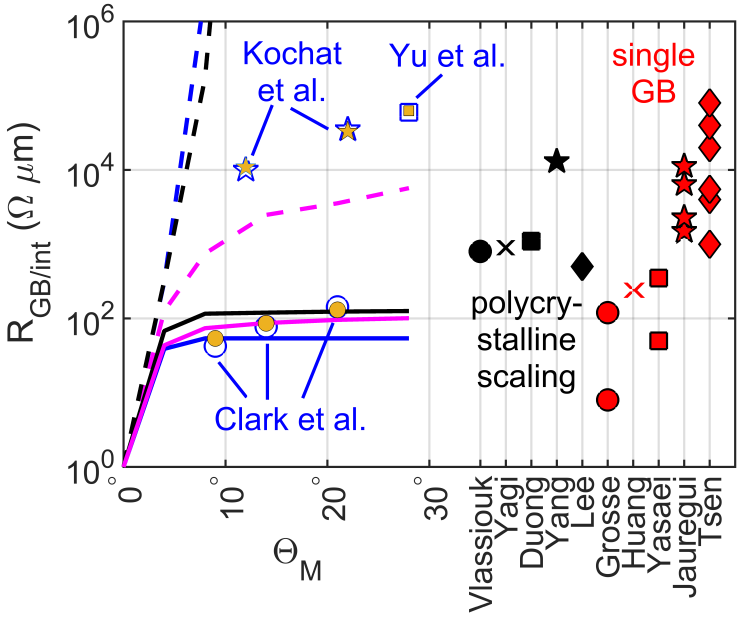

Figure 5.7: compares the calculated GB/interface resistance vs. misorientation angles across twin (solid lines) and tilt (dashed lines) Gr-Gr (shown in blue) and MoS_2-MoS_2 (shown in magenta) GBs, and Class-I (solid black line) and Class-II (dashed black line) Gr-MoS_2 interfaces. The reported values of graphene GB resistance in the literature are also plotted in this figure. The data for graphene GB resistance which are available with misorientation angles are plotted with blue markers [2, 3, 4]. The other studies about graphene GB resistance where mismatch angle wasn't mentioned explicitly are plotted on the right with red and black markers. The red markers are the resistance values from literature across single graphene GB [5, 6, 7, 8, 9]. The black markers are for the literature data on GB resistance extracted by polycrystalline scaling from polycrystalline samples [10, 11, 12, 13, 14].The yellow markers represent the calculated graphene GB resistance corresponding to those combinations of Θ_M and Θ_B which fit the experimental measurements.

The aim of our study is to understand the effect of misorientation angle on GB conductance. There could be additional effect due to grain boundary roughness [116] and the presence of localized electronic states, which have been observed at 3D interfaces [229] and 2D grain boundaries [230, 231, 205]. The localized states are not included in our model, but could be treated by modifying $D_b(E)$ in Eqn. 5.3. The presence of localized

interface states could lead to two types of behavior, depending on the magnitude of the transport gap. For low mismatch angles or symmetric GBs where the transport gap is small and the transmission coefficient is close to unity, the localized states and roughness at the GB would reduce the transmission coefficient; in that case, our calculated conductance values can be thought of as an upper bound. For large mismatch angles, we found a wide transport gap where transmission is zero, especially in graphene GBs and graphene-MoS_2 interfaces. Then localized states might introduce additional channels for transmission and lead to slightly higher GB conductance than what we report here without these localized states. In that sense, our conductance values could be thought of as a lower bound.

5.4 Conclusion

In conclusion, we find that misorientation angle between two adjacent grains plays a very significant role in both homojunctions and heterojunctions. We show that the resistance across graphene GBs and graphene-MoS_2 interfaces varies over a very wide range depending on the degree of mismatch between adjacent grains and type of GBs. The transmission coefficient across symmetric interfaces (twin GBs in homojunctions and Class-I interfaces in heterojunctions) is found to be less sensitive to misorientation angles between adjacent grains because they deflect electrons rather coherently. In these symmetric interfaces, there is no transmission gap. On the other hand, the transmission across asymmetric interfaces (tilt GBs in homojunctions and Class-II interfaces in heterojunctions) is largely diminished by mismatch angles and a transmission gap opens up in the energy spectrum. In contrast to graphene-graphene tilt GBs, the resistance across MoS_2-MoS_2 tilt GBs show relatively much weaker dependence on mismatch angles. This is attributed to the flat parabolic conduction band bottom in MoS_2 as compared to the steep conical conduction band bottom in graphene. As a result, the rotation of the BZ in MoS_2 by large angles causes a small transmission gap, whereas even a small misorientation angle across graphene GBs gives rise to a large transmission gap. In homojunctions, the bands are identical on either side of the

interface and the response to the carrier concentration, and hence the back-gated voltage, is also uniform on both sides. Thus, for a given misorientation angle, the variation of transmission coefficient vs. energy is independent of carrier concentration in homojunctions. In heterojunctions, the bands are aligned at the interface using the macroscopic variables, including work function and electron affinity, based on Schottky-Mott rule, forming an energy barrier at the interface. The band alignment, and with it the energy barrier between graphene and MoS_2, reduces with the carrier concentration because of the differences in their densities-of-states. Consequently, the interface resistance strongly decreases with carrier concentration in heterojunctions in both classes of interfaces. In summary, electrical transport across twin homojunctions and Class-I heterojunctions shows a weak dependence on mismatch angles, whereas the resistance across tilt homojunctions and Class-II heterojunctions exhibits a strong dependence on mismatch angles.

CHAPTER 6

ELECTRONIC TRANSPORT ACROSS EXTENDED GRAIN BOUNDARIES IN GRAPHENE

6.1 Introduction

Over the last 50 years, dimension scaling of transistors in integrated circuits has been accompanied by shrinking the dimension of interconnects and vias, typically made of copper. Current state-of-the-art uses polycrystalline copper interconnects as thin as 10 nm. However, due to the increased surface roughness and grain boundary (GB) scattering, the resistivity of copper increases exponentially below 100 nm which imposes a limit to further downscaling of copper interconnects [49]. This limitation has led to extensive research in finding a suitable alternative which can replace copper in the next-generation nanoelectronic devices and circuits. Owing to the ultrathin nature and superior carrier mobility, graphene is envisioned as a promising candidate for interconnects and contacts in the emerging integrated circuits [232, 233, 234]. The dimension of mechanically exfoliated single crystalline graphene grains are limited to few tens of microns, however, commercial integration as interconnects would require wafer-scale manufacturing. Currently, chemical vapor deposition (CVD) on metal substrates is the most commonly used technique to grow such large-area 2D sheets [235, 236, 237, 116]. Controlled growth and nucleation processes using low-pressure CVD, adjusting content of oxygen on the surface of Cu substrate, and replacing methane with ethanol as carbon source have yielded single crystals up to a centimeter [235, 31, 238] and films up to 30 inches [239] in dimension.

CVD-grown graphene is, inherently, polycrystalline in nature. It consists of grains of various sizes and random crystallographic orientations, where every pair of adjacent grains

are separated by a GB. The difference in crystallographic orientation between adjacent grains—often referred to as *misorientation angle* Θ_{M}—results in mismatch in the crystal structure at their junction. Based on the substrate imperfections and factors governing the growth process, GBs may contain topological defects and have wrinkles of varying width up to 20 nm [2, 116, 240]. In general, GBs are found to limit electrical performance of graphene transistors [241]. Several experimental studies [8, 6, 242] have been carried out to understand the effect of Θ_{M} on electrical transport properties in graphene. The resistivity of individual GB (ρ_{GB}) varies over a wide range—few hundred Ω μm [7, 2] to several tens of kΩ μm [4, 5, 191] and shows no clear correlation with Θ_{M}. Imaging GBs using optical [243], scanning electron [244] and high resolution scanning transmission electron microscopes [245, 246] reveals that GBs are straight lines only in microscopic scale, upto few nanometers. Typically, the average length of the GBs may extend from few hundred nanometers to few microns and over this macroscopic length scale, the GBs are rarely straight lines rather they meander between two grains.

In contrast to experimental findings, there are a few theoretical studies that have investigated the effect of Θ_{M} on graphene ρ_{GB} and found a strong correlation between them [247, 196, 248, 249]. These studies reveal the opening of an energy transport gap—a consequence of the simultaneous energy and momentum conservation of a quantum-mechanical wave traveling across an interface [225]—the size of which depends on the Θ_{M} and the symmetry of the GBs. The ρ_{GB} depends very strongly on the size of the transport gap as the number of carriers contributing to transport depends exponentially on the size of the gap. It has also been shown that ρ_{GB} does not only depend on the total Θ_{M}, but exhibits a strong dependence on the degree of asymmetry of GBs which is given by the relative angles between the boundary and the crystallographic orientations of each grain. In asymmetric GBs with large Θ_{M}, the transport gap is so large that ρ_{GB} is 20 orders of magnitude larger than those with small Θ_{M} [249]. These theoretical studies have investigated GBs only at micro-scale level, upto few nanometers, and assumed GBs to be straight

lines [200, 249] which is not representative of actual (experimentally-observed) GBs. Consequently, the prediction of ρ_{GB} deviates significantly from experimental measurements. To distinguish between previous theoretical studies where researchers have investigated GBs at micro-scale level, and assumed GBs to be straight lines, we call GBs at macroscopic level as extended/non-straight GBs. There has not been any attempt made, so far, to examine the impact of zig-zagness on the resistivity of extended graphene GBs.

In order to simulate transport across and in the vicinity of extended GBs, we developed a two-step approach. The first step is to use a generalized autocorrelation function that satisfies the requirements for generating isotropic self-affine 1D boundaries with given roughness Δ and lateral correlation lengths L_{corr}. Then we employed a method developed in our previous work [249] to calculate the transmission of charge carriers across each GB segment based on energy and momentum conservation principle and extended it to study transport across these non-straight GBs. Our results clearly show that the meandering nature of a GB yields a few highly conductive GB segments, and consequently, the overall resistivity of actual GBs always falls within a universal range of 10^2 to 10^4 Ω μm, irrespective of the misorientation angles. The range of resistivity values align quite well with those measured experimentally. The conductive segments are found to be the ones which bisect the relative crystallographic angles of the grains constituting the boundary. We show that the ρ_{GB} is inversely proportional to the effective slope of the GB, given by Δ/L_{corr}. In the second step, we developed a new approach to study the effect of spreading resistance on electrical transport in graphene samples with extended GBs. The method uses a 2D Voronoi tessellation (VT) to emulate an extended GB and simultaneously discretize the grains on either sides of the GB into small simulation cells. Then we iteratively solved for the current in each discretized Voronoi cell to obtain a steady-state voltage profile. Our results corroborate that even in the presence of grain resistance, most voltage drop occurs near the GB and the current curves in graphene grains to flow through the few conductive segments of a GB giving rise to spreading resistance. The spreading resistance that results

from the longer current path is found to be directly proportional to the resistance of the graphene grains.

6.2 Methodology

6.2.1 Simulation of non-straight GBs

In the past, researchers have generated 2D self-affine surfaces from their autocorrelation functions for understanding the effect of surface roughness on several physical properties of materials [250, 251, 252]. Here we used a generalized autocorrelation function of the form [253]

$$C(x) = \Delta^2 \exp\left[-\left(\frac{\mid x \mid}{L_{corr}}\right)^{2H}\right]$$

to generate non-straight GBs with a given rms roughness (Δ) and correlation length (L_{corr}). Several natural surfaces used in various engineering applications are shown to exhibit a Hurst exponent (H) greater than 0.7 [254]. The values of H vary between 0 and 1, where higher values represent rough lines with smoother peaks and hence less roughness. We have used H=1, where peaks resemble gaussian curves, here in this study to simulate extended boundaries. Then we calculated the power density spectrum S(q) of the autocorrelation function as

$$S(q) = \mathscr{F}[C(x)],$$

where $\mathscr{F}$ is the Fourier transform. To generate correlated heights (h) for a range of x, we first multiply the square root of S(q) with a random phase $e^{i\phi}$ generated by taking Fourier transform of a randomly distributed points and then take an inverse Fourier transform of the product as

$$h(x) = \mathscr{F}^{-1}[\sqrt{S(q)}e^{i\phi}].$$

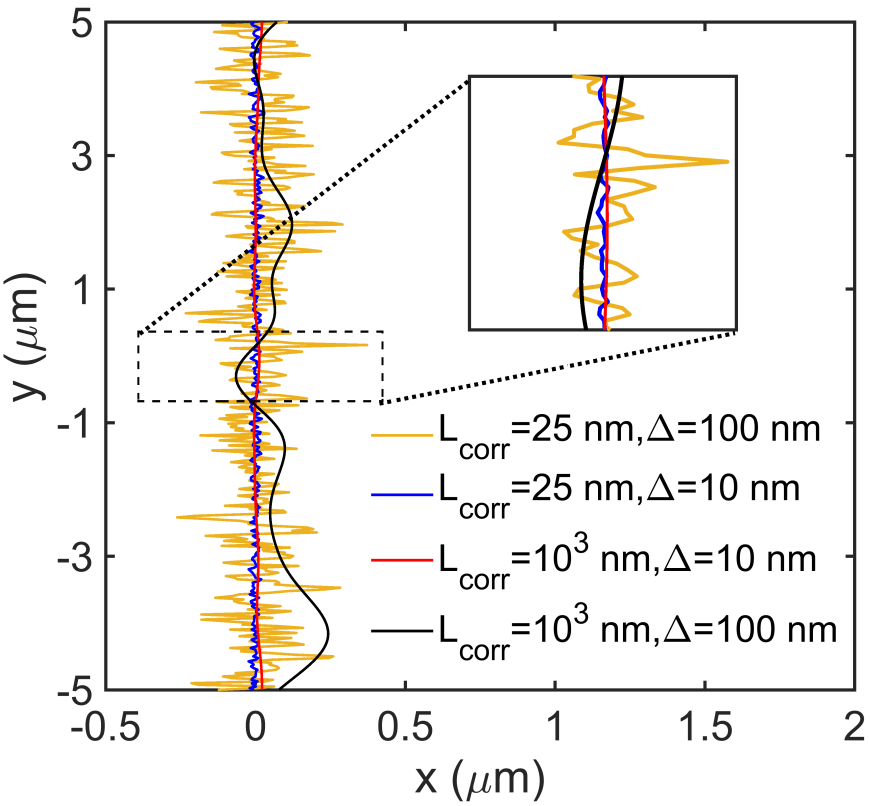

Figure 6.1: shows non-straight GBs with different rms roughness (Δ) and correlation lengths (L_{corr}). The red and blue lines represent highly correlated and uncorrelated GBs, respectively, with small Δ, whereas the black and yellow curves represent GBs with large Δ for L_{corr} equal to 1000 and 25 nm, respectively. The inset shows a zoomed-in view of the various non-straight GBs.

Fig.6.1 shows a 10 μm-wide non-straight GBs with different L_{corr} and Δ. The yellow and blue curves are for a small correlation length (L_{corr}=25 nm) and different rms roughness (100 and 10 nm, respectively), whereas the black and red lines correspond to GBs with large correlation length (L_{corr}= 1 μm) and Δ equal to 100 and 10 nm, respectively. The inset shows a zoomed view of a region for these GBs. The regions on the left and right-hand side of the GB are the two grains with crystallographic angles of x$^\circ$ and y$^\circ$, respectively, with respect to the y-axis, such that x$^\circ$ + y$^\circ$ = Θ_{M}. Each GB segment makes a different angle with the crystal orientation of the left and right grains, which we refer here as Θ_L and Θ_R, respectively.

6.2.2 Calculation of GB resistivity

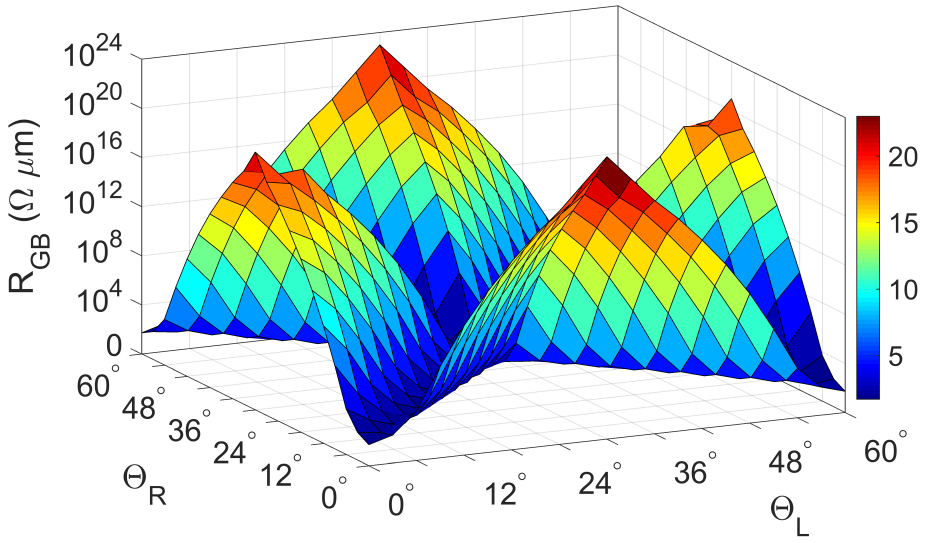

Figure 6.2: shows the resistivity ρ_{GB} for various combinations of Θ_{L} and Θ_{R}. The color bar represents the ρ_{GB} in log scale [$\log_{10}\rho_{GB}$]. The regions with blue color represents low resistivity and red color stands for high resistivity.

Next, we compute the resistivity of each segment corresponding to the pair of angles, Θ_{L} and Θ_{R}. The details of the theoretical approach used for the calculation of resistivity of each segments is given by equations 5.1-5.4 in Chapter 5.2. A carrier density of 6×10^{16} m^{-2} is used to compute the GB resistivity. The dependence of ρ_{GB} on any combination of Θ_{L} and Θ_{R} is summarized in Fig. 6.2. Symmetric GBs (Θ_{L}=Θ_{R}) exhibit the smallest resistivity in the order of 10^2 Ω μm, whereas the asymmetric GBs show orders of magnitude higher resistivity which is due to the opening of a transport gap [247, 196, 248, 249]. Based on the Θ_{L} and Θ_{R} corresponding to each GB segment, we calculate their resistivity ρ^i_{GB}. Since the GB segments are parallel channels for the charge carriers, the overall GB conductance is given by the sum of the conductance of all the segments, $G_{GB} = \Sigma_i[(\rho^i_{GB})^{-1} \times L^i_{GB}]$, where L^i_{GB} represents the length of the ith GB segment. Then the GB resistivity is calculated as $\rho_{GB} = [G_{GB}]^{-1} \times L_{GB}$, where L_{GB} is the length of the GB. The method discussed above computes the ballistic resistance across any non-straight GB with given Δ, L_{corr} and Θ_M. But to get a complete picture of electron

transport across a graphene sample with GB, it is essential that we solve for the voltage profile between two contacts where both grains and GB are present simultaneously in the calculation. Therefore, we developed an interesting approach using a 2D-Voronoi Tessellation (VT) to emulate a non-straight GB while also using it as a tool to discretize the grains.

6.2.3 Calculation of steady-state current and spreading resistance

Voronoi tessellation (VT) has been widely used in the past to emulate the microstructure of polycrystalline materials for both 2D [194] as well as three-dimensional materials [255]. Here we employ a 2D-VT to mimic non-straight GBs. The 2D-VT starts with a set of points (also called seed points) uniformly distributed in a 2D plane. The space is then divided into subspaces around each seed point called Voronoi cell such that all the points inside any given Voronoi cell is spatially closest to the seed point associated with it than any other seed points. In other words, these seed points are the centroids (center of mass) of the respective Voronoi cells, and hence this method is also called centroidal Voronoi tessellation (CVT). The number of Voronoi cells that would be generated is equal to the number of seed points, N. The network of non-overlapping polygons thus formed is called Voronoi diagram as shown in Fig. 6.3. The Voronoi cells are grouped to form two grains. The left grain comprises of all the Voronoi cells whose centers are located on the left of the red-dotted line, which bisects the Voronoi diagram laterally. The right grain consists of the remaining Voronoi cells, whose centers are located on the right of the red-dotted line. The zig-zag line separating the two grains forms a non-straight GB, as shown by the blue line in Fig. 6.3. Then we follow a similar approach as discussed above to calculate the local orientations of each GB segment with respect to the orientations of the left and right grains, indicated by Θ_{L} and Θ_{R}, respectively, as shown in the inset of Fig. 6.3.

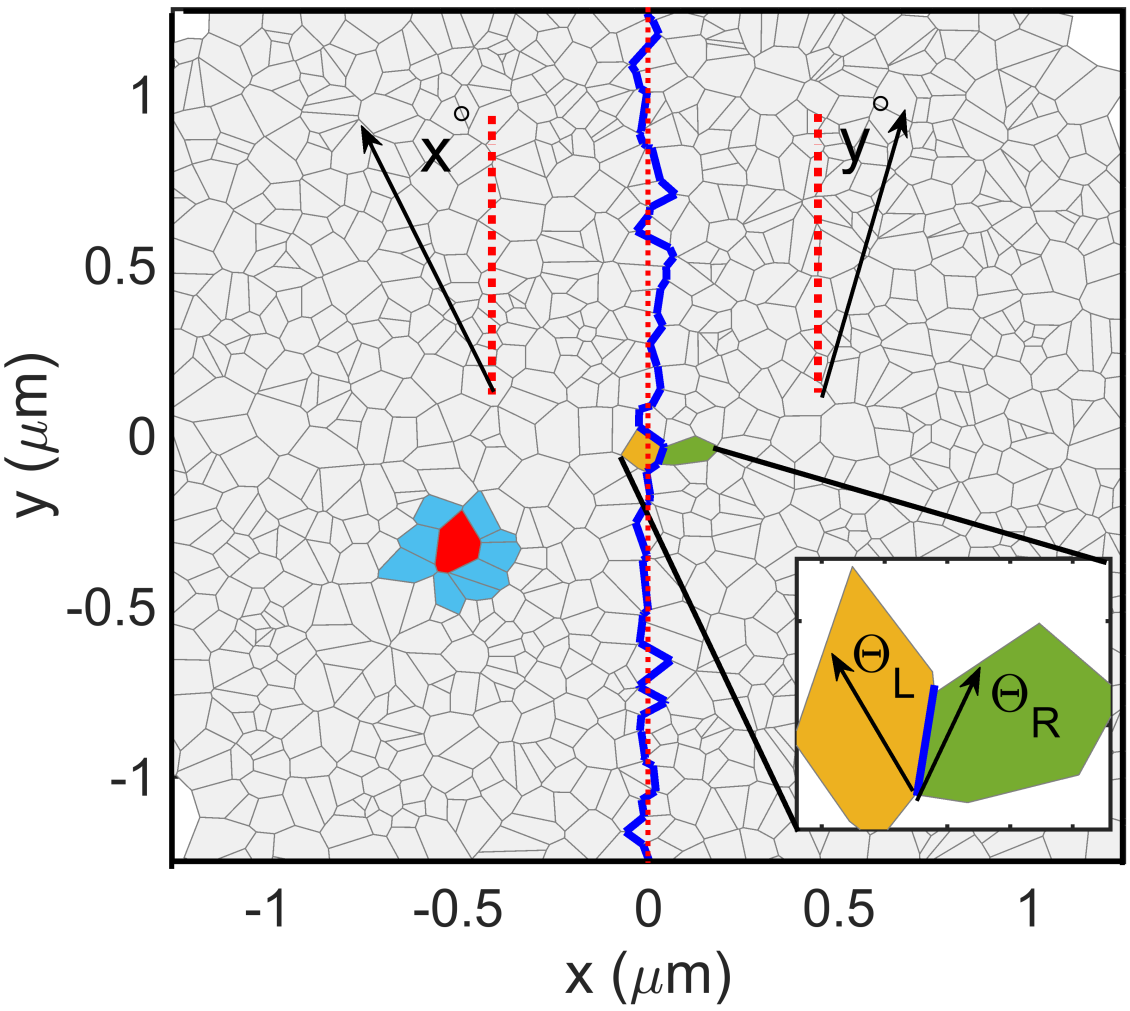

Figure 6.3: shows a Voronoi diagram obtained from 2D-VT. All the Voronoi cells on the left of the blue line form the left grain and the ones on the right side constitute the right grain. The left and right grains have crystal orientations at angles x° and y°, respectively, measured with respect to the y-direction. The blue line represents the GB between the left and right grains. The orientations of the left and right grains relative to the GB is given by Θ_{L} and Θ_{R}, as shown in the inset of the figure.

Then one Volt is applied in a region on the left side of the sample shown in Fig. 6.3 and a region on the extreme right of the sample is grounded. Then we, iteratively, updated the voltage of all the Voronoi cells to compute the steady-state current flowing through the entire graphene sample. In the steady state condition, the net current flowing through the boundaries (in and out) of each Voronoi cell must be zero. Mathematically,

$$\sum_j I_{ij} = 0, \forall\, i, \tag{6.1}$$

where the index j represents the first neighboring Voronoi cells, shown in blue in Fig. 6.3, of the i-th cell, the red cell in Fig. 6.3. The current flowing out of the i-th Voronoi cell I_{ij} is calculated as $(V_i - V_j)G_{ij}$, where G_{ij} is the conductance between cells i and j. The resistance R_{ij} (reciprocal of G_{ij}) comprises of the total resistance between i-th and j-th Voronoi cells. Mathematically, $R_{ij} = (\rho_{grain} \times L_{ij}/W_{ij}) + R_{ij}^{GB}$, where ρ_{grain} is the sheet resistance of single crystalline graphene which depends on the mobility and carrier density. L_{ij} is the distance between i-th and j-th cells and W_{ij} is the length of the edge separating the two Voronoi cells. If the Voronoi cells i and j are on either sides of the GB, then R_{ij}^{GB} is the resistance of the GB segment, else it is zero.

On substituting $I_{ij} = (V_i - V_j) \times G_{ij}$ in Eqn. 6.1 and rearranging the terms, V_i can be written as

$$V_i = \frac{\sum_j V_j \times G_{ij}}{\sum_j G_{ij}}. \tag{6.2}$$

Then we set up an iterative loop, where we updated the voltages of each Voronoi cell based on the voltages of its neighbors from the last iteration as

$$V_i^{n+1} = \frac{\sum_j V_j^n \times G_{ij}}{\sum_j G_{ij}}. \tag{6.3}$$

A steady-state is reached when the maximum voltage change of all the cells between two consecutive iterations is less than $10^{-4}\%$. For most of the cases, it took about 5000 iterations to reach steady-state.

6.3 Results and Discussion

6.3.1 Resistivity for GBs with different roughness and correlation length

We focus here on the effect of structure of non-straight GBs on their resistivity, especially for the asymmetric GBs with large Θ_M; for demonstration, we used an asymmetric

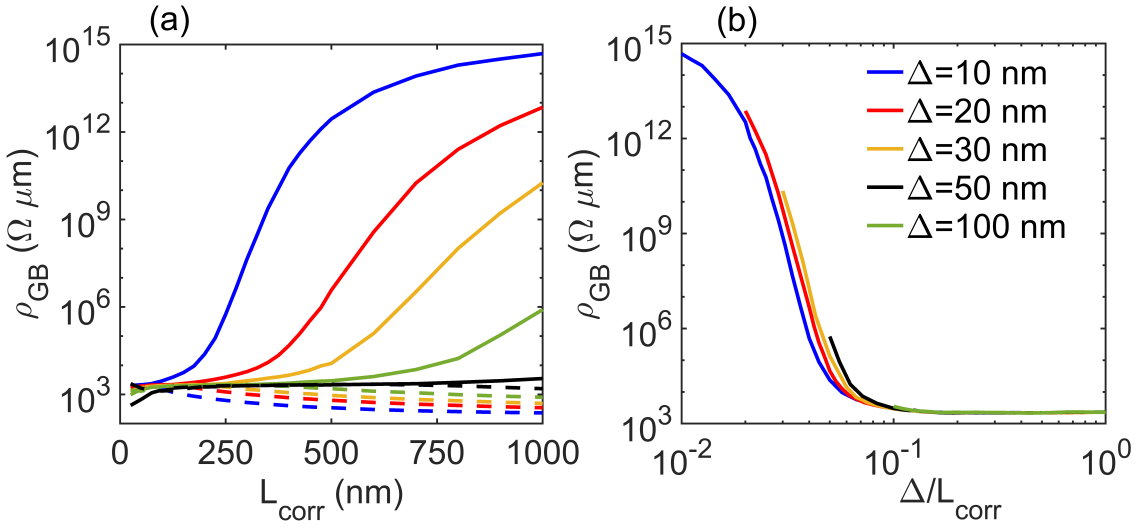

Figure 6.4: **(a)** shows the dependence of ρ_{GB} on the roughness and correlation length of non-straight GBs. The same data for ρ_{GB} is plotted against the average slope of the GB in **(b)**.

case of (x°,y°)=(0°,20°). We used roughness and correlation length to characterize the structure of extended GBs. In Fig. 6.4(a), we found that the resistivity is the least for GBs with the largest Δ and the smallest L_{corr} which is counter-intuitive because roughness and poor correlation lengths are often associated with negative effects. Since the conductivity of a non-straight GB depends on the probability of finding a symmetric segment, a more wavy GB, which is characterized by large roughness and small correlation length, exhibits the smallest resistivity, as we can see in the figure. Small correlation length and large roughness corresponds to a GB with steep effective slope. Fig. 6.4(b) shows the GB resistivity for the same set of correlation length and roughness but plotted against the slope of the GB, Δ/L_{corr}. We found that GB resistivity is inversely proportional to the slope with ρ_{GB} showing an universal trend for all correlation lengths and roughness. It indicates that the average slope of a GB—described by Δ/L_{corr}—can be used as a quantifier for the GB resistivities. The resistivity of a symmetric, non-straight GB shows negligible dependence on roughness and correlation length, as shown by the dashed lines in Fig. 6.4(a).

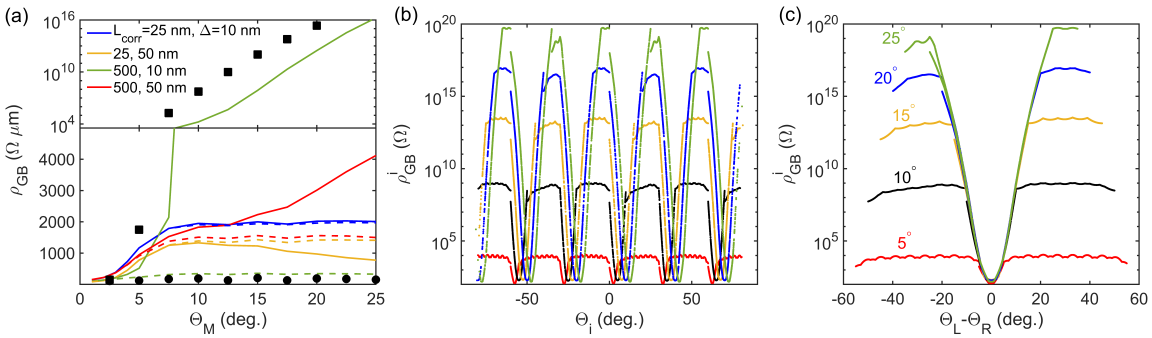

Figure 6.5: **(a)** shows the resistivity of non-straight line GBs vs. misorientation angle Θ_M for various correlation length and roughness. The solid and dashed lines represent the resitivities of asymmetric and symmetric GBs, respectively. **(b)** shows the resistivity of each GB segment ρ^i_{GB} vs. the angles (Θ_i) that each segment makes with a vertical reference axis for various Θ_M. Red, black, yellow, blue and green curves correspond to 5°, 10°, 15°, 20°, and 25°, respectively. Segments with Θ_i equal to $\Theta_M/2 \pm 30°$ divide the crystallographic angles of the grains symmetrically and will exhibit the smallest resistivity. This is illustrated in **(c)** where the resistivity of each segment is plotted against the relative difference between the crystallographic angles of each grain with Θ_i, given by $\Theta_L - \Theta_R$; the segments with the smallest $\mid \Theta_L - \Theta_R \mid$ has the least resistivity and as $\mid \Theta_L - \Theta_R \mid$ increases, ρ^i_{GB} increases exponentially.

Next, we go on to explore the effect of misorientation angles on resistivity of non-straight GBs. In Fig. 6.5(a), the solid lines represent the most asymmetric cases $(0°, \Theta_M)$ and dashed lines are for symmetric ones $(\Theta_M/2, \Theta_M/2)$. For asymmetric GBs, when the effective slope of the GB (Δ/L_{corr}) is large (blue and yellow solid lines), the GB resistivity varies between 10^2 to 10^4 Ω μm and is more or less independent of the misorientation angle, especially for $\Theta_M > 5°$. Our results show that the zig-zag nature of GBs makes them orders of magnitude more conductive than the straight line ones. An extended GB with small Δ and large L_{corr} would resemble a straight-line GB. We calculated the resistivity for GBs with Δ and L_{corr} equal to 10 and 500 nm, respectively, (green curves) for various misorientation angles to compare the results with those of the straight line GBs published in our previous work [249]. We found that the solid green curve shows a strong dependence on Θ_M and the resistivity values range from a few hundreds to 10^{20} Ω μm, similar to those of the black square markers, which show the resistivity vs. Θ_M for asymmetric, straight

line GBs. On the other hand, the green dashed line shows a similar trend as the resistivities of straight line GBs for symmetric case, which is shown here by black circular markers. For symmetric cases, the resistivities of uncorrelated boundaries with different roughness show slightly higher values than those of the straight line ones, but the resistivity values are still quite small, varying between 1000 to 2000 Ω μm. In short, due to the waviness of GBs, there always exists a few segments which provide a conductive path for the current to flow across a GB, and as a result, the resistivity of most experimentally-observed (non-straight) GBs exhibits negligible dependence on misorientation angle.

To identify the conductive segments in a non-straight GB, we plotted the resistivity of each segment ρ_{GB}^{i} against the angles Θ_i that each segment makes with a vertical reference axis for various Θ_M shown by different colors in Fig. 6.5(b)—red, black, yellow, blue and green curves correspond to Θ_M equal to 5°, 10°, 15°, 20°, and 25°, respectively. We found that only a few segments have resistivity as small as 10^2 Ω μm, whereas remaining segments are highly resistive. To see which segments are most conductive, we plotted ρ_{GB}^{i} vs. $\Theta_L - \Theta_R$ in Fig. 6.5(c). We found that the segments with $\Theta_L - \Theta_R$ equal to zero have the smallest resistivity; $\Theta_L - \Theta_R$ equal to zero corresponds to the segments which divide the crystallographic angles of the grains symmetrically. When $\mid \Theta_L - \Theta_R \mid$ increases, the resistivity of those segments also increases exponentially; consequently, we found that only those segments with $\mid \Theta_L - \Theta_R \mid < 5^\circ$ contributes to the overall conductance of the GB.

6.3.2 Spreading resistance

Lastly, we turn to the path of current near the GB and examine the effect of the large variation in resistivity along the GB on current flow. Fig. 6.6(a) shows the steady-state voltage profile in a 2.5 μm $\times$ 2.5 μm sample with an asymmetric GB at x=0. The crystal orientations of left and right grains are 0° and 20°, respectively. The conductance of the GB segments is qualitatively represented here by a color scheme shown on the right of the figure. The highly resistive segments are depicted by black lines, and the light-colored

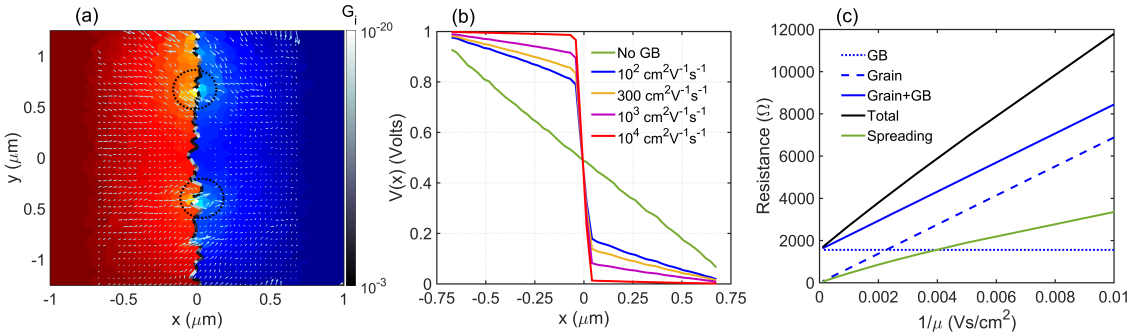

Figure 6.6: **(a)** shows the steady-state voltage profile between the two contacts in a 2.5 μm $\times$ 2.5 μm graphene sample with a GB at x=0. The resistivity of each GB segment is represented here by a color scheme on the right of the figure. The direction and magnitude of the current flowing through the sample is shown by the direction and length of the arrows, respectively. **(b)** shows the average voltage profile along the x-direction for various grain resistances ($\propto \mu^{-1}$). **(c)** shows the variation of the total and spreading resistance as a function of grain resistance.

segments are the conductive ones. We used a carrier density of 6×10^{12} cm^{-2} to calculate the GB and grain resistances. A mobility of 100 cm^2 V^{-1} s^{-1} is used here to compute the sheet resistance of graphene grains. For the contacts, a fixed voltage of 1V (shown by dark red) is applied in the region -1$<$ x $<$-0.75 μm, whereas the region on the right, 0.75$<$ x $<$1 μm, is grounded (shown by dark blue). The smooth transition in the voltage profile from red to blue near the conductive segments corroborates that majority current flows through a few narrow segments of a highly resistive GB. The current flow in the grains and across the GB is shown by arrows overlaid on this figure, where the magnitude and direction of the current flow is represented by the length and direction of the arrows, respectively. We can see here that the current starts bending near the GB and its magnitude increases around conductive GB segments, which are shown by the two dotted circles in the figure.

To determine potential drop along the sample length, we calculated an average voltage, shown by the blue line in fig. 6.6(b), in the x-direction, $V(x) = \frac{1}{L_y}\int V(x,y)dy$, where L_y is the width of the sample. We see that about 65% of the applied voltage drops at the GB. The green curve in fig. 6.6(b) represents voltage drop in a sample without GB, where the potential drops linearly along the sample, as expected. Since the conductance

of a single-crystalline graphene varies between a wide range depending on the impurities, defects and other fabrication parameters, we plotted V(x) along the sample for different grain resistance, R_{grain}, which we tuned by varying mobility between 10^2 to 10^4 cm^2 V^{-1} s^{-1}. We see that in a sample where the mobility is as high as 10^4 cm^2 V^{-1} s^{-1}, more than 95% of the voltage drops at the GB; in such samples one can approximate the resistance of the entire sample by the R_{GB} only.

The effect of current bending and traversing additional path in the grain to access the conductive channels of a highly resistive GB is, typically, represented by spreading resistance, R_{spread}, such that $R_{tot} = R_{grain} + R_{GB} + R_{spread}$. Fig. 6.6(b) shows the spreading resistance as a function of the grain resistance, which is proportional to the μ^{-1} as shown by the dashed blue line. The total resistance of the sample, which is calculated as the voltage difference between the two contacts divided by the total steady-state current passing through the GB, is shown by the black curve. We can see that R_{tot} is equal to $R_{GB} + R_{grain}$ (shown by the solid blue line) when the grains are highly conductive, that is μ=10^4 cm^2 V^{-1} s^{-1}. When the resistance of the grains ($\propto \mu^{-1}$) increases, the difference between the R_{tot} and $R_{GB} + R_{grain}$, which is the spreading resistance as shown by the green curve, also increases. In other words, we found that the current bends more to flow through the conductive GB segments in relatively more resistive grains. As a result, the current flow is non-uniform along the GB; the degree of non-uniformity is determined by the spreading resistance. We also found that the current flowing through a narrow conductive GB segment, qualitatively, resembles to a cylindrical current source in 3D [256]. Since graphene is two-dimensional, the voltage profile would approximately follow a circular solution of the form—$V(L) \propto I\rho_{sheet} \times \frac{1}{2} ln(\frac{L}{2l_{GB}})$ for $l_{GB} \ll L/2$. L is the distance between the two contacts and l_{GB} is the effective length of the conductive segment. We calculated an effective length of the conductive channel, $\frac{\Sigma_i G_i L_i}{\Sigma_i G_i}$, to be about 30 nm which is 1.2% of the total length of the GB.

6.4 Conclusions

Due to the zigzag nature of extended GBs, there are GB segments which divide the relative crystallographic angles between two grains symmetrically, which makes these segments highly conductive. The presence of these conductive segments destroys the correlation between the resistivity and misorientation angles which was reported in previous theoretical studies on straight-line GBs. The resistivity of non-straight GBs are found to be independent of misorientation angles and lie in an universal range of 10^2 to 10^4 Ω μm. It bridges the discrepancy found in experiments and previous theoretical reports. Since the probability of finding conductive segments is higher when Δ is large, we found that the resistivity is inversely proportional to the effective slope (Δ/L_{corr}) of the GB. As a result, extended GBs with large roughness and small correlation length exhibit the least resistivity. The steady-state voltage profile of a graphene sample with extended GB clearly shows that the current bends in the grains to flow through the few conductive segments which gives rise to a spreading resistance. We found that the spreading resistance scales with the grain resistance—the scaling factor is proportional to a "$ln\left(\sqrt{\frac{L}{2l_{GB}}}\right)$" term, which qualitatively resembles to the solution for current emanating from a cylindrical source in 3D. Beyond improving our understanding on electrical transport across graphene GBs, this study will be crucial for designing future nanoelectronic circuits.

CHAPTER 7

APPENDIX

7.1 First-Principles Phonon Dispersion Calculation of Monolayer WSe_2

The full phonon dispersion of monolayer WSe_2 is calculated with the PHonon code as distributed with the Quantum-Espresso package [97]. The unit cell structure is first relaxed using the Broyden-Fletcher-Goldfarb-Shanno algorithm [257, 258] until the forces acting on each atom are less than 2.6×10^{-5} eV/Å. The equilibrium lattice parameters - in order of lattice constant a, Se-Se distance z, and W-Se distance r of the energetically relaxed structure are a=3.321 Å, z=3.348 Å, and r=2.545 Å. To ensure that interplanar van der Waals interactions between adjacent trilayer planes are neglected, a separation distance of about 10 Åis imposed along the z-direction. In the relaxation calculation and the self-consistent field total energy calculation, we use a plane wave kinetic energy cutoff of 100 Ry, a shifted Monkhorst-Pack grid scheme of $16\times16\times1$, and a convergence threshold for self-consistency of 10^{-14}. A GGA functional with Perdew-Burke-Ernzenhof parameterization and Vanderbilt type ultrasoft pseudopotential [259] is used for both W and Se. In calculating interatomic force constants from Density Functional Perturbation Theory [260], a $8\times16\times1$ q-mesh is used with a convergence threshold of 10^{-14}. After the phonon calculation, the dynamical matrices are inverse Fourier Transformed to obtain the interatomic force constant matrices (IFCs) in real space. Finally, we sample the 1st brillouin zone for phonon frequencies using a dense grid of 25,208 q-points. Using this dense grid we then calculate the pDOS including homogeneous collision broadening through internal mechanisms $\Gamma_{j,int}$, with a Lorentzian broadening function $D_{WSe_2}(\omega) = \sum_{\vec{q},b} \frac{\chi}{\pi[\chi^2+[E-\hbar\omega(\vec{q},b)]^2]}$, where χ is an energetic smearing term equal to $\Gamma_{j,int}[\omega_b(\vec{q})]$, E is a discretized energy space

spanning [0,100] meV, and ω_b is the phonon dispersion per branch b. The resulting phonon dispersion, pDOS, and equilibrium structure are shown in Figure 7.1.

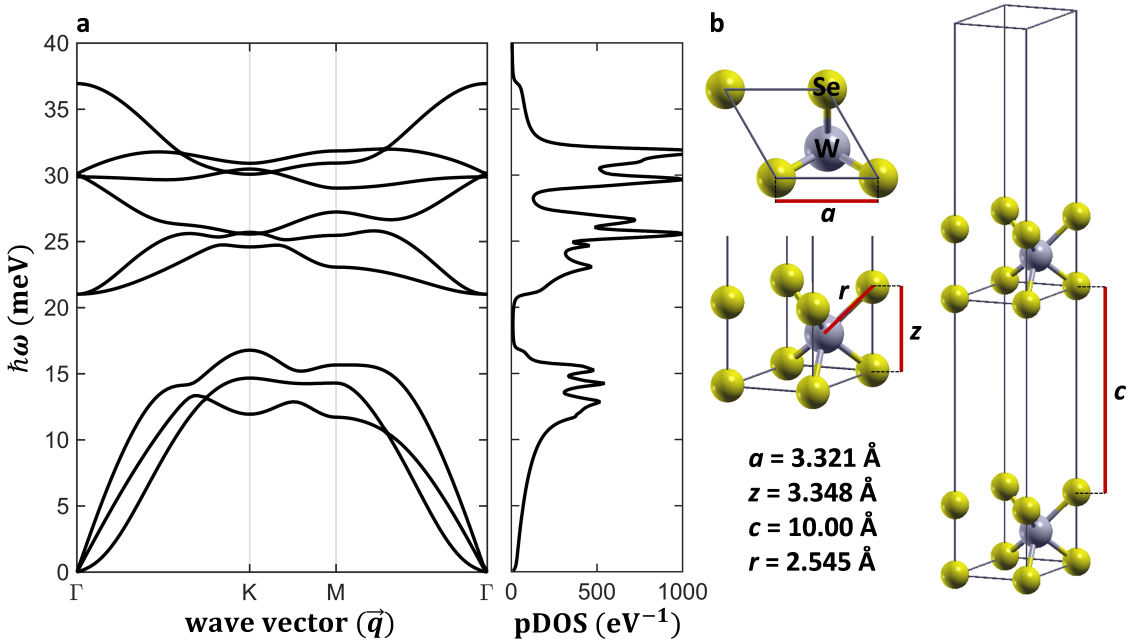

Figure 7.1: **(a)**The full phonon dispersion (left) and pDOS (right) for monolayer WSe_2 as calculated from first-principles DFPT. An energetic smearing of 0.3 meV is used in calculating the pDOS. **(b)** Schematics of the unit cell structure of monolayer WSe_2 marking lattice constant a, chalcogen-to-chalcogen (Se-Se) distance z, W-Se distance r, and vacuum spacing c

7.2 Multilayer Thermal Boundary Conductance Model (Theory)

Phonon transport across a 2D-3D van der Waals (vdW) interface is carried by out-of-plane flexural (ZA) branch phonons, which are interacting with the substrate through the vdW bond and hopping across the interface [43]. The rate at which ZA phonons hop across the interface is given by a substrate scattering rate Γ_{sub} [261]. When a ZA phonon hops across the 2D-3D interface it depopulates the population of ZA phonons in the monolayer, which can then only be replenished by internal scattering mechanisms Γ_{int}. Therefore, the picture of thermal boundary conductance between a vdW (2D) material and its substrate involves both an external (or Kapitza) resistance [43, 262] determined by the rate at which

ZA phonons transfer into the substrate Γ_{sub} and an internal resistance [262, 263] determined by the rate at which ZA phonons are replenished by Γ_{int}. The thermal boundary conductance can then be written as a sum of series conductances resulting in

$$G = \int \hbar\omega D_{WSe_2}(\omega)\frac{dN_0(T)}{dT}\frac{\Gamma_{sub}(\omega)\Gamma_{int}(\omega)}{\Gamma_{sub}(\omega)+\Gamma_{int}(\omega)}d\omega \tag{7.1}$$

In the above, the first three terms of the integrand are the modal heat capacity $C_{WSe_2}(\omega) = \hbar\omega D_{WSe_2}(\omega)(dN_0(T))/dT$, where N_0 is the Bose-Einstein distribution function $N_0(T) = [exp(\hbar\omega/(k_BT)) - 1]^{-1}$. The last term in the integrand represents the summation of two series resistances that are determined by their respective scattering rates Γ_{int} and Γ_{sub}, and can be written more compactly as $[\Gamma_{sub}^{-1}(\omega) + \Gamma_{int}^{-1}(\omega)]^{-1}$. We can then write the spectral conductance as $G(\omega) = C_{WSe_2}(\Omega)[\Gamma_{sub}^{-1}(\omega) + \Gamma_{int}^{-1}(\omega)]^{-1}$. Therefore, the effective thermal boundary conductance is determined by the slowest scattering rate, Γ_{int} or Γ_{sub}.

The rate at which ZA phonons transfer from a (single) monolayer to substrate, termed by the substrate scattering rate Γ_{sub}, is given by [264]:

$$\Gamma_{sub}(\omega) = \frac{\pi}{2}\frac{D_{sub}(\omega)}{M_{ML}M_{sub}}\frac{K_a^2}{\omega^2} \tag{7.2}$$

In the above, $D_{ML}(\omega)$ is the substrate phonon Density of States (pDOS), K_a is the van der Waals spring coupling constant, ω is the phonon frequency, M_{ML} is the mass of the atoms of the monolayer in contact with the substrate, and M_{sub} is the mass of the atoms at the surface of the substrate. However, in this work we have few-layer WSe_2 flake of thickness H of about 7 nm. Taking the thickness of the trilayer (Se-W-Se) plus the thickness of the vdW gap between adjacent planes to be about 6.45 Å[265], we have 11 layers of WSe_2. We can treat this few-layer WSe_2 as an N-layer monolayer and extend the above following formulations by Ong [266] for multilayer thermal boundary resistance. The resulting sub-

strate scattering rate for phonon transport between a few-layer vdW (stacked 2D) system to a (3D) substrate can be written as,

$$\Gamma^{FL}_{j,sub}(\omega) = \frac{\pi}{2}\left[\frac{M_{Se}}{K_{sub}} + \frac{((j-1)M_{WSe_2})}{K_z}\right]^{-2}\frac{M_{Se}}{M_{sub}}\frac{D_{sub}(\omega)}{\omega^2} \tag{7.3}$$

where K_{sub} is the vdW spring coupling constant between the bottom-most monolayer and the substrate, K_z is the interlayer spring coupling constant [267], M_{Se} is the mass of the chalcogen atom selenium, M_{WSe_2} is the unit cell mass of WSe_2, and j represents the j-th layer in the few-layer stack. While K_{sub} is taken as an input parameter, K_z (per unit area) is reported to be 8.63×10^{19} N m^{-3} in WSe_2 [267]. This value is then multiplied by the unit cell area of WSe_2 to obtain the interplanar spring coupling constant K_z=8.24 N m^{-1} which is the value of K_z used in all our calculations.

The rate at which ZA phonons are repopulated by internal mechanisms Γ_{int} is determined by the summation of three-phonon anharmonic processes Γ_{anh} [268], phonon-boundary scattering [178] Γ_{bound}, and, when encapsulated, phonon interactions with an encapsulating layer $\Gamma_{j,enc}$—precisely, $\Gamma_{j,int} = \Gamma_{anh} + \Gamma_{bound} + \Gamma_{j,enc}$. Three-phonon anharmonic scattering is taken as the summation of Normal (non-resistive) and Umklapp (resistive) scattering mechanisms $\Gamma_{anh}(\omega) = \Gamma_N(\omega) + \Gamma_U(\omega)$, where

$$\Gamma_N(\omega) = \frac{\gamma^2(S_{MX}h_{MX})^\alpha}{m_{MX}v_{ac}^\beta}\omega^{a_N}T\exp(-\Theta_D/3T), \tag{7.4}$$

$$\Gamma_U(\omega) = \frac{\hbar\gamma^2}{m_{MX}v_{ac}^2\Theta_D}\omega^2 T\exp(-\Theta_D/3T). \tag{7.5}$$

In either Γ_N or Γ_U, γ is the Gruneisen parameter, S_{MX} is the unit cell surface area, h_{MX} is the interlayer spacing, m_{MX} is the atomic mass, v_{ac} is the acoustic sound velocity of the monolayer, Θ_D is the Debye Temperature, and T is temperature. The α, β, and a_N terms in Γ_N correspond to fitted empirical constants. For phonon-boundary scattering we assume a purely diffuse scattering model in which $\Gamma_{bound}(\omega) = v_g/H$, where H is the thickness of

the few-layer vdW structure. We can use a purely diffuse model because both the substrate and encapsulating layer are amorphous. It has been shown that, regardless of boundary roughness, phonon collisions at a boundary with an amorphous material results in mainly diffusive scattering [269].

Phonon interactions rate with an encapsulating layer in a few-layer vdW structure can be written similarly to $\Gamma^{FL}_{j,sub}(\omega)$ as

$$\Gamma^{FL}_{j,sub}(\omega) = \frac{\pi}{2}\left[\frac{M_{Se}}{K_{enc}} + \frac{((NL-j)M_{WSe_2})}{K_z}\right]^{-2}\frac{M_{Se}}{\omega^2}\left[\frac{(D_{enc}(\omega))}{M_{enc}} + \frac{(D_{WSe_2}(\omega))}{M_{Se}}\right], \tag{7.6}$$

where NL represents the total number of vdW layers, M_{enc} is the mass of the surface atoms of the superstrate, K_{enc} is the spring coupling constant between the topmost WSe_2 layer and the encapsulating layer, and $D_{enc}(\omega)$ is the pDOS of the encapsulating layer. For simplicity, we assume here that the spring coupling constant between the topmost layer and the encapsulating layer K_{enc} is equal to that between the bottommost layer and the substrate K_{sub}. Lastly, the thermal boundary conductance contribution from each layer j in the multilayer (or few-layer) stack is then calculated, analogously to a single layer, from

$$G_j(T) = \int \hbar\omega D_{WSe_2}(\omega)\frac{dN_0(T)}{dT}\frac{\Gamma_{j,sub}(\omega)\Gamma_{j,int}(\omega)}{\Gamma_{j,sub}(\omega)+\Gamma_{j,int}(\omega)}d\omega. \tag{7.7}$$

Each layer is coupled to the substrate acting as a system of parallel resistive elements. Since Raman thermometry measures a single average temperature based on the total heat dissipation, we consider a uniform temperature across the multilayer stack to compute an effective conductance. Thus, the total conductance (TBC) of this network of parallel resistors can then be obtained by summing over the conductance of each layer from TBC=$\sum_j G_j(T)$. The thermal boundary resistance per layer (TBR_j) values correspond precisely to TBR_j=G_j^{-1} at room-temperature.

7.3 Integrals for phonon-electron rates

7.3.1 Acoustic phonon-electron rate integrals

7.3.1.1 First integral

$$
\begin{aligned}
I_1 &= \int_{k_{n1}}\int_{k_{n2}} [exp\left(-\frac{E_{nk}-E_F}{k_BT}\right)\delta[k_{n1}-k'_n]dk_{n1}dk_{n2} \\
&= \int_{k_{n1}}\int_{k_{n2}} exp\left(\frac{E_F}{k_BT}\right)exp(-\frac{\hbar^2}{2m^\star k_BT}(k_{n1}^2+k_{n2}^2))\delta[k_{n1}-k'_n]dk_{n1}dk_{n2} \\
&= exp\left(\frac{E_F}{k_BT}\right)\int_{k_{n1}} exp\left(-\frac{\hbar^2k_{n1}^2}{2m^\star k_BT}\right)\delta[k_{n1}-k'_n]dk_{n1}\int_{k_{n2}} exp\left(-\frac{\hbar^2k_{n2}^2}{2m^\star k_BT}\right)dk_{n2}.
\end{aligned}
$$

The integral with respect to dk_{n2} is a Gaussian integral of zeroth order which yields $\sqrt{\frac{2\pi m^\star k_BT}{\hbar^2}}$. Using the integral property of Dirac-delta function, we evaluate the integral with respect to dk_{n2}. Thus, I_1 simplifies to

$$
\begin{aligned}
I_1 &= exp\left(\frac{E_F}{k_BT}\right)exp\left(-\frac{\hbar^2k_n'^2}{2m^\star k_BT}\right)\sqrt{\frac{2\pi m^\star k_BT}{\hbar^2}} \\
&= exp\left(\frac{E_F}{k_BT}\right)\sqrt{\frac{2\pi m^\star k_BT}{\hbar^2}}exp\left(-\frac{\hbar^2q^2}{8m^\star k_BT}-\frac{m^\star v_s^2}{2k_BT}-\frac{\hbar v_sq}{2k_BT}\right).
\end{aligned}
\tag{7.8}
$$

7.3.1.2 Second integral

$$
\begin{aligned}
I_2 &= \int_{k_{n1}}\int_{k_{n2}} [exp\left(-\frac{E_{nk+q}-E_F}{k_BT}\right)\delta[k_{n1}-k'_n]dk_{n1}dk_{n2} \\
&= \int_{k_{n1}}\int_{k_{n2}} exp\left(\frac{E_F}{k_BT}\right)exp\left(-\frac{\hbar^2}{2m^\star k_BT}(k_n^2+q^2+k_n\cdot q)\right)\delta[k_{n1}-k'_n]dk_{n1}dk_{n2} \\
&= \sqrt{\frac{2\pi m^\star k_BT}{\hbar^2}}exp\left(\frac{E_F}{k_BT}\right)exp\left(-\frac{\hbar^2q^2}{2m^\star k_BT}\right)\int_{k_{n1}} exp\left(-\frac{\hbar^2k_{n1}^2}{2m^\star k_BT}\right)exp\left(-\frac{2\hbar^2k_{n1}q}{2m^\star k_BT}\right) \\
&\quad \delta[k_{n1}-k'_n]dk_{n1}.
\end{aligned}
$$

$$
\begin{aligned}
I_2 &= exp\left(\frac{E_F}{k_BT}\right)\sqrt{\frac{2\pi m^\star k_BT}{\hbar^2}}exp\left(-\frac{\hbar^2q^2}{8m^\star k_BT}-\frac{m^\star v_s^2}{2k_BT}-\frac{\hbar v_sq}{2k_BT}\right)exp\left(-\frac{\hbar^2q^2}{2m^\star k_BT}\right)\times \\
&\quad exp\left(-\frac{\hbar^2q^2}{2m^\star k_BT}\right)exp\left[-\frac{\hbar^2q}{m^\star k_BT}\left(-\frac{q}{2}-\frac{m^\star v_s}{\hbar}\right)\right].
\end{aligned}
\tag{7.9}
$$

By combining Eqn. 7.8 and Eqn. 7.9, we can write the transition rates as

$$\frac{1}{\tau_{q\nu}^{ep}} = -\frac{m^\star D_a^2 q}{4\pi\hbar^2\rho\omega_{q\nu}} \sum_n exp\left(\frac{E_F}{k_BT}\right)\sqrt{\frac{2\pi m^\star k_BT}{\hbar^2}} exp\left(-\frac{\hbar^2q^2}{8m^\star k_BT} - \frac{m^\star v_s^2}{2k_BT} - \frac{\hbar v_s q}{2k_BT}\right) \times \left[1 - exp\left(\frac{\hbar v_s q}{k_BT}\right)\right].$$

$$\frac{1}{\tau_{q\nu}^{ep}} = \frac{m^{\star 3/2} D_a^2 (k_BT)^{1/2}}{(2\pi)^{1/2} 2\hbar^3 \rho v_s} \sum_n exp\left(\frac{E_F}{k_BT}\right) exp\left(-\frac{\hbar^2q^2}{8m^\star k_BT} - \frac{m^\star v_s^2}{2k_BT} - \frac{\hbar v_s q}{2k_BT}\right)\left[exp\left(\frac{\hbar v_s q}{k_BT}\right) - 1\right]. \tag{7.10}$$

7.3.2 Phonon-electron rate for optical phonons

Following the same procedure as the acoustic case, we can write the rate of optical phonon-electron transition as

$$\frac{1}{\tau_{q\nu}^{ep}} = -\frac{m^\star D_o^2}{4\pi\hbar^2\rho\omega_o q}\int_k d^2k(f_{nk} - f_{nk+q})\delta\left(k_n cos\theta + \frac{q}{2} + \frac{m^\star\omega_o}{\hbar q}\right). \tag{7.11}$$

We can again split this integral into two integrals, and solve them separately.

7.3.2.1 First integral

The first integral is the same as the first integral in acoustic case (Eqn. 7.8) with $v_s q$ replaced by ω_o.

$$I_1 = exp\left(\frac{E_F}{k_BT}\right)\sqrt{\frac{2\pi m^\star k_BT}{\hbar^2}} exp\left(-\frac{\hbar^2q^2}{8m^\star k_BT} - \frac{m^\star\omega_o^2}{2k_BTq^2} - \frac{\hbar\omega_o}{2k_BT}\right). \tag{7.12}$$

7.3.2.2 Second integral

The second integral also takes a similar form as in the acoustic case in Eqn.3.11 except $v_s q$ replaced by ω_o.

$$I_1 = exp\left(\frac{E_F}{k_BT}\right)\sqrt{\frac{2\pi m^\star k_BT}{\hbar^2}} exp\left(-\frac{\hbar^2q^2}{8m^\star k_BT} - \frac{m^\star\omega_o^2}{2k_BTq^2} - \frac{\hbar\omega_o}{2k_BT}\right) exp\left(\frac{\hbar\omega_o}{k_BT}\right). \tag{7.13}$$

By combining Eqn. 7.12 and Eqn. 7.13 along with the prefactor in Eqn. 7.11, we can write the optical phonon-electron scattering rate as—

$$\frac{1}{\tau_{q\nu}^{ep}} = \frac{m^{\star 3/2} D_o^2 (k_B T)^{1/2}}{(2\pi)^{1/2} 2\hbar^3 \rho \omega_o q} exp\left(\frac{E_F}{k_B T}\right) exp\left(-\frac{\hbar^2 q^2}{8m^\star k_B T} - \frac{m^\star \omega_o^2}{2k_B T q^2} - \frac{\hbar\omega_o}{2k_B T}\right)\left[exp\left(\frac{\hbar\omega_o}{k_B T}\right) - 1\right]. \tag{7.14}$$

In the limit of $q \to 0$, this gets further simplified

$$\frac{1}{\tau_{q\nu}^{ep}} = \frac{m^{\star 3/2} D_o^2 (k_B T)^{1/2}}{(2\pi)^{1/2} 2\hbar^3 \rho \omega_o q} exp\left(\frac{E_F}{k_B T}\right) exp\left(-\frac{m^\star \omega_o^2}{2k_B T q^2}\right) exp\left(-\frac{\hbar\omega_o}{2k_B T}\right)\left[exp\left(\frac{\hbar\omega_o}{k_B T}\right) - 1\right].$$

Assuming $\frac{\hbar\omega_o}{2k_B T}$ to be x, we can write

$$exp\left(-\frac{\hbar\omega_o}{2k_B T}\right)\left[exp\left(\frac{\hbar\omega_o}{k_B T}\right) - 1\right] = e^{-x}(e^{2x} - 1) = sinh\left(\frac{\hbar\omega_o}{2k_B T}\right).$$

We again combine few terms in the expression for optical phonon-electron transition rate to express it in terms of 2D carrier density

$$\boxed{\frac{1}{\tau_{q\nu}^{ep}} = \left(\frac{2\pi m^\star}{k_B T}\right)^{1/2} \frac{D_o^2}{\rho\omega_o} exp\left(-\frac{m^\star \omega_o^2}{2k_B T q^2}\right)\left(\frac{1}{\hbar q}\right) n(E) sinh\left(\frac{\hbar\omega_o}{2k_B T}\right)}. \tag{7.15}$$

7.4 Density Functional Theory calculations of the electronic band-structure of Graphene and MoS_2

For graphene, we used a scalar relativistic, norm-conserving pseudopotential (NCPP) which implements a direct-fit Von Barth-Car method with a Perdew-Zunger local density approximation (LDA) exchange-correlation functional [270]. For MoS_2, we used a non-relativistic NCPP for Mo and a scalar relativistic NCPP for S. Both potentials employed a Martins-Troullier method with a Perdew-Wang LDA exchange correlation [271]. The lattice constants are a = 2.459 Å for graphene and a = 3.125 Å, z = 3.11 Å for MoS_2, where z is the distance between chalcogen atoms. To ensure that interplanar interactions

are neglected, the repeating images of the monolayers are seperated by a 20 Å vacuum. The cutoff energy for plane waves was 120 Ry for graphene and 140 Ry for MoS_2. We used a convergence threshold of 10^{-15} on a Monkhorst-Pack grid sizes of $8\times8\times1$ for graphene and $6\times6\times4$ for MoS_2 for the initial total energy calculation and then performed a band-structure calculation on a dense grid of 25,208 k-points (wavevectors) with a convergence threshold of 10^{-12}. We used the central difference method to obtain the electron velocities per band which, in turn, are subsequently used in calculating the electronic density of states (DOS) and other transport properties including interfacial transmission and resistance of the interface.

7.5 Ballistic resistance of graphene-graphene interface

We derive an analytical expression for the ballistic resistance across graphene GBs and compare it with the numerically computed values of ballistic resistance at different carrier concentrations. We define ballistic resistance as the resistance between two perfectly-matched grains, that is when misorientation angle (Θ_M) is 0°. In the diffusive limit (Ohmic regime) when the dimension of the conductor is large compared to the carrier mean free path, the conductance varies inversely with length. One would expect the conductance to become infinite when the conductor length tends to zero. However, it has been experimentally found in both metals and semiconductors [272] that the measured conductance converge to a finite value called ballistic conductance. The regime where we see this limiting behavior is called ballistic regime. In this regime, characterized by an absence of scattering, the conductor has no resistance–the ballistic resistance is not the resistance of the conductor but the contact resistance [227].

With a careful treatment of the voltage across the GB, as done in a 4-probe measurement and analogous to the corrections made to the temperature gradient for phonon transmission [225], one could remove the ballistic contact resistance and show that the resistance across an idealized perfectly-matched GB is zero. In our calculations, the GB resistance at any

given mismatch angle includes the ballistic resistance, which varies with the carrier concentration. So, while comparing the 4-probe experimental measurements of GB resistance for a given mismatch angle with our results, as shown in Figure 5.7, we subtract the ballistic resistance from the calculated GB resistance.

The ballistic conductance for 1D conductor is given by the expression $G_{ball,1D} = 2e^2/h$, where e is the charge of the carrier and h is Planck's constant. A 2D conductor of width W could be thought of as a number of parallel 1D conductors, and thus, the conductance of the 2D conductor is the sum of the conductances of all the 1D conductors. The number of such 1D conductors that would be equivalent to the 2D conductor of width W is called 2D channel number, M_{2D}. Using the expression of ballistic conductance for 1D conductor, we write the ballistic conductance for a 2D conductor as

$$G_{ball,2D} = G_{ball,1D} \times M_{2D}(E_F) \tag{7.16}$$

The channel number at any energy (E) for a given width of the ribbon is calculated as [100]

$$M(E) = W\frac{h}{4}<v_x(E)>D_{2D}(E) \tag{7.17}$$

where $<v_x(E)>$ is calculated by 2D averaging of velocity of all the modes, $<v_x(E)> = \frac{2}{\pi}v_F$. v_F is the Fermi velocity ($\approx 10^6$ ms^{-1}), which is computed from the slope of the bandstructure (E-k relationship) around Dirac point. $D_{2D}(E)$ is the 2D density of states.

The dispersion of graphene around the Dirac point is approximated by the relation $E(\vec{k}) = \hbar v_F \mid \vec{k} \mid$, where $\hbar$ is the reduced Planck's constant. The general expression for calculating 2D density of states is

$$D_{2D}(\vec{k}) = \frac{1}{(2\pi)^2}\frac{2\pi \mid \vec{k} \mid}{\nabla_k E(\vec{k})}g_s g_v \tag{7.18}$$

where g_s and g_v are constants related to the spin of electron and valley degeneracy respectively. For graphene g_v=2 and g_s=2 for electrons. $\nabla_k E(\vec{k})$ is the gradient of energy

dispersion with respect to the wavevector and around the Dirac point it can be approximated by $\hbar v_F$. Thus for graphene,

$$D_{2D}(E) = \frac{2}{\pi \hbar^2 v_F^2} \mid E \mid \tag{7.19}$$

In general, 2D carrier concentration is given as

$$n_{2D}(E_F) = \int_0^\infty f_0(E) D_{2D}(E) dE \tag{7.20}$$

where $f_0(E)$ is the equilibrium Fermi-Dirac distribution function, $f_0(E) = [1+exp(\frac{E-E_F}{K_B T})]^{-1}$. As graphene is degenerate, so Eqn. 7.20 can be approximated by

$$n_{2D}(E_F) = \int_0^{E_F} D_{2D}(E) dE = \int_0^{E_F} \frac{2}{\pi \hbar^2 v_F^2} E dE = \frac{E_F^2}{\pi \hbar^2 v_F^2} \tag{7.21}$$

Using the expressions for density of states and 2D-averaged velocity, channel number in Eqn. 7.17 for graphene can be written as

$$M_{2D}(E_F) = \frac{2}{\pi} \frac{E_F}{\hbar v_F} W \tag{7.22}$$

Replacing the expression for channel number obtained from Eqn. 7.22 in Eqn. 7.16, we can calculate ballistic conductance in graphene as

$$\frac{G_{ball,2D}}{W} = \frac{8q^2}{\hbar^2 v_F} E_F \tag{7.23}$$

From Eqn. 7.21 and Eqn. 7.23, ballistic conductance in graphene can be expressed in terms of carrier concentration as

$$\frac{G_{ball,2D}}{W} = \frac{4q^2}{h} \sqrt{\frac{n_{2D}}{\pi}} \tag{7.24}$$

Thus the ballistic resistance R_{ball} in graphene, which is the reciprocal of $G_{ball,2D}$, is inversely proportional to the square root of carrier concentration. On using the values of the

constants in Eqn. 7.24 and intrinsic carrier concentration of 8×10^{10} cm^{-2}, the analytical value of R_{ball} in graphene is about 405 Ω μm.

We compare these analytically calculated values of ballistic resistance for different carrier concentrations with our numerically calculated values as shown in Figure 7.2(b). At intrinsic carrier concentration ($n_0 = 8 \times 10^{10}$ cm^{-2}), the numerically calculated ballistic resistance is 424 Ω μm, which compares quite well with the analytical value of 405 Ω μm. In Figure 7.2(a) we can see that transmission coefficient $\Gamma(E)$ is 1 for the entire energy range, showing perfect transmission for 0° mismatch (perfectly-matched grains). The curve encompassing the blue area in the figure is the Fermi window function, which is defined as the derivative of Fermi-Dirac distribution function with respect to energy, for intrinsic carrier concentration that is when the Fermi level E_F is around the Dirac point and the electron concentration is equal to the hole concentration. Eqn. 5.4 shows that the grain boundary resistance is a function of transmission coefficient, Fermi window function, velocity (proportional to Fermi velocity in graphene, which is a constant) and density of states. When the carrier (electron) concentration increases the Fermi level goes inside the conduction band and as a result Fermi window function, which is symmetric about the Fermi level, also shifts accordingly as shown in Figure 7.2(a). The integral of the product of Fermi window, transmission coefficient and velocity with respect to the energy is the same for all carrier concentrations but it is due to the 2D density of states, which is independent of the Fermi level, in the integral of grain boundary resistance that causes the difference in R_{GB} when plotted against carrier concentration as shown in Figure 7.2(b).

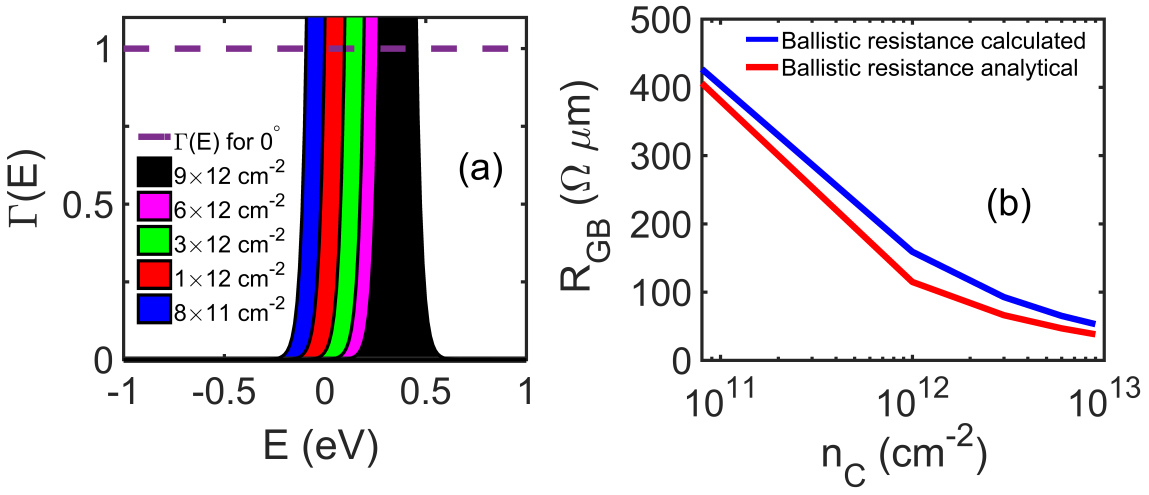

Figure 7.2: **(a)** shows perfect transmission for 0° mismatch angle between two graphene grains. The curves outlining the area in different colors represent the Fermi window function $(-df/dE)$, which is symmetric about E_F, for different carrier concentrations. **(b)** shows comparison between numerically and analytically calculated values of GB resistance (R_{GB}) with carrier concentration. R_{GB} is inversely proportional to the square root of the carrier concentration.

BIBLIOGRAPHY

[1] M. Mitchell Waldrop. The chips are down for moore's law. *Nature*, 530(7589):144–147, 2016.

[2] Kendal W. Clark, X.-G. Zhang, Ivan V. Vlassiouk, Guowei He, Randall M. Feenstra, and An-Ping Li. Spatially resolved mapping of electrical conductivity across individual domain (grain) boundaries in graphene. *ACS Nano*, 7:7956–7966, 2013.

[3] Vidya Kochat, Chandra Sekhar Tiwary, Tathagata Biswas, Gopalakrishnan Ramalingam, Kimberly Hsieh, Kamanio Chattopadhyay, Srinivasan Raghavan, Manish Jain, and Arindam Ghosh. Magnitude and origin of electrical noise at individual grain boundaries in graphene. *Nano Lett.*, 16:562–567, 2016.

[4] Qingkai Yu, Luis A. Jauregui, Wei Wu, Robert Colby, Jifa Tian, Zhihua Su, Helin Cao, Zhihong Liu, Deepak Pandey, Dongguang Wei, Ting Fung Chung, Peng Peng, Nathan P. Guisinger, Eric A. Stach, Jiming Bao, Shin-Shem Pei, and Yong P. Chen. Control and characterization of individual grains and grain boundaries in graphene grown by chemical vapour deposition. *Nat. Mater.*, 10:443–449, 2011.

[5] Luis A. Jauregui, Helin Cao, Wei Wu, Qingkai Yu, and Yong P. Chen. Electronic properties of grains and grain boundaries in graphene grown by chemical vapor deposition. *Sol. State Commun.*, 151:1100 – 1104, 2011.

[6] Adam W. Tsen, Lola Brown, Mark P. Levendorf, Fereshte Ghahari, Pinshane Y. Huang, Robin W. Havener, Carlos S. Ruiz-Vargas, David A. Muller, Philip Kim, and Jiwoong Park. Tailoring electrical transport across grain boundaries in polycrystalline graphene. *Science*, 336:1143–1146, 2012.

[7] Kyle L. Grosse, Vincent E. Dorgan, David Estrada, Joshua D. Wood, Ivan Vlassiouk, Gyula Eres, Joseph W. Lyding, William P. King, and Eric Pop. Direct observation of resistive heating at graphene wrinkles and grain boundaries. *Appl. Phys. Lett.*, 105(14):143109, 2014.

[8] Pinshane Y. Huang, Carlos S. Ruiz-Vargas, Arend M. van der Zande, William S. Whitney, Mark P. Levendorf, Joshua W. Kevek, Shivank Garg, Jonathan S. Alden, Caleb J. Hustedt, Ye Zhu, Jiwoong Park, Paul L. McEuen, and David A. Muller. Grains and grain boundaries in single-layer graphene atomic patchwork quilts. *Nature*, 469(7330):389–392, 2011.

[9] Poya Yasaei, Bijandra Kumar, Reza Hantehzadeh, Morteza Kayyalha, Artem Baskin, Nikita Repnin, Canhui Wang, Robert F. Klie, Yong P. Chen, Petr Krl, and Amin Salehi-Khojin. Chemical sensing with switchable transport channels in graphene grain boundaries. *Nat. Commun.*, 5:4911–, 2014.

[10] Ivan Vlassiouk, Sergei Smirnov, Ilia Ivanov, Pasquale F Fulvio, Sheng Dai, Harry Meyer, Miaofang Chi, Dale Hensley, Panos Datskos, and Nickolay V Lavrik. Electrical and thermal conductivity of low temperature cvd graphene: the effect of disorder. *Nanotechnology*, 22:275716, 2011.

[11] Katsunori Yagi, Ayaka Yamada, Kenjiro Hayashi, Naoki Harada, Shintaro Sato, and Naoki Yokoyama. Dependence of field-effect mobility of graphene grown by thermal chemical vapor deposition on its grain size. *Japanese J. Appl. Phys.*, 52:110106, 2013.

[12] Dinh Loc Duong, Gang Hee Han, Seung Mi Lee, Fethullah Gunes, Eun Sung Kim, Sung Tae Kim, Heetae Kim, Quang Huy Ta, Kang Pyo So, Seok Jun Yoon, Seung Jin Chae, Young Woo Jo, Min Ho Park, Sang Hoon Chae, Seong Chu Lim, Jae Young Choi, and Young Hee Lee. Probing graphene grain boundaries with optical microscopy. *Nature*, 490(7419):235–239, 2012.

[13] Meng Yang, Shinichirou Sasaki, Masato Ohnishi, Ken Suzuki, and Hideo Miura. Electronic properties and strain sensitivity of cvd-grown graphene with acetylene. *Japanese J. Appl. Phys.*, 55:04EP05, 2016.

[14] Dongmok Lee, Gi Duk Kwon, Jung Ho Kim, Eric Moyen, Young Hee Lee, Seunghyun Baik, and Didier Pribat. Significant enhancement of the electrical transport properties of graphene films by controlling the surface roughness of Cu foils before and during chemical vapor deposition. *Nanoscale*, 6:12943–12951, 2014.

[15] R. Peierls. Quelques proprits typiques des corps solides. *Annales de l'institut Henri Poincaré*, 5(3):177–222, 1935.

[16] K. S. Novoselov, A. K. Geim, S. V. Morozov, D. Jiang, Y. Zhang, S. V. Dubonos, I. V. Grigorieva, and A. A. Firsov. Electric field effect in atomically thin carbon films. *Science*, 306(5696):666–669, 2004.

[17] K. S. Novoselov, D. Jiang, F. Schedin, T. J. Booth, V. V. Khotkevich, S. V. Morozov, and A. K. Geim. Two-dimensional atomic crystals. *Proc. Natl. Acad. Sci. U.S.A.*, 102(30):10451–10453, 2005.

[18] K. S. Novoselov, A. K. Geim, S. V. Morozov, D. Jiang, M. I. Katsnelson, I. V. Grigorieva, S. V. Dubonos, and A. A. Firsov. Two-dimensional gas of massless dirac fermions in graphene. *Nature*, 438:197, 2005.

[19] Yuanbo Zhang, Yan-Wen Tan, Horst L. Stormer, and Philip Kim. Experimental observation of the quantum hall effect and berry's phase in graphene. *Nature*, 438:201, 2005.

[20] A. K. Geim and K. S. Novoselov. The rise of graphene. *Nat. Mater.*, 6:183, 2007.

[21] K.I. Bolotin, K.J. Sikes, Z. Jiang, M. Klima, G. Fudenberg, J. Hone, P. Kim, and H.L. Stormer. Ultrahigh electron mobility in suspended graphene. *Solid State Commun.*, 146(9):351 – 355, 2008.

[22] K. I. Bolotin, K. J. Sikes, J. Hone, H. L. Stormer, and P. Kim. Temperature-dependent transport in suspended graphene. *Phys. Rev. Lett.*, 101:096802, 2008.

[23] Xu Du, Ivan Skachko, Anthony Barker, and Eva Y. Andrei. Approaching ballistic transport in suspended graphene. *Nat. Nanotechnol.*, 3:491–, 2008.

[24] N. Sule and I. Knezevic. Phonon-limited electron mobility in graphene calculated using tight-binding bloch waves. *J. Appl. Phys.*, 112(5):053702, 2012.

[25] Jian-Hao Chen, Chaun Jang, Shudong Xiao, Masa Ishigami, and Michael S. Fuhrer. Intrinsic and extrinsic performance limits of graphene devices on SiO_2. *Nat. Nanotechnol.*, 3:206–, 2008.

[26] K. Nagashio, T. Yamashita, T. Nishimura, K. Kita, and A. Toriumi. Electrical transport properties of graphene on SiO2 with specific surface structures. *J. Appl. Phys.*, 110(2):024513, 2011.

[27] C. R. Dean, A. F. Young, I. Meric, C. Lee, L. Wang, S. Sorgenfrei, K. Watanabe, T. Taniguchi, P. Kim, K. L. Shepard, and J. Hone. Boron nitride substrates for high-quality graphene electronics. *Nat. Nanotechnol.*, 5:722–, 2010.

[28] Xuesong Li, Yanwu Zhu, Weiwei Cai, Mark Borysiak, Boyang Han, David Chen, Richard D. Piner, Luigi Colombo, and Rodney S. Ruoff. Transfer of large-area graphene films for high-performance transparent conductive electrodes. *Nano Lett.*, 9:4359–4363, 2009.

[29] N. Sule, S. C. Hagness, and I. Knezevic. Clustered impurities and carrier transport in supported graphene. *Phys. Rev. B*, 89:165402, 2014.

[30] Zhun-Yong Ong and Massimo V. Fischetti. Theory of interfacial plasmon-phonon scattering in supported graphene. *Phys. Rev. B*, 86:165422, 2012.

[31] Yufeng Hao, M. S. Bharathi, Lei Wang, Yuanyue Liu, Hua Chen, Shu Nie, Xiaohan Wang, Harry Chou, Cheng Tan, Babak Fallahazad, H. Ramanarayan, Carl W. Magnuson, Emanuel Tutuc, Boris I. Yakobson, Kevin F. McCarty, Yong-Wei Zhang, Philip Kim, James Hone, Luigi Colombo, and Rodney S. Ruoff. The role of surface oxygen in the growth of large single-crystal graphene on copper. *Science*, 342(6159):720–723, 2013.

[32] Jae-Hyun Lee, Eun Kyung Lee, Won-Jae Joo, Yamujin Jang, Byung-Sung Kim, Jae Young Lim, Soon-Hyung Choi, Sung Joon Ahn, Joung Real Ahn, Min-Ho Park, Cheol-Woong Yang, Byoung Lyong Choi, Sung-Woo Hwang, and Dongmok Whang. Wafer-scale growth of single-crystal monolayer graphene on reusable hydrogen-terminated germanium. *Science*, 344(6181):286–289, 2014.

[33] Hua Yu, Mengzhou Liao, Wenjuan Zhao, Guodong Liu, X. J. Zhou, Zheng Wei, Xiaozhi Xu, Kaihui Liu, Zonghai Hu, Ke Deng, Shuyun Zhou, Jin-An Shi, Lin Gu, Cheng Shen, Tingting Zhang, Luojun Du, Li Xie, Jianqi Zhu, Wei Chen, Rong Yang, Dongxia Shi, and Guangyu Zhang. Wafer-scale growth and transfer of highly-oriented monolayer MoS_2 continuous films. *ACS Nano*, 11(12):12001–12007, 2017.

[34] Branimir Radisavljevic and Andras Kis. Mobility engineering and a metal-insulator transition in monolayer MoS_2. *Nat. Mater.*, 12(9):815–820, 2013.

[35] Matin Amani, Matthew L. Chin, A. Glen Birdwell, Terrance P. O' Regan, Sina Najmaei, Zheng Liu, Pulickel M. Ajayan, Jun Lou, and Madan Dubey. Electrical performance of monolayer MoS_2 field-effect transistors prepared by chemical vapor deposition. *Appl. Phys. Lett.*, 102(19):193107, 2013.

[36] E. Pop. Energy dissipation and transport in nanoscale devices. *Nano Research*, 3(3):147–169, 2010.

[37] Kyle L. Grosse, Myung-Ho Bae, Feifei Lian, Eric Pop, and William P. King. Nanoscale Joule heating, Peltier cooling and current crowding at graphene-metal contacts. *Nat. Nanotechnol.*, 6:287–290, 2011.

[38] Saptarshi Das and Joerg Appenzeller. Where does the current flow in two-dimensional layered systems? *Nano Lett.*, 13:3396–3402, 2013.

[39] Saurabh V. Suryavanshi and Eric Pop. S2ds: Physics-based compact model for circuit simulation of two-dimensional semiconductor devices including non-idealities. *J. Appl. Phys.*, 120:224503, 2016.

[40] P. Yasaei, C. J. Foss, K. Karis, A. Behranginia, A. El-Ghandour, A. Fathizadeh, A. K. Majee, C. Foster, F. Khalili-Araghi, Z. Aksamija, and A. Salehi-Khojin. Interfacial thermal transport in monolayer graphene- and MoS_2-based devices. *Adv. Mater. Interfaces*, page 1700334, 2017.

[41] Eilam Yalon, Connor J. McClellan, Kirby K. H. Smithe, Miguel Munoz Rojo, Runjie Lily Xu, Saurabh V. Suryavanshi, Alex J. Gabourie, Christopher M. Neumann, Feng Xiong, Amir Barati Farimani, and Eric Pop. Energy dissipation in monolayer MoS_2 electronics. *Nano Lett.*, 17(6):3429–3433, 2017.

[42] Zhun-Yong Ong, Yongqing Cai, and Gang Zhang. Theory of substrate-directed heat dissipation for single-layer graphene and other two-dimensional crystals. *Phys. Rev. B*, 94:165427, 2016.

[43] Gabriela C Correa, Cameron J Foss, and Zlatan Aksamija. Interface thermal conductance of van der Waals monolayers on amorphous substrates. *Nanotechnology*, 28(13):135402, 2017.

[44] Cameron J. Foss and Zlatan Aksamija. Quantifying thermal boundary conductance of 2D-3D interfaces. *2D Mater.*, 6(2):025019, feb 2019.

[45] Poya Yasaei, Amirhossein Behranginia, Zahra Hemmat, Ahmed I. El-Ghandour, Craig D. Foster, and Amin Salehi-Khojin. Quantifying the limits of through-plane thermal dissipation in 2D-material-based systems. *2D Mater.*, 4(3):035027, 2017.

[46] Sam Vaziri, Eilam Yalon, Miguel Muñoz Rojo, Saurabh V. Suryavanshi, Huairuo Zhang, Connor J. McClellan, Connor S. Bailey, Kirby K. H. Smithe, Alexander J. Gabourie, Victoria Chen, Sanchit Deshmukh, Leonid Bendersky, Albert V. Davydov, and Eric Pop. Ultrahigh thermal isolation across heterogeneously layered two-dimensional materials. *Sci. Adv.*, 5(8), 2019.

[47] Bolin Liao, Bo Qiu, Jiawei Zhou, Samuel Huberman, Keivan Esfarjani, and Gang Chen. Significant reduction of lattice thermal conductivity by the electron-phonon interaction in silicon with high carrier concentrations: A first-principles study. *Phys. Rev. Lett.*, 114:115901, 2015.

[48] Sheng-Ying Yue, Runqing Yang, and Bolin Liao. Controlling thermal conductivity of two-dimensional materials via externally induced phonon-electron interaction. *Phys. Rev. B*, 100:115408, 2019.

[49] N. C. Wang, S. Sinha, B. Cline, C. D. English, G. Yeric, and E. Pop. Replacing copper interconnects with graphene at a 7-nm node. In *2017 IEEE International Interconnect Technology Conference (IITC)*, pages 1–3, 2017.

[50] K. S. Novoselov, V. I. Fal'ko, L. Colombo, P. R. Gellert, M. G. Schwab, and K. Kim. A roadmap for graphene. *Nature*, 490:192–200, 2012.

[51] Lin-Bao Luo, Xiao-Bao Yang, Feng-Xia Liang, Hu Xu, Yu Zhao, Xing Xie, Wen-Feng Zhang, and Shuit-Tong Lee. Surface defects-induced p-type conduction of silicon nanowires. *J. Phys. Chem. C*, 115(38):18453–18458, 2011.

[52] Dmitry A. Kislitsyn, Vancho Kocevski, Jon M. Mills, Sheng-Kuei Chiu, Christian F. Gervasi, Benjamen N. Taber, Ariel E. Rosenfield, Olle Eriksson, Jn Rusz, Andrea M. Goforth, and George V. Nazin. Mapping of defects in individual silicon nanocrystals using real-space spectroscopy. *J. Phys. Chem. Lett.*, 7(6):1047–1054, 2016.

[53] Bin Peng, Wei Zheng, Jiantao Qin, and Wanli Zhang. Two-dimensional MX2 semiconductors for sub-5 nm junctionless field effect transistors. *Materials (Basel, Switzerland)*, 11(3):430, 2018.

[54] Matthew Yankowitz, Jiamin Xue, Daniel Cormode, Javier D. Sanchez-Yamagishi, K. Watanabe, T. Taniguchi, Pablo Jarillo-Herrero, Philippe Jacquod, and Brian J. LeRoy. Emergence of superlattice dirac points in graphene on hexagonal boron nitride. *Nat. Phys.*, 8:382–386, 2012.

[55] Manish Chhowalla, Hyeon Suk Shin, Goki Eda, Lain-Jong Li, Kian Ping Loh, and Hua Zhang. The chemistry of two-dimensional layered transition metal dichalcogenide nanosheets. *Nat. Chem.*, 5:263–275, 2013.

[56] M. Prunnila, J. Ahopelto, and F. Gamiz. Electron mobility in ultrathin silicon-on-insulator layers at 4.2 k. *Appl. Phys. Lett.*, 84(13):2298–2300, 2004.

[57] Alexander A. Balandin. Thermal properties of graphene and nanostructured carbon materials. *Nat. Mater.*, 10:569–581, 2011.

[58] E. H. Cho, M. J. Kim, H. Sohn, W. H. Shin, J. Y. Won, Y. Kim, C. Kwak, C. S. Lee, and Y. S. Woo. A graphene mesh as a hybrid electrode for foldable devices. *Nanoscale*, 10:628–638, 2018.

[59] R. R. Nair, P. Blake, A. N. Grigorenko, K. S. Novoselov, T. J. Booth, T. Stauber, N. M. R. Peres, and A. K. Geim. Fine structure constant defines visual transparency of graphene. *Science*, 320(5881):1308–1308, 2008.

[60] Jun Huang, Sivasubramanian Somu, and Ahmed Busnaina. A molybdenum disulfide/carbon nanotube heterogeneous complementary inverter. *Nanotechnology*, 23(33):335203, 2012.

[61] Mahmut Tosun, Steven Chuang, Hui Fang, Angada B. Sachid, Mark Hettick, Yongjing Lin, Yuping Zeng, and Ali Javey. High-gain inverters based on WSe_2 complementary field-effect transistors. *ACS Nano*, 8(5):4948–4953, 2014.

[62] Jaesung Lee, Zenghui Wang, Keliang He, Rui Yang, Jie Shan, and Philip X.-L. Feng. Electrically tunable single- and few-layer MoS_2 nanoelectromechanical systems with broad dynamic range. *Sci. Adv.*, 4(3), 2018.

[63] Britton W. H. Baugher, Hugh O. H. Churchill, Yafang Yang, and Pablo Jarillo-Herrero. Optoelectronic devices based on electrically tunable pn diodes in a monolayer dichalcogenide. *Nat. Nanotechnol.*, 9:262–267, 2014.

[64] M. M. Furchi, A. A. Zechmeister, F. Hoeller, S. Wachter, A. Pospischil, and T. Mueller. Photovoltaics in van der waals heterostructures. *IEEE Journal of Selected Topics in Quantum Electronics*, 23(1):106–116, 2017.

[65] Di Xiao, Gui-Bin Liu, Wanxiang Feng, Xiaodong Xu, and Wang Yao. Coupled spin and valley physics in monolayers of MoS_2 and other group-vi dichalcogenides. *Phys. Rev. Lett.*, 108:196802, 2012.

[66] Rudren Ganatra and Qing Zhang. Few-layer MoS_2: A promising layered semiconductor. *ACS Nano*, 8:4074, 2014.

[67] Subhamoy Ghatak, Atindra Nath Pal, and Arindam Ghosh. Nature of electronic states in atomically thin MoS_2 field-effect transistors. *ACS Nano*, 5(10):7707–7712, 2011.

[68] Zhun-Yong Ong and Massimo V. Fischetti. Mobility enhancement and temperature dependence in top-gated single-layer MoS_2. *Phys. Rev. B*, 88:165316, 2013.

[69] B. Radisavljevic, A. Radenovic, J. Brivio, V. Giacometti, and A. Kis. Single-layer MoS_2 transistors. *Nat. Nanotechnol.*, 6:147, 2011.

[70] Rajesh Kappera, Damien Voiry, Sibel Ebru Yalcin, Wesley Jen, Muharrem Acerce, Sol Torrel, Brittany Branch, Sidong Lei, Weibing Chen, Sina Najmaei, Jun Lou, Pulickel M. Ajayan, Gautam Gupta, Aditya D. Mohite, and Manish Chhowalla. Metallic 1T phase source/drain electrodes for field effect transistors from chemical vapor deposited MoS_2. *Appl. Phys. Lett. Mater.*, 2:092516, 2014.

[71] Wei-Fan Hsu, Li-Syuan Lu, Po-Chun Kuo, Jie-He Chen, Wei-Chen Chueh, Han Yeh, Hui-Ling Kao, Jyh-Shin Chen, and Wen-Hao Chang. Monolayer mos2 enabled single-crystalline growth of aln on si(100) using low-temperature helicon sputtering. *ACS Appl. Nano Mater.*, 2(4):1964–1969, 2019.

[72] Jing-Kai Huang, Jiang Pu, Chang-Lung Hsu, Ming-Hui Chiu, Zhen-Yu Juang, Yung-Huang Chang, Wen-Hao Chang, Yoshihiro Iwasa, Taishi Takenobu, and Lain-Jong Li. Large-area synthesis of highly crystalline WSe_2 monolayers and device applications. *ACS Nano*, 8(1):923–930, 2014.

[73] Sunkook Kim, Aniruddha Konar, Wan-Sik Hwang, Jong Hak Lee, Jiyoul Lee, Jaehyun Yang, Changhoon Jung, Hyoungsub Kim, Ji-Beom Yoo, Jae-Young Choi, Yong Wan Jin, Sang Yoon Lee, Debdeep Jena, Woong Choi, and Kinam Kim. High-mobility and low-power thin-film transistors based on multilayer MoS_2 crystals. *Nat. Commun.*, 3:1011, August 2012.

[74] Saptarshi Das, Hong-Yan Chen, Ashish Verma Penumatcha, and Joerg Appenzeller. High performance multilayer MoS_2 transistors with scandium contacts. *Nano Lett.*, 13(1):100–105, 2013.

[75] N. R. Pradhan, D. Rhodes, S. Memaran, J. M. Poumirol, D. Smirnov, S. Talapatra, S. Feng, N. Perea-Lopez, A. L. Elias, M. Terrones, P. M. Ajayan, and L. Balicas. Hall and field-effect mobilities in few layered p-WSe_2 field-effect transistors. *Sci. Rep.*, 5:8979, March 2015.

[76] Xu Cui, Gwan-Hyoung Lee, Young Duck Kim, Ghidewon Arefe, Pinshane Y. Huang, Chul-Ho Lee, Daniel A. Chenet, Xian Zhang, Lei Wang, Fan Ye, Filippo Pizzocchero, Bjarke S. Jessen, Kenji Watanabe, Takashi Taniguchi, David A. Muller, Tony Low, Philip Kim, and James Hone. Multi-terminal transport measurements of MoS_2 using a van der Waals heterostructure device platform. *Nat. Nanotechnol.*, 10:534, Appl. Phys. Rev. 2015.

[77] Yang Sui and Joerg Appenzeller. Screening and interlayer coupling in multilayer graphene field-effect transistors. *Nano Lett.*, 9:2973–2977, 2009.

[78] Saptarshi Das and Joerg Appenzeller. Screening and interlayer coupling in multilayer MoS_2. *Phys. Status Solidi RRL*, 7:268–273, 2013.

[79] Zhun-Yong Ong. Thickness-dependent kapitza resistance in multilayered graphene and other two-dimensional crystals. *Phys. Rev. B*, 95:155309, Apr 2017.

[80] Amirhossein Behranginia, Zahra Hemmat, Arnab K. Majee, Cameron J. Foss, Poya Yasaei, Zlatan Aksamija, and Amin Salehi-Khojin. Power dissipation of WSe_2 field-effect transistors probed by low-frequency Raman thermometry. *ACS Appl. Mater. Interfaces*, 10(29):24892–24898, 2018.

[81] Poya Yasaei, Zahra Hemmat, Cameron J. Foss, Shixuan Justin Li, Liang Hong, Amirhossein Behranginia, Leily Majidi, Robert F. Klie, Michel W. Barsoum, Zlatan Aksamija, and Amin Salehi-Khojin. Enhanced thermal boundary conductance in few-layer ti3c2 mxene with encapsulation. *Adv. Mater.*, 30(43):1801629, 2018.

[82] Nan Ma and Debdeep Jena. Charge scattering and mobility in atomically thin semiconductors. *Phys. Rev. X*, 4:011043, Mar 2014.

[83] Shuigang Xu, Zefei Wu, Huanhuan Lu, Yu Han, Gen Long, Xiaolong Chen, Tianyi Han, Weiguang Ye, Yingying Wu, Jiangxiazi Lin, Junying Shen, Yuan Cai, Yuheng He, Fan Zhang, Rolf Lortz, Chun Cheng, and Ning Wang. Universal low-temperature ohmic contacts for quantum transport in transition metal dichalcogenides. *2D Mater.*, 3:021007, 2016.

[84] Amirhossein Behranginia, Poya Yasaei, Arnab K. Majee, Vinod K. Sangwan, Fei Long, Cameron J. Foss, Tara Foroozan, Shadi Fuladi, Mohammad Reza Hantehzadeh, Reza Shahbazian-Yassar, Mark C. Hersam, Zlatan Aksamija, and Amin Salehi-Khojin. Direct growth of high mobility and low-noise lateral MoS_2 graphene heterostructure electronics. *Small*, 13:1604301, 2017.

[85] Xiaokun Gu and Ronggui Yang. Phonon transport in single-layer transition metal dichalcogenides: A first-principles study. *Appl. Phys. Lett.*, 105(13):131903, 2014.

[86] Hui Fang, Steven Chuang, Ting Chia Chang, Kuniharu Takei, Toshitake Takahashi, and Ali Javey. High-performance single layered wse2 p-fets with chemically doped contacts. *Nano Lett.*, 12(7):3788–3792, July 2012.

[87] Wei Liu, Jiahao Kang, Deblina Sarkar, Yasin Khatami, Debdeep Jena, and Kaustav Banerjee. Role of metal contacts in designing high-performance monolayer n-type WSe_2 field effect transistors. *Nano Lett.*, 13(5):1983–1990, May 2013.

[88] Arnab K. Majee, Zahra Hemmat, Cameron J. Foss, Amin Salehi-Khojin, and Zlatan Aksamija. Current rerouting improves heat removal in few-layer WSe_2 devices. *ACS Appl. Mater. Interfaces*, 12(12):14323–14330, 2020.

[89] Kirby Smithe, Chris D. English, Saurabh V. Suryavanshi, and Eric Pop. High-field transport and velocity saturation in synthetic monolayer MoS_2. *Nano Lett.*, 18(7):4516–4522, 2018.

[90] Gianluca Fiori, Bartholomus N. Szafranek, Giuseppe Iannaccone, and Daniel Neumaier. Velocity saturation in few-layer MoS_2 transistor. *Appl. Phys. Lett.*, 103(23):233509, 2013.

[91] Zhenghe Jin, Xiaodong Li, Jeffrey T. Mullen, and Ki Wook Kim. Intrinsic transport properties of electrons and holes in monolayer transition-metal dichalcogenides. *Phys. Rev. B*, 90:045422, 2014.

[92] Eilam Yalon, Ozgur Burak Aslan, Kirby K. H. Smithe, Connor J. McClellan, Saurabh V. Suryavanshi, Feng Xiong, Aditya Sood, Christopher M. Neumann, Xiaoqing Xu, Kenneth E. Goodson, Tony F. Heinz, and Eric Pop. Temperature-dependent thermal boundary conductance of monolayer MoS_2 by Raman thermometry. *ACS Appl. Mater. Interfaces*, 9(49):43013–43020, 2017.

[93] A. K. Geim and I. V. Grigorieva. Van der Waals heterostructures. *Nature*, 499:419, July 2013.

[94] Poya Yasaei, Cameron J. Foss, Klas Karis, Amirhossein Behranginia, Ahmed I. El-Ghandour, Arman Fathizadeh, Javier Olivares, Arnab K. Majee, Craig D. Foster, Fatemeh Khalili-Araghi, Zlatan Aksamija, and Amin Salehi-Khojin. Interfacial thermal transport in monolayer mos2- and graphene-based devices. *Adv. Mater. Interfaces*, 4:1700334–, 2017.

[95] Yingchao Zhang, Xun Shi, Wenjing You, Zhensheng Tao, Yigui Zhong, Fairoja Cheenicode Kabeer, Pablo Maldonado, Peter M. Oppeneer, Michael Bauer, Kai Rossnagel, Henry Kapteyn, and Margaret Murnane. Coherent modulation of the electron temperature and electron–phonon couplings in a 2d material. *Proc. Nat. Acad. Sci.*, 117(16):8788–8793, 2020.

[96] Amirhossein Behranginia, Zahra Hemmat, Arnab K. Majee, Cameron J. Foss, Poya Yasaei, Zlatan Aksamija, and Amin Salehi-Khojin. Power dissipation of WSe_2 field-effect transistors probed by low-frequency raman thermometry. *ACS Appl. Mater. Interfaces*, 10(29):24892–24898, 2018.

[97] Paolo Giannozzi, Stefano Baroni, Nicola Bonini, Matteo Calandra, Roberto Car, Carlo Cavazzoni, Davide Ceresoli, Guido L Chiarotti, Matteo Cococcioni, Ismaila Dabo, Andrea Dal Corso, Stefano de Gironcoli, Stefano Fabris, Guido Fratesi, Ralph Gebauer, Uwe Gerstmann, Christos Gougoussis, Anton Kokalj, Michele Lazzeri, Layla Martin-Samos, Nicola Marzari, Francesco Mauri, Riccardo Mazzarello, Stefano Paolini, Alfredo Pasquarello, Lorenzo Paulatto, Carlo Sbraccia, Sandro Scandolo, Gabriele Sclauzero, Ari P Seitsonen, Alexander Smogunov, Paolo Umari, and Renata M Wentzcovitch. Quantum espresso: a modular and open-source software project for quantum simulations of materials. *J. Phys. Condens. Matter*, 21(39):395502, 2009.

[98] Cameron J Foss and Zlatan Aksamija. Quantifying thermal boundary conductance of 2d-3d interfaces. *2D Mater.*, 6(2):025019, 2019.

[99] J. Ziman. *Electrons and Phonons: The Theory of Transport Phenomena in Solids*. Oxford University Press Inc., 1960.

[100] M. Lundstrom and C. Jeong. *Near-equilibrium transport Fundamentals and applications*. World Scientific Publishing Co. Pte. Ltd., 2 edition, 2013.

[101] D. A. Broido, M. Malorny, G. Birner, Natalio Mingo, and D. A. Stewart. Intrinsic lattice thermal conductivity of semiconductors from first principles. *Appl. Phys. Lett.*, 91(23):231922, 2007.

[102] A. Ward and D. A. Broido. Intrinsic phonon relaxation times from first-principles studies of the thermal conductivities of Si and Ge. *Phys. Rev. B*, 81(8):085205, 2010.

[103] Ankit Jain and Alan J. H. McGaughey. Thermal transport by phonons and electrons in aluminum, silver, and gold from first principles. *Phys. Rev. B*, 93:081206, 2016.

[104] B. D. Kong, S. Paul, M. Buongiorno Nardelli, and K. W. Kim. First-principles analysis of lattice thermal conductivity in monolayer and bilayer graphene. *Phys. Rev. B*, 80(3):033406, 2009.

[105] Alexander A. Balandin. Thermal properties of graphene and nanostructured carbon materials. *Nature Mater.*, 10(8):569–581, 2011.

[106] L. Lindsay, Wu Li, Jesús Carrete, Natalio Mingo, D. A. Broido, and T. L. Reinecke. Phonon thermal transport in strained and unstrained graphene from first principles. *Phys. Rev. B*, 89:155426, 2014.

[107] P. Xu, M. Neek-Amal, S. D. Barber, J. K. Schoelz, M. L. Ackerman, P. M. Thibado, A. Sadeghi, and F. M. Peeters. Unusual ultra-low-frequency fluctuations in free-standing graphene. *Nat. Commun.*, 5:3720, 2014.

[108] Arnab K. Majee and Zlatan Aksamija. Length divergence of the lattice thermal conductivity in suspended graphene nanoribbons. *Phys. Rev. B*, 93:235423, 2016.

[109] L. Lindsay, D. A. Broido, and T. L. Reinecke. First-principles determination of ultrahigh thermal conductivity of boron arsenide: A competitor for diamond? *Phys. Rev. Lett.*, 111:025901, 2013.

[110] Catalin Chiritescu, David G. Cahill, Ngoc Nguyen, David Johnson, Arun Bodapati, Pawel Keblinski, and Paul Zschack. Ultralow thermal conductivity in disordered, layered WSe_2 crystals. *Science*, 315(5810):351–353, 2007.

[111] E. T. Swartz and R. O. Pohl. Thermal boundary resistance. *Rev. Mod. Phys.*, 61(3):605–668, 1989.

[112] S. P. Hepplestone and G. P. Srivastava. Theory of interface scattering of phonons in superlattices. *Phys. Rev. B*, 82:144303, 2010.

[113] Patrick E. Hopkins, John C. Duda, and Pamela M. Norris. Anharmonic phonon interactions at interfaces and contributions to thermal boundary conductance. *J. Heat Transf.*, 133:062401, 2011.

[114] Z. Aksamija and I. Knezevic. Anisotropy and boundary scattering in the lattice thermal conductivity of silicon nanomembranes. *Phys. Rev. B*, 82:045319, 2010.

[115] Huicong Dong, Bin Wen, and Roderick Melnik. Relative importance of grain boundaries and size effects in thermal conductivity of nanocrystalline materials. *Sci. Rep.*, 4:7037, 2014.

[116] Poya Yasaei, Arman Fathizadeh, Reza Hantehzadeh, Arnab K. Majee, Ahmed El-Ghandour, David Estrada, Craig Foster, Zlatan Aksamija, Fatemeh Khalili-Araghi, and Amin Salehi-Khojin. Bimodal phonon scattering in graphene grain boundaries. *Nano Lett.*, 15:4532–4540, 2015.

[117] Allon I. Hochbaum, Renkun Chen, Raul Diaz Delgado, Wenjie Liang, Erik C. Garnett, Mark Najarian, Arun Majumdar, and Peidong Yang. Enhanced thermoelectric performance of rough silicon nanowires. *Nature*, 451:163–167, 2008.

[118] M. Upadhyaya and Z. Aksamija. Non-diffusive lattice thermal transport in si-ge alloy nanowires. *Phys. Rev. B*, 94:174303, 2016.

[119] Pierre Martin, Zlatan Aksamija, Eric Pop, and Umberto Ravaioli. Impact of phonon-surface roughness scattering on thermal conductivity of thin si nanowires. *Phys. Rev. Lett.*, 102(12):125503, 2009.

[120] E. S. Landry and A. J. H. McGaughey. Effect of film thickness on the thermal resistance of confined semiconductor thin films. *J. Appl. Phys.*, 107(1):013521, 2010.

[121] Changwook Jeong, Supriyo Datta, and Mark Lundstrom. Thermal conductivity of bulk and thin-film silicon: A landauer approach. *J. Appl. Phys.*, 111(9):093708, 2012.

[122] G. Chen. Thermal conductivity and ballistic-phonon transport in the cross-plane direction of superlattices. *Phys. Rev. B*, 57(23):14958–14973, 1998.

[123] D. A. Broido and T. L. Reinecke. Lattice thermal conductivity of superlattice structures. *Phys. Rev. B*, 70(8):081310, 2004.

[124] Z. Aksamija and I. Knezevic. Thermal conductivity of $Si_{1-x}Ge_x$/$Si_{1-y}Ge_y$ superlattices: Competition between interfacial and internal scattering. *Phys. Rev. B*, 88:155318, 2013.

[125] Xinyu Wang, Yang Hong, Paddy K L Chan, and Jingchao Zhang. Phonon thermal transport in silicene-germanene superlattice: a molecular dynamics study. *Nanotechnology*, 28:255403, 2017.

[126] Ronggui Yang and Gang Chen. Thermal conductivity modeling of periodic two-dimensional nanocomposites. *Phys. Rev. B*, 69(19):195316, 2004.

[127] Jen-Kan Yu, Slobodan Mitrovic, Douglas Tham, Joseph Varghese, and James R. Heath. Reduction of thermal conductivity in phononic nanomesh structures. *Nat Nano*, 5:718–721, 2010.

[128] G. Pernot, M. Stoffel, I. Savic, F. Pezzoli, P. Chen, G. Savelli, A. Jacquot, J. Schumann, U. Denker, I. Mnch, Ch. Deneke, O. G. Schmidt, J. M. Rampnoux, S. Wang, M. Plissonnier, A. Rastelli, S. Dilhaire, and N. Mingo. Precise control of thermal conductivity at the nanoscale through individual phonon-scattering barriers. *Nat Mater*, 9:491–495, 2010.

[129] Daniel Abarbanel and Jesse Maassen. Modeling quasi-ballistic transient thermal transport with spatially sinusoidal heating: A McKelvey-Shockley flux approach. *J. Appl. Phys.*, 121(20):204305, 2017.

[130] C. W. Chang, D. Okawa, H. Garcia, A. Majumdar, and A. Zettl. Breakdown of fourier's law in nanotube thermal conductors. *Phys. Rev. Lett.*, 101:075903, 2008.

[131] Mark E. Siemens, Qing Li, Ronggui Yang, Keith A. Nelson, Erik H. Anderson, Margaret M. Murnane, and Henry C. Kapteyn. Quasi-ballistic thermal transport from nanoscale interfaces observed using ultrafast coherent soft x-ray beams. *Nat Mater*, 9:26–30, 2010.

[132] G. Chen. Nonlocal and nonequilibrium heat conduction in the vicinity of nanoparticles. *J. Heat Trans.*, 118:539–545, 1996.

[133] N. Mingo and D. A. Broido. Carbon nanotube ballistic thermal conductance and its limits. *Phys. Rev. Lett.*, 95(9):096105, 2005.

[134] Maria N. Luckyanova, Jivtesh Garg, Keivan Esfarjani, Adam Jandl, Mayank T. Bulsara, Aaron J. Schmidt, Austin J. Minnich, Shuo Chen, Mildred S. Dresselhaus, Zhifeng Ren, Eugene A. Fitzgerald, and Gang Chen. Coherent phonon heat conduction in superlattices. *Science*, 338(6109):936–939, 2012.

[135] G. D. Mahan and Francisco Claro. Nonlocal theory of thermal conductivity. *Phys. Rev. B*, 38:1963–1969, 1988.

[136] Gang Chen. Ballistic-diffusive heat-conduction equations. *Phys. Rev. Lett.*, 86:2297–2300, 2001.

[137] A. J. Minnich, J. A. Johnson, A. J. Schmidt, K. Esfarjani, M. S. Dresselhaus, K. A. Nelson, and G. Chen. Thermal conductivity spectroscopy technique to measure phonon mean free paths. *Phys. Rev. Lett.*, 107(9):095901, 2011.

[138] Justin P. Freedman, Jacob H. Leach, Edward A. Preble, Zlatko Sitar, Robert F. Davis, and Jonathan A. Malen. Universal phonon mean free path spectra in crystalline semiconductors at high temperature. *Sci. Rep.*, 3:2963, 2013.

[139] Jeremy A. Johnson, A. A. Maznev, John Cuffe, Jeffrey K. Eliason, Austin J. Minnich, Timothy Kehoe, Clivia M. Sotomayor Torres, Gang Chen, and Keith A. Nelson. Direct measurement of room-temperature nondiffusive thermal transport over micron distances in a silicon membrane. *Phys. Rev. Lett.*, 110:025901, 2013.

[140] Lingping Zeng, Kimberlee C. Collins, Yongjie Hu, Maria N. Luckyanova, Alexei A. Maznev, Samuel Huberman, Vazrik Chiloyan, Jiawei Zhou, Xiaopeng Huang, Keith A. Nelson, and Gang Chen. Measuring phonon mean free path distributions by probing quasiballistic phonon transport in grating nanostructures. *Sci. Rep.*, 5:17131, 2015.

[141] Philip B. Allen. Size effects in thermal conduction by phonons. *Phys. Rev. B*, 90:054301, Aug 2014.

[142] A J Minnich. Advances in the measurement and computation of thermal phonon transport properties. *J. Phys.: Condens. Matter*, 27(5):053202, 2015.

[143] Sebastian G. Volz. Thermal insulating behavior in crystals at high frequencies. *Phys. Rev. Lett.*, 87:074301, 2001.

[144] F. X. Alvarez and D. Jou. Memory and nonlocal effects in heat transport: From diffusive to ballistic regimes. *Appl. Phys. Lett.*, 90(8):083109, 2007.

[145] Younès Ezzahri and Karl Joulain. Dynamical thermal conductivity of bulk semiconductor crystals. *J. Appl. Phys.*, 112(8):083515, 2012.

[146] Y. Ezzahri and A. Shakouri. Ballistic and diffusive transport of energy and heat in metals. *Phys. Rev. B*, 79:184303, 2009.

[147] Y. Ezzahri, K. Joulain, and A. Shakouri. Transient energy and heat transport in metals: Effect of the discrete character of the lattice. *J. Heat Transfer*, 133:072401–072401–14, 2011.

[148] Pankaj Bhalla, Pradeep Kumar, Nabyendu Das, and Navinder Singh. Theory of the dynamical thermal conductivity of metals. *Phys. Rev. B*, 94:115114, 2016.

[149] Hideo Kaburaki, Ju Li, Sidney Yip, and Hajime Kimizuka. Dynamical thermal conductivity of argon crystal. *J. Appl. Phys.*, 102:043514, 2007.

[150] A. Sellitto, F. X. Alvarez, and D. Jou. Phonon-wall interactions and frequency-dependent thermal conductivity in nanowires. *J. Appl. Phys.*, 109(6):064317, 2011.

[151] Fan Yang and Chris Dames. Heating-frequency-dependent thermal conductivity: An analytical solution from diffusive to ballistic regime and its relevance to phonon scattering measurements. *Phys. Rev. B*, 91:165311, 2015.

[152] Joseph Callaway. Model for lattice thermal conductivity at low temperatures. *Phys. Rev.*, 113:1046–1051, 1959.

[153] Laurent Chaput. Direct solution to the linearized phonon Boltzmann equation. *Phys. Rev. Lett.*, 110:265506, 2013.

[154] S. Ghosh, I. Calizo, D. Teweldebrhan, E. P. Pokatilov, D. L. Nika, A. A. Balandin, W. Bao, F. Miao, and C. N. Lau. Extremely high thermal conductivity of graphene: Prospects for thermal management applications in nanoelectronic circuits. *Appl. Phys. Lett.*, 92:151911, 2008.

[155] Sangyeop Lee, David Broido, Keivan Esfarjani, and Gang Chen. Hydrodynamic phonon transport in suspended graphene. *Nat. Commun.*, 6:6290, 2015.

[156] Yangyu Guo and Moran Wang. Phonon hydrodynamics and its applications in nanoscale heat transport. *Physics Reports*, 595:1 – 44, 2015.

[157] Jingchao Zhang, Xiaopeng Huang, Yanan Yue, Jianmei Wang, and Xinwei Wang. Dynamic response of graphene to thermal impulse. *Phys. Rev. B*, 84:235416, 2011.

[158] Andrea Cepellotti, Giorgia Fugallo, Lorenzo Paulatto, Michele Lazzeri, Francesco Mauri, and Nicola Marzari. Phonon hydrodynamics in two-dimensional materials. *Nat. Commun.*, 6:6400, 2015.

[159] Marvin Chester. Second sound in solids. *Phys. Rev.*, 131:2013–2015, 1963.

[160] R. A. Guyer and J. A. Krumhansl. Dispersion relation for second sound in solids. *Phys. Rev.*, 133:A1411–A1417, 1964.

[161] R. A. Guyer and J. A. Krumhansl. Solution of the linearized phonon boltzmann equation. 148:766–778, 1966.

[162] Andrea Cepellotti and Nicola Marzari. Transport waves as crystal excitations. *Phys. Rev. Materials*, 1:045406, 2017.

[163] C. T. Lane, Henry A. Fairbank, and William M. Fairbank. Second sound in liquid helium ii. *Phys. Rev.*, 71:600–605, 1947.

[164] T. F. McNelly, S. J. Rogers, D. J. Channin, R. J. Rollefson, W. M. Goubau, G. E. Schmidt, J. A. Krumhansl, and R. O. Pohl. Heat pulses in naf: Onset of second sound. *Phys. Rev. Lett.*, 24:100–102, 1970.

[165] Howard E. Jackson, Charles T. Walker, and Thomas F. McNelly. Second sound in naf. *Phys. Rev. Lett.*, 25:26–28, 1970.

[166] V. Narayanamurti and R. C. Dynes. Observation of second sound in bismuth. *Phys. Rev. Lett.*, 28:1461–1465, 1972.

[167] Maxime Markov, Jelena Sjakste, Giuliana Barbarino, Giorgia Fugallo, Lorenzo Paulatto, Michele Lazzeri, Francesco Mauri, and Nathalie Vast. Hydrodynamic heat transport regime in bismuth: A theoretical viewpoint. *Phys. Rev. Lett.*, 120:075901, 2018.

[168] Akitoshi Koreeda, Ryuta Takano, and Seishiro Saikan. Second sound in $\mathrm{srtio_3}$. *Phys. Rev. Lett.*, 99:265502, 2007.

[169] Yee Kan Koh, David G. Cahill, and Bo Sun. Nonlocal theory for heat transport at high frequencies. *Phys. Rev. B*, 90:205412, 2014.

[170] M Omini and A Sparavigna. An iterative approach to the phonon Boltzmann equation in the theory of thermal conductivity. *Physica B: Condensed Matter*, 212(2):101 – 112, 1995.

[171] L. Lindsay, D. A. Broido, and Natalio Mingo. Flexural phonons and thermal transport in graphene. *Phys. Rev. B*, 82:115427, 2010.

[172] Aleksandr Chernatynskiy and Simon R. Phillpot. Evaluation of computational techniques for solving the Boltzmann transport equation for lattice thermal conductivity calculations. *Phys. Rev. B*, 82:134301, 2010.

[173] Jinlong Ma, Wu Li, and Xiaobing Luo. Examining the callaway model for lattice thermal conductivity. *Phys. Rev. B*, 90:035203, 2014.

[174] Yangyu Guo and Moran Wang. Heat transport in two-dimensional materials by directly solving the phonon boltzmann equation under Callaway's dual relaxation model. *Phys. Rev. B*, 96:134312, 2017.

[175] Zhiwei Ding, Jiawei Zhou, Bai Song, Vazrik Chiloyan, Mingda Li, Te-Huan Liu, and Gang Chen. Phonon hydrodynamic heat conduction and knudsen minimum in graphite. *Nano Lett.*, 18(1):638–649, 2018. PMID: 29236507.

[176] D. T. Morelli, J. P. Heremans, and G. A. Slack. Estimation of the isotope effect on the lattice thermal conductivity of group iv and group iii-v semiconductors. *Phys. Rev. B*, 66:195304, 2002.

[177] Z. Aksamija and I. Knezevic. Lattice thermal conductivity of graphene nanoribbons: Anisotropy and edge roughness scattering. *Appl. Phys. Lett.*, 98:141919, 2011.

[178] Z. Aksamija and I. Knezevic. Thermal transport in graphene nanoribbons supported on $\mathrm{sio_2}$. *Phys. Rev. B*, 86:165426, 2012.

[179] Philip B. Allen. Improved callaway model for lattice thermal conductivity. *Phys. Rev. B*, 88:144302, 2013.

[180] Keith T. Regner, Daniel P. Sellan, Zonghui Su, Cristina H. Amon, Alan J.H. McGaughey, and Jonathan A. Malen. Broadband phonon mean free path contributions to thermal conductivity measured using frequency domain thermoreflectance. *Nat Commun*, 4:1640, 2013.

[181] John Cuffe, Jeffrey K. Eliason, A. A. Maznev, Kimberlee C. Collins, Jeremy A. Johnson, Andrey Shchepetov, Mika Prunnila, Jouni Ahopelto, Clivia M. Sotomayor Torres, Gang Chen, and Keith A. Nelson. Reconstructing phonon mean-free-path contributions to thermal conductivity using nanoscale membranes. *Phys. Rev. B*, 91:245423, 2015.

[182] Hang Zhang, Xiangwen Chen, Young-Dahl Jho, and Austin J. Minnich. Temperature-dependent mean free path spectra of thermal phonons along the c-axis of graphite. *Nano Lett.*, 16:1643–1649, 2016.

[183] D. D. Joseph and Luigi Preziosi. Heat waves. *Rev. Mod. Phys.*, 61:41–73, 1989.

[184] Lei Ren, Qi Zhang, Jun Yao, Zhengzong Sun, Ryosuke Kaneko, Zheng Yan, Sbastien Nanot, Zhong Jin, Iwao Kawayama, Masayoshi Tonouchi, James M. Tour, and Junichiro Kono. Terahertz and infrared spectroscopy of gated large-area graphene. *Nano Lett.*, 12(7):3711–3715, 2012.

[185] Younès Ezzahri and Karl Joulain. Dynamical thermoelectric coefficients of bulk semiconductor crystals: Towards high thermoelectric efficiency at high frequencies. *J. Appl. Phys.*, 115(22):223703, 2014.

[186] D. Y. Tzou. A unified field approach for heat conduction from macro- to micro-scales. *J. Heat Transf.*, 117(1):8–16, 1995.

[187] Myung-Ho Bae, Zuanyi Li, Zlatan Aksamija, Pierre N Martin, Feng Xiong, Zhun-Yong Ong, Irena Knezevic, and Eric Pop. Ballistic to diffusive crossover of heat flow in graphene ribbons. *Nat. Commun.*, 4:1734, 2013.

[188] Leonid A. Sidorenkov, Meng Khoon Tey, Rudolf Grimm, Yan-Hua Hou, Lev Pitaevskii, and Sandro Stringari. Second sound and the superfluid fraction in a fermi gas with resonant interactions. *Nature*, 498:78, 2013.

[189] Xuesong Li, Carl W. Magnuson, Archana Venugopal, Jinho An, Ji Won Suk, Boyang Han, Mark Borysiak, Weiwei Cai, Aruna Velamakanni, Yanwu Zhu, Lianfeng Fu, Eric M. Vogel, Edgar Voelkl, Luigi Colombo, and Rodney S. Ruoff. Graphene films with large domain size by a two-step chemical vapor deposition process. *Nano Lett.*, 10:4328–4334, 2010.

[190] H. F. Mataré. Carrier transport at grain boundaries in semiconductors. *J. Appl. Phys.*, 56(10):2605–2631, 1984.

[191] Andreas Isacsson, Aron W Cummings, Luciano Colombo, Luigi Colombo, Jari M Kinaret, and Stephan Roche. Scaling properties of polycrystalline graphene: a review. *2D Mater.*, 4:012002, 2017.

[192] Teng Ma, Zhibo Liu, Jinxiu Wen, Yang Gao, Xibiao Ren, Huanjun Chen, Chuanhong Jin, Xiu-Liang Ma, Ningsheng Xu, Hui-Ming Cheng, and Wencai Ren. Tailoring the thermal and electrical transport properties of graphene films by grain size engineering. *Nat. Commun.*, 8:14486–, 2017.

[193] Bohayra Mortazavi, Romain Quey, Alireza Ostadhossein, Aurelien Villani, Nicolas Moulin, Adri C.T. van Duin, and Timon Rabczuk. Strong thermal transport along polycrystalline transition metal dichalcogenides revealed by multiscale modeling for MoS_2. *Appl. Mater. Today*, 7:67 – 76, 2017.

[194] Z. Aksamija and I. Knezevic. Lattice thermal transport in large-area polycrystalline graphene. *Phys. Rev. B*, 90:035419, 2014.

[195] Justin C. Koepke, Joshua D. Wood, David Estrada, Zhun-Yong Ong, Kevin T. He, Eric Pop, and Joseph W. Lyding. Atomic-scale evidence for potential barriers and strong carrier scattering at graphene grain boundaries: A scanning tunneling microscopy study. *ACS Nano*, 7:75–86, 2013.

[196] Oleg V. Yazyev and Steven G. Louie. Electronic transport in polycrystalline graphene. *Nat. Mater.*, 9:806–809, 2010.

[197] Pter Vancs, Gza I. Mrk, Philippe Lambin, Alexandre Mayer, Yong-Sung Kim, Chanyong Hwang, and Lszl P. Bir. Electronic transport through ordered and disordered graphene grain boundaries. *Carbon*, 64:101 – 110, 2013.

[198] Hengji Zhang, Geunsik Lee, Cheng Gong, Luigi Colombo, and Kyeongjae Cho. Grain boundary effect on electrical transport properties of graphene. *J. Phys. Chem. C*, 118(5):2338–2343, 2014.

[199] Jie Sun, Na Lin, Zhenyu Li, Hao Ren, Cheng Tang, and Xian Zhao. Electronic and transport properties of graphene with grain boundaries. *RSC Adv.*, 6:1090–1097, 2016.

[200] Colin Ophus, Ashivni Shekhawat, Haider Rasool, and Alex Zettl. Large-scale experimental and theoretical study of graphene grain boundary structures. *Phys. Rev. B*, 92:205402, 2015.

[201] Sina Najmaei, Matin Amani, Matthew L. Chin, Zheng Liu, A. Glen Birdwell, Terrance P. ORegan, Pulickel M. Ajayan, Madan Dubey, and Jun Lou. Electrical transport properties of polycrystalline monolayer molybdenum disulfide. *ACS Nano*, 8:7930–7937, 2014.

[202] Hennrik Schmidt, Shunfeng Wang, Leiqiang Chu, Minglin Toh, Rajeev Kumar, Weijie Zhao, A. H. Castro Neto, Jens Martin, Shaffique Adam, Barbaros Özyilmaz, and Goki Eda. Transport properties of monolayer MoS_2 grown by chemical vapor deposition. *Nano Lett.*, 14:1909–1913, 2014.

[203] Arend M. van der Zande, Pinshane Y. Huang, Daniel A. Chenet, Timothy C. Berkelbach, YuMeng You, Gwan-Hyoung Lee, Tony F. Heinz, David R. Reichman, David A. Muller, and James C. Hone. Grains and grain boundaries in highly crystalline monolayer molybdenum disulphide. *Nat. Mater.*, 12(6):554–561, 2013.

[204] Sina Najmaei, Zheng Liu, Wu Zhou, Xiaolong Zou, Gang Shi, Sidong Lei, Boris I. Yakobson, Juan-Carlos Idrobo, Pulickel M. Ajayan, and Jun Lou. Vapour phase growth and grain boundary structure of molybdenum disulphide atomic layers. *Nat. Mater.*, 12(8):754–759, 2013.

[205] Thuc Hue Ly, David J. Perello, Jiong Zhao, Qingming Deng, Hyun Kim, Gang Hee Han, Sang Hoon Chae, Hye Yun Jeong, and Young Hee Lee. Misorientation-angle-dependent electrical transport across molybdenum disulfide grain boundaries. *Nat. Commun.*, 7:10426–, 2016.

[206] Kibum Kang, Saien Xie, Lujie Huang, Yimo Han, Pinshane Y. Huang, Kin Fai Mak, Cheol-Joo Kim, David Muller, and Jiwoong Park. High-mobility three-atom-thick semiconducting films with wafer-scale homogeneity. *Nature*, 520(7549):656–660, 2015.

[207] Lijie Ci, Li Song, Chuanhong Jin, Deep Jariwala, Dangxin Wu, Yongjie Li, Anchal Srivastava, Z. F. Wang, Kevin Storr, Luis Balicas, Feng Liu, and Pulickel M. Ajayan. Atomic layers of hybridized boron nitride and graphene domains. *Nat. Mater.*, 9(5):430–435, 2010.

[208] Gang Hee Han, Julio A. Rodrguez-Manzo, Chan-Woo Lee, Nicholas J. Kybert, Mitchell B. Lerner, Zhengqing John Qi, Eric N. Dattoli, Andrew M. Rappe, Marija Drndic, and A. T. Charlie Johnson. Continuous growth of hexagonal graphene and boron nitride in-plane heterostructures by atmospheric pressure chemical vapor deposition. *ACS Nano*, 7:10129–10138, 2013.

[209] Zheng Liu, Lulu Ma, Gang Shi, Wu Zhou, Yongji Gong, Sidong Lei, Xuebei Yang, Jiangnan Zhang, Jingjiang Yu, Ken P. Hackenberg, Aydin Babakhani, Juan-Carlos Idrobo, Robert Vajtai, Jun Lou, and Pulickel M. Ajayan. In-plane heterostructures of graphene and hexagonal boron nitride with controlled domain sizes. *Nat. Nano.*, 8(2):119–124, 2013.

[210] Yexin Deng, Zhe Luo, Nathan J. Conrad, Han Liu, Yongji Gong, Sina Najmaei, Pulickel M. Ajayan, Jun Lou, Xianfan Xu, and Peide D. Ye. Black phosphorus-monolayer MoS_2 van der waals heterojunction p-n diode. *ACS Nano*, 8:8292–8299, 2014.

[211] Daniele Stradi, Nick R. Papior, Ole Hansen, and Mads Brandbyge. Field effect in graphene-based van der waals heterostructures: Stacking sequence matters. *Nano Lett.*, 17:2660–2666, 2017.

[212] Andrey A Kistanov, Yongqing Cai, Yong-Wei Zhang, Sergey V Dmitriev, and Kun Zhou. Strain and water effects on the electronic structure and chemical activity of in-plane graphene/silicene heterostructure. *J. Phys. Condens. Matter*, 29(9):095302, 2017.

[213] Lili Yu, Yi-Hsien Lee, Xi Ling, Elton J. G. Santos, Yong Cheol Shin, Yuxuan Lin, Madan Dubey, Efthimios Kaxiras, Jing Kong, Han Wang, and Toms Palacios. Graphene/MoS_2 hybrid technology for large-scale two-dimensional electronics. *Nano Lett.*, 14(6):3055–3063, 2014.

[214] Henry Yu, Alex Kutana, and Boris I. Yakobson. Carrier delocalization in two-dimensional coplanar p-n junctions of graphene and metal dichalcogenides. *Nano Lett.*, 16:5032–5036, 2016.

[215] He Tian, Zhen Tan, Can Wu, Xiaomu Wang, Mohammad Ali Mohammad, Dan Xie, Yi Yang, Jing Wang, Lain-Jong Li, Jun Xu, and Tian-Ling Ren. Novel field-effect schottky barrier transistors based on graphene-MoS_2 heterojunctions. *Sci. Rep.*, 4:5951–, 2014.

[216] Xingen Liu and Zhongyao Li. Electric field and strain effect on graphene-MoS_2 hybrid structure: Ab initio calculations. *J. Phys. Chem. Lett.*, 6(16):3269–3275, 2015.

[217] Demetrio Logoteta, Gianluca Fiori, and Giuseppe Iannaccone. Graphene-based lateral heterostructure transistors exhibit better intrinsic performance than graphene-based vertical transistors as post-cmos devices. *Sci. Rep*, 4:6607–, 2014.

[218] Junfeng Zhang, Weiyu Xie, Jijun Zhao, and Shengbai Zhang. Band alignment of two-dimensional lateral heterostructures. *2D Mater.*, 4:015038, 2017.

[219] N. F. Mott. The theory of crystal rectifiers. *Proc. Royal Soc. London A: Mathematical, Physical and Engineering Sciences*, 171:27–38, 1939.

[220] Songbo Yang, Peng Zhou, Lin Chen, Qingqing Sun, Pengfei Wang, Shijin Ding, Anquan Jiang, and David Wei Zhang. Direct observation of the work function evolution of graphene-two-dimensional metal contacts. *J. Mater. Chem. C*, 2:8042–8046, 2014.

[221] Min Sup Choi, Gwan-Hyoung Lee, Young-Jun Yu, Dae-Yeong Lee, Seung Hwan Lee, Philip Kim, James Hone, and Won Jong Yoo. Controlled charge trapping by molybdenum disulphide and graphene in ultrathin heterostructured memory devices. *Nat. Commun.*, 4:1624–, 2013.

[222] Xuming Zou, Jingli Wang, Chung-Hua Chiu, Yun Wu, Xiangheng Xiao, Changzhong Jiang, Wen-Wei Wu, Liqiang Mai, Tangsheng Chen, Jinchai Li, Johnny C. Ho, and Lei Liao. Interface engineering for high-performance top-gated moS_2 field-effect transistors. *Adv. Mater.*, 26(36):6255–6261, 2014.

[223] Y. Q. Wu, P. D. Ye, M. A. Capano, Y. Xuan, Y. Sui, M. Qi, J. A. Cooper, T. Shen, D. Pandey, G. Prakash, and R. Reifenberger. Top-gated graphene field-effect-transistors formed by decomposition of sic. *Appl. Phys. Lett.*, 92(9):092102, 2008.

[224] Wei Liu, Deblina Sarkar, Jiahao Kang, Wei Cao, and Kaustav Banerjee. Impact of contact on the operation and performance of back-gated monolayer MoS_2 field-effect-transistors. *ACS Nano*, 9(8):7904–7912, 2015.

[225] G. Chen. *Nanoscale Energy Transport and Conversion*. Oxford, 1st edition, 2005.

[226] G. Gilat and L. J. Raubenheimer. Accurate numerical method for calculating frequency-distribution functions in solids. *Phys. Rev.*, 144:390–395, 1966.

[227] S. Datta. *Electronic Transport in Mesoscopic Systems*. Cambridge University Press, 1st edition, 1995.

[228] S. Datta. *Lessons from Nanoelectronics A New Perspective on Transport*, volume 1. World Scientific Publishing Co. Pte. Ltd., 2012.

[229] M. E. Eberhart and D. D. Vvedensky. Localized grain-boundary electronic states and intergranular fracture. *Phys. Rev. Lett.*, 58:61–64, 1987.

[230] Adina Luican-Mayer, Jose E Barrios-Vargas, Jesper Toft Falkenberg, Gabriel Auts, Aron W Cummings, David Soriano, Guohong Li, Mads Brandbyge, Oleg V Yazyev, Stephan Roche, and Eva Y Andrei. Localized electronic states at grain boundaries on the surface of graphene and graphite. *2D Mater.*, 3:031005, 2016.

[231] Sudipta Dutta and Katsunori Wakabayashi. Magnetization due to localized states on graphene grain boundary. *Sci. Rep.*, 5:11744–, 2015.

[232] Sanghamitra Debroy, Santhosh Sivasubramani, Gayatri Vaidya, Swati Ghosh Acharyya, and Amit Acharyya. Temperature and size effect on the electrical properties of monolayer graphene based interconnects for next generation mqca based nanoelectronics. *Sci. Rep.*, 10(1):6240, 2020.

[233] Stuart Thomas. Cmos-compatible graphene. *Nature Electronics*, 1(12):612–612, 2018.

[234] Junkai Jiang, Jiahao Kang, Wei Cao, Xuejun Xie, Haojun Zhang, Jae Hwan Chu, Wei Liu, and Kaustav Banerjee. Intercalation doped multilayer-graphene-nanoribbons for next-generation interconnects. *Nano Lett.*, 17(3):1482–1488, 2017.

[235] Xuesong Li, Weiwei Cai, Jinho An, Seyoung Kim, Junghyo Nah, Dongxing Yang, Richard Piner, Aruna Velamakanni, Inhwa Jung, Emanuel Tutuc, Sanjay K. Banerjee, Luigi Colombo, and Rodney S. Ruoff. Large-area synthesis of high-quality and uniform graphene films on copper foils. *Science*, 324(5932):1312–1314, 2009.

[236] Keun Soo Kim, Yue Zhao, Houk Jang, Sang Yoon Lee, Jong Min Kim, Kwang S. Kim, Jong-Hyun Ahn, Philip Kim, Jae-Young Choi, and Byung Hee Hong. Large-scale pattern growth of graphene films for stretchable transparent electrodes. *Nature*, 457:706–, 2009.

[237] Alfonso Reina, Xiaoting Jia, John Ho, Daniel Nezich, Hyungbin Son, Vladimir Bulovic, Mildred S. Dresselhaus, and Jing Kong. Large area, few-layer graphene films on arbitrary substrates by chemical vapor deposition. *Nano Lett.*, 9:30–35, 2009. PMID: 19046078.

[238] Xiao Chen, Pei Zhao, Rong Xiang, Sungjin Kim, JinHyeok Cha, Shohei Chiashi, and Shigeo Maruyama. Chemical vapor deposition growth of 5mm hexagonal single-crystal graphene from ethanol. *Carbon*, 94:810–815, 2015.

[239] Sukang Bae, Hyeongkeun Kim, Youngbin Lee, Xiangfan Xu, Jae-Sung Park, Yi Zheng, Jayakumar Balakrishnan, Tian Lei, Hye Ri Kim, Young Il Song, Young-Jin Kim, Kwang S. Kim, Barbaros Özyilmaz, Jong-Hyun Ahn, Byung Hee Hong, and Sumio Iijima. Roll-to-roll production of 30-inch graphene films for transparent electrodes. *Nat. Nanotechnol.*, 5:574–, 2010.

[240] Y.H. Zhang, B. Wang, H.R. Zhang, Z.Y. Chen, Y.Q. Zhang, B. Wang, Y.P. Sui, X.L. Li, X.M. Xie, G.H. Yu, Z. Jin, and X.Y. Liu. The distribution of wrinkles and their effects on the oxidation resistance of chemical vapor deposition graphene. *Carbon*, 70:81–86, 2014.

[241] H. F. Mataré. Transport processes at grain boundaries in polycrystalline material under optical illumination. *J. Appl. Phys.*, 54(11):6452–6458, 1983.

[242] Justin C. Koepke, Joshua D. Wood, David Estrada, Zhun-Yong Ong, Kevin T. He, Eric Pop, and Joseph W. Lyding. Atomic-scale evidence for potential barriers and strong carrier scattering at graphene grain boundaries: A scanning tunneling microscopy study. *ACS Nano*, 7:75–86, 2013.

[243] Xuge Fan, Stefan Wagner, Philip Schädlich, Florian Speck, Satender Kataria, Tommy Haraldsson, Thomas Seyller, Max C. Lemme, and Frank Niklaus. Direct observation of grain boundaries in graphene through vapor hydrofluoric acid (vhf) exposure. *Sci. Adv.*, 4(5), 2018.

[244] Jaewoon Kang, Chang-Ju Lee, Jaeeuk Kim, Honghwi Park, Changhee Lim, Junyeong Lee, Muhan Choi, and Hongsik Park. Effect of copper surface morphology on grain size uniformity of graphene grown by chemical vapor deposition. *Current Appl. Phys.*, 19(12):1414–1420, 2019.

[245] Kwanpyo Kim, Zonghoon Lee, William Regan, C. Kisielowski, M. F. Crommie, and A. Zettl. Grain boundary mapping in polycrystalline graphene. *ACS Nano*, 5(3):2142–2146, 2011.

[246] Gwan-Hyoung Lee, Ryan C. Cooper, Sung Joo An, Sunwoo Lee, Arend van der Zande, Nicholas Petrone, Alexandra G. Hammerberg, Changgu Lee, Bryan Crawford, Warren Oliver, Jeffrey W. Kysar, and James Hone. High-strength chemical-vapor–deposited graphene and grain boundaries. *Science*, 340(6136):1073–1076, 2013.

[247] Delwin Perera and Jochen Rohrer. Structure sensitivity of electronic transport across graphene grain boundaries. *Phys. Rev. B*, 98:155432, 2018.

[248] Samuel Dechamps, Viet-Hung Nguyen, and Jean-Christophe Charlier. Ab initio quantum transport in polycrystalline graphene. *Nanoscale*, 10(16):7759–7768, 2018.

[249] Arnab K. Majee, Cameron J. Foss, and Zlatan Aksamija. Impact of mismatch angle on electronic transport across grain boundaries and interfaces in 2d materials. *Sci.Rep.*, 7(1):16597–, 2017.

[250] S.M. Goodnick, D.K. Ferry, C.W. Wilmsen, Z. Liliental, D. Fathy, and O.L. Krivanek. Surface roughness at Si(100)-SiO_2 interface. *Phys. Rev. B*, 32:8171–8186, 1985.

[251] B. N. J. Persson. Theory of rubber friction and contact mechanics. *J. Chem. Phys.*, 115(8):3840–3861, 2001.

[252] J. Krim and G. Palasantzas. Experimental observations of self-affine scaling and kinetic roughening at sub-micron length scales. *Int. J. Mod. Phys. B*, 09(06):599–632, 1995.

[253] Matthew Pelliccione and Toh-Ming Lu. *Self-Affine Surfaces. In: Evolution of Thin Film Morphology. Materials Science*. Springer, New York, NY, 108 edition, 2008.

[254] B. N. J. Persson. On the fractal dimension of rough surfaces. *Tribol. Lett.*, 54(1):99–106, 2014.

[255] N. Nouri, V. Ziaei-Rad, and S. Ziaei-Rad. An approach for simulating microstructures of polycrystalline materials. *Comput. Mech.*, 52(1):181–192, 2013.

[256] F. M. Smits. Measurement of sheet resistivities with the four-point probe. *Bell System Technical Journal*, 37(3):711–718, 1958.

[257] R. Fletcher. A new approach to variable metric algorithms. *The Comput. Jour.*, 13:317–322, 1970.

[258] D. Goldfarb. A family of variable-metric methods derived by variational means. *Math. Comput.*, 24:23–26, 1970.

[259] John P. Perdew, Kieron Burke, and Matthias Ernzerhof. Generalized gradient approximation made simple. *Phys. Rev. Lett.*, 77:3865–3868, 1996.

[260] Stefano Baroni, Stefano de Gironcoli, Andrea Dal Corso, and Paolo Giannozzi. Phonons and related crystal properties from density-functional perturbation theory. *Rev. Mod. Phys.*, 73:515–562, 2001.

[261] Jae Hun Seol, Insun Jo, Arden L. Moore, Lucas Lindsay, Zachary H. Aitken, Michael T. Pettes, Xuesong Li, Zhen Yao, Rui Huang, David Broido, Natalio Mingo, Rodney S. Ruoff, and Li Shi. Two-dimensional phonon transport in supported graphene. *Science*, 328:213–216, 2010.

[262] Eilam Yalon, Ozgur Burak Aslan, Kirby K. H. Smithe, Connor J. McClellan, Saurabh V. Suryavanshi, Feng Xiong, Aditya Sood, Christopher M. Neumann, Xiaoqing Xu, Kenneth E. Goodson, Tony F. Heinz, and Eric Pop. Temperature-dependent thermal boundary conductance of monolayer MoS_2 by raman thermometry. *ACS Appl. Mater. Interfaces*, 9(49):43013–43020, 2017.

[263] Samy Merabia and Konstantinos Termentzidis. Thermal boundary conductance across rough interfaces probed by molecular dynamics. *Phys. Rev. B*, 89:054309, 2014.

[264] Poya Yasaei, Amirhossein Behranginia, Zahra Hemmat, Ahmed I El-Ghandour, Craig D Foster, and Amin Salehi-Khojin. Quantifying the limits of through-plane thermal dissipation in 2d-material-based systems. *2D Mater.*, 4(3):035027, 2017.

[265] D. Voß, P. Krüger, A. Mazur, and J. Pollmann. Atomic and electronic structure of WSe_2 from ab initio theory: Bulk crystal and thin film systems. *Phys. Rev. B*, 60:14311–14317, 1999.

[266] Zhun-Yong Ong. Thickness-dependent kapitza resistance in multilayered graphene and other two-dimensional crystals. *Phys. Rev. B*, 95:155309, 2017.

[267] Yanyuan Zhao, Xin Luo, Hai Li, Jun Zhang, Paulo T. Araujo, Chee Kwan Gan, Jumiati Wu, Hua Zhang, Su Ying Quek, Mildred S. Dresselhaus, and Qihua Xiong. Interlayer breathing and shear modes in few-trilayer MoS_2 and WSe_2. *Nano Lett.*, 13(3):1007–1015, 2013.

[268] Xiangfan Xu, Luiz F. C. Pereira, Yu Wang, Jing Wu, Kaiwen Zhang, Xiangming Zhao, Sukang Bae, Cong Tinh Bui, Rongguo Xie, John T. L. Thong, Byung Hee Hong, Kian Ping Loh, Davide Donadio, Baowen Li, and Barbaros Özyilmaz. Length-dependent thermal conductivity in suspended single-layer graphene. *Nat. Commun.*, 5:3689, 2014.

[269] Zhi Liang, Thomas E. Wilson, and Pawel Keblinski. Phonon interference in crystalline and amorphous confined nanoscopic films. *J. Appl. Phys.*, 121(7):075303, 2017.

[270] J. P. Perdew and Alex Zunger. Self-interaction correction to density-functional approximations for many-electron systems. *Phys. Rev. B*, 23:5048–5079, 1981.

[271] John P. Perdew and Yue Wang. Accurate and simple analytic representation of the electron-gas correlation energy. *Phys. Rev. B*, 45:13244–13249, 1992.

[272] B. J. van Wees, H. van Houten, C. W. J. Beenakker, J. G. Williamson, L. P. Kouwenhoven, D. van der Marel, and C. T. Foxon. Quantized conductance of point contacts in a two-dimensional electron gas. *Phys. Rev. Lett.*, 60:848–850, 1988.